

Computational and Mathematical Methods in Medicine

Image-Based Computational Cardiology: From Data to Understanding

Guest Editors: Linwei Wang, Vicky Y. Wang, and Heye Zhang

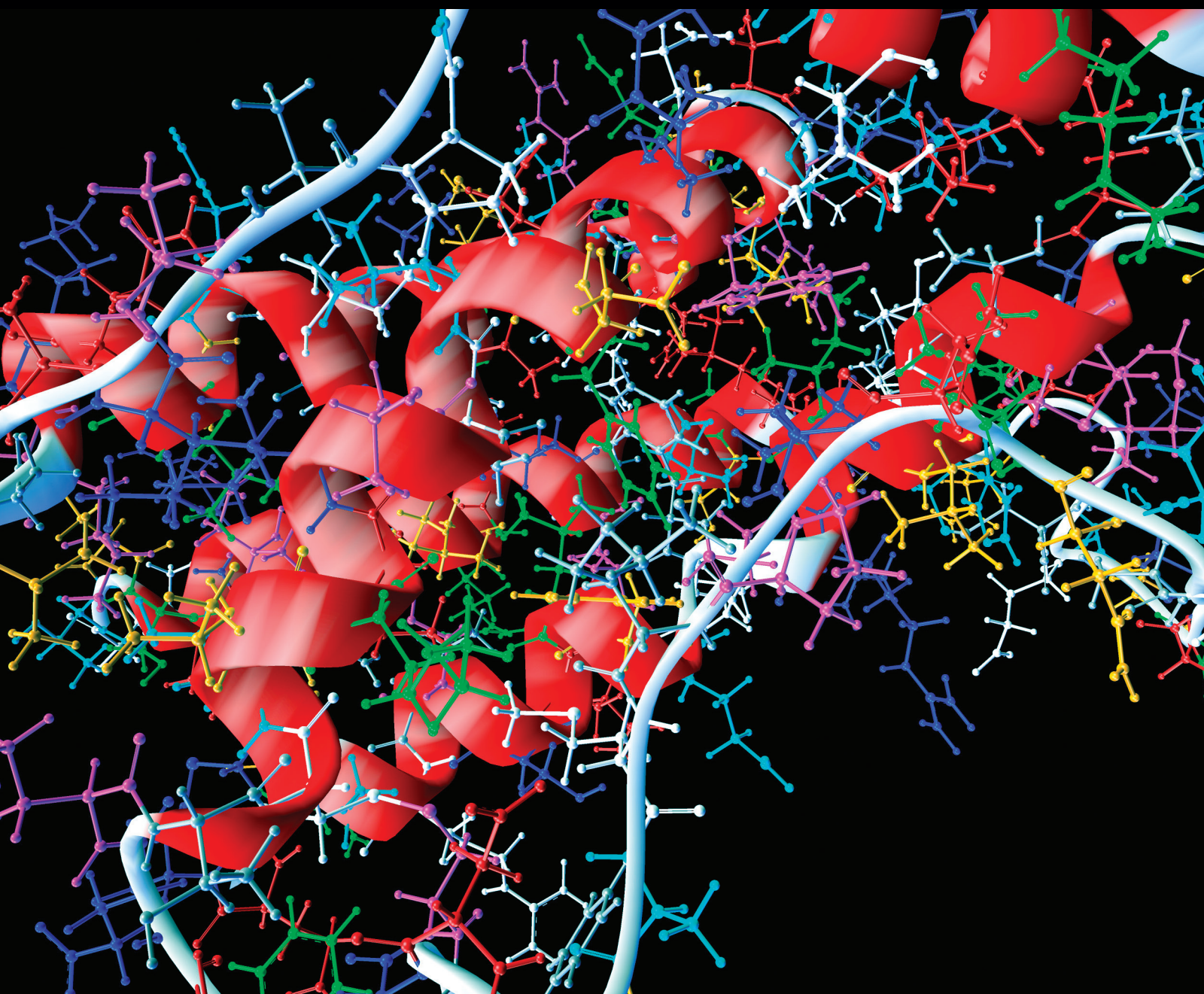




Image-Based Computational Cardiology: From Data to Understanding

Computational and Mathematical Methods in Medicine

**Image-Based Computational Cardiology:
From Data to Understanding**

Guest Editors: Linwei Wang, Vicky Y. Wang, and Heye Zhang



Copyright © 2014 Hindawi Publishing Corporation. All rights reserved.

This is a special issue published in “Computational and Mathematical Methods in Medicine.” All articles are open access articles distributed under the Creative Commons Attribution License, which permits unrestricted use, distribution, and reproduction in any medium, provided the original work is properly cited.

Editorial Board

- Emil Alexov, USA
Elena Amato, Italy
Konstantin G. Arbeev, USA
Georgios Archontis, Cyprus
Chris Bauch, Canada
Lynne Bilston, Australia
Konstantin B. Blyuss, UK
Thierry Busso, France
Xueyuan Cao, USA
Carlos Castillo-Chavez, USA
Carlo Cattani, Italy
Shengyong Chen, China
Phoebe Chen, Australia
Hsiu-Hsi Chen, Taiwan
Wai-Ki Ching, Hong Kong
Nadia A. Chuzhanova, UK
Maria N. D. S. Cordeiro, Portugal
Irena Cosic, Australia
Fabien Crauste, France
William Crum, UK
Getachew Dagne, USA
Qi Dai, China
Justin Dauwels, Singapore
Didier Delignières, France
Thomas Desaive, Belgium
Georges El Fakhri, USA
Issam El Naqa, USA
Ricardo Femat, Mexico
Marc T. Figge, Germany
Alfonso T. García-Sosa, Estonia
Amit Gefen, Israel
Humberto G.-Díaz, Spain
Igor I. Goryanin, Japan
Marko Gosak, Slovenia
- Dinesh Gupta, India
Damien Hall, Australia
Volkhard Helms, Germany
Akimasa Hirata, Japan
Roberto Hornero, Spain
Tingjun Hou, China
Seiya Imoto, Japan
Sebastien Incerti, France
Abdul Salam Jarrah, USA
Hsueh-Fen Juan, Taiwan
R. Karaman, Palestinian Authority
Lev Klebanov, Czech Republic
Andrzej Kloczkowski, USA
Xiang-Yin Kong, China
Xiangrong Kong, USA
Zuofeng Li, USA
Qizhai Li, China
Chung-Min Liao, Taiwan
Quan Long, UK
Reinoud Maex, France
Valeri Makarov, Spain
Kostas Marias, Greece
Richard J. Maude, Thailand
Panagiotis Mavroidis, USA
Georgia Melagraki, Greece
Michele Migliore, Italy
John Mitchell, UK
Arnold B. Mitnitski, Canada
Michele Nichelatti, Italy
Ernst Niebur, USA
Kazuhisa Nishizawa, Japan
Hugo Palmans, UK
Francesco Pappalardo, Italy
Matjaz Perc, Slovenia
- Jesús Picó, Spain
Giuseppe Pontrelli, Italy
Mohamad A. Pourhoseingholi, Iran
Christopher Pretty, New Zealand
Ravi Radhakrishnan, USA
John J. Rice, USA
Xu Shen, China
Simon A. Sherman, USA
E. Albert Siegbahn, Sweden
Sivabal Sivaloganathan, Canada
Dong Song, USA
Emiliano Spezi, UK
Tianhai Tian, Australia
Tianhai Tian, Australia
Jerzy Tiuryn, Poland
Nestor V. Torres, Spain
Nelson J. Trujillo-Barreto, Cuba
Po-Hsiang Tsui, Taiwan
Gabriel Turinici, France
Kutlu O. Ulgen, Turkey
Edelmira Valero, Spain
Liangjiang Wang, USA
Ruisheng Wang, USA
David A. Winkler, Australia
Guang Wu, China
Chen Yanover, Israel
Xiaojun Yao, China
Kaan Yetilmesoy, Turkey
Henggui Zhang, UK
Huaguang Zhang, China
Xiaoqi Zheng, China
Yunping Zhu, China

Contents

Image-Based Computational Cardiology: From Data to Understanding, Linwei Wang, Vicky Y. Wang, and Heye Zhang

Volume 2014, Article ID 120960, 2 pages

Fitting C^2 Continuous Parametric Surfaces to Frontiers Delimiting Physiologic Structures,

Jason D. Bayer, Matthew Epstein, and Jacques Beaumont

Volume 2014, Article ID 278479, 16 pages

The Relationship between the 24 h Blood Pressure Variability and Carotid Intima-Media Thickness: A Compared Study, Huahua Xiong, Dan Wu, Xiaohong Tian, Wan-Hua Lin, Chunyue Li, Heye Zhang, Yunpeng Cai, and Yuan-Ting Zhang

Volume 2014, Article ID 303159, 9 pages

Embryonic Heart Morphogenesis from Confocal Microscopy Imaging and Automatic Segmentation,

Hongda Mao, Megan Gribble, Arkady M. Pertsov, and Pengcheng Shi

Volume 2013, Article ID 293069, 7 pages

Accelerating Dynamic Cardiac MR Imaging Using Structured Sparse Representation, Nian Cai,

Shengru Wang, Shasha Zhu, and Dong Liang

Volume 2013, Article ID 160139, 8 pages

Three-Dimensional Reconstruction of Thoracic Structures: Based on Chinese Visible Human, Yi Wu,

Na Luo, Liwen Tan, Binji Fang, Ying Li, Bing Xie, Kaijun Liu, Chun Chu, Min Li, and Shaoxiang Zhang

Volume 2013, Article ID 795650, 7 pages

L_p -Norm Regularization in Volumetric Imaging of Cardiac Current Sources, Azar Rahimi, Jingjia Xu, and Linwei Wang

Volume 2013, Article ID 276478, 10 pages

Three-Dimensional Reconstruction of Coronary Arteries and Its Application in Localization of

Coronary Artery Segments Corresponding to Myocardial Segments Identified by Transthoracic

Echocardiography, Chunyan Zhong, Yanli Guo, Haiyun Huang, Liwen Tan, Yi Wu, and Wenting Wang

Volume 2013, Article ID 783939, 8 pages

A Voxel-Map Quantitative Analysis Approach for Atherosclerotic Noncalcified Plaques of the Coronary Artery Tree, Ying Li, Wei Chen, Kaijun Liu, Yi Wu, Yonglin Chen, Chun Chu, Binji Fang, Liwen Tan,

and Shaoxiang Zhang

Volume 2013, Article ID 957195, 9 pages

Editorial

Image-Based Computational Cardiology: From Data to Understanding

Linwei Wang,¹ Vicky Y. Wang,² and Heye Zhang³

¹ Rochester Institute of Technology, Rochester, NY 14634, USA

² Auckland Bioengineering Institute, The University of Auckland, Auckland 1010, New Zealand

³ Shenzhen Institutes of Advanced Technology, Shenzhen 518055, China

Correspondence should be addressed to Linwei Wang; linwei.wang@rit.edu

Received 29 April 2014; Accepted 29 April 2014; Published 1 June 2014

Copyright © 2014 Linwei Wang et al. This is an open access article distributed under the Creative Commons Attribution License, which permits unrestricted use, distribution, and reproduction in any medium, provided the original work is properly cited.

Over the past decade, rapid advances in imaging technologies have enabled state-of-the-art image-based analysis of cardiac function at a variety of scales and from multiple aspects, such as cardiac electrophysiology, cardiac biomechanics, and cardiovascular system. This special issue aims to showcase developments in cardiac image computing over the past five years, with a special emphasis given to novel computing techniques used to analyze cardiac anatomy and functions for better understanding of cardiac diseases. The final issue includes 8 high quality manuscripts that addressed some very interesting and timely research questions faced by researchers worldwide. The topics range from the improvement of real-time imaging acquisition, through the design of novel image analysis techniques and image-guided surgical planning tools, to cardiovascular risk assessment and detection.

Studying the evolution of heart formation has become an active research area [1]. Embryonic heart morphogenesis (EHM) is a complex and dynamic process where the heart transforms from a single tube into a four-chambered pump. Conventional imaging techniques fail to capture this process due to limited penetration depth. H. Mao et al. utilized confocal microscopy imaging with tissue optical immersion clearing technique to image the heart at different stages of development for an EHM study of quail. This area of study not only showed promising results in obtaining snapshots of hearts during growth, but also laid the foundation to investigate data-driven modeling of heart growth, which in turn could deepen our understanding of the cause, progression, treatment, and prevention of diseases related to cardiac growth.

Improving the speed of image reconstruction directly enhances the abundance of the data. In the work of N. Cai et al., a new method was developed to improve compressive sensing (CS) based reconstruction for dynamic cardiac MRI leveraging the theory of structured sparse representation. Their experimental results demonstrated that the proposed method improved the reconstruction quality of dynamic cardiac cine MRI over the state-of-the-art CS method [2].

Whilst numerous researches have been dedicated to imaging cardiac structure and mechanical function, non-invasive imaging of cardiac electrical activities remains to be a challenging task which entails the use of sophisticated mathematical models and optimization techniques [3, 4]. A. Rahimi et al. presented the superiority of an L_p-norm model over its L₁ and L₂ counterparts in imaging cardiac current sources with various spatial extents and distributions. Through computer-simulated and real-data experiments, they further demonstrated the feasibility of the proposed method in imaging the complex structure of excitation wavefront, as well as current sources distributed along the postinfarction scar border—the region that plays a critical role in the triggering and sustaining of lethal arrhythmias.

Extracting anatomical and physiological information of the heart from cardiac images requires robust yet simple segmentation techniques that suit different application purposes and different image qualities [5]. The work of J. Bayer et al. attempted to fit continuous parametric surfaces to scattered geometric data points forming frontiers delimiting physiologic structures in segmented images, and they successfully verified their methods by reconstructing

a geometric model of a mouse's ventricles from a CT scan. This type of segmentation technique provides useful means of visualizing anatomical structures from low-quality images. C. Zhong et al. also investigated model-based image segmentation technique to reconstruct coronary artery (CA) segments that correspond to myocardial segments typically shown in conventional echocardiographic sectional images. By incorporating the existing Chinese visible human (CVH) data and 5 sets of clinical CT data, they established 3D CA models and studied their application in localization of CA segments. The fully reconstructed 3D model allowed virtual dissection to simulate convectional sections of transthoracic echocardiography. A preliminary study involving 170 patients was also undertaken to assess their proposed technique.

With coronary artery disease (CAD) becoming one of the most frequent causes of heart failure, there continues to be an urgent need to design prompt and accurate clinical diagnosis for CAD [6]. For example, noncalcified plaques (NCPs) on coronary artery trees are associated with the presence of lipid-core plaques that are prone to rupture. Thus, it is important to detect and monitor the development of NCPs. Y. Li et al. proposed a mathematical morphological approach to quantitatively analyze the noncalcified plaques on a three-dimensional coronary artery wall model (3D-CAWM). This work combined Voxel-Map analysis techniques, plaque locating, and anatomical location related labeling, which was demonstrated to achieve more detailed and comprehensive coronary tree wall visualization.

Image-guided surgery has now become one of the most active research topics in cardiac imaging computing [7]. Y. Wu et al. reconstructed a three-dimensional digitized visible model of human thoracic structures to provide morphological data for imaging diagnosis and thoracic-cardiovascular surgery. This research provided an efficient learning platform for medical students or junior surgeons to better interpret human thoracic anatomy and practice virtual thoracic and cardiovascular surgery.

This special issue concludes with a clinical study that examined the relationship between blood pressure variation (BPV) and carotid intima-media thickness (IMT) for 60 subjects (aged between 33 and 79) in Shenzhen. H. Xiong et al. found that both the daytime systolic BPV and 24-hour systolic BPV evaluated by three indices are positively associated with IMT. They conclude that daytime systolic BPV is the best variable to represent the increasing of carotid IMT. In addition, after adjusting by age, sex, smoking, hypertension, and mean blood pressure (BP) and peak-to-peak values, 24 h diastolic BPV evaluated with standard deviation also presents the favorable performance.

Overall, the 8 manuscripts included in this special issue provide a sample of the current state in image-based computational cardiology, including the classic topics such as image segmentation and image reconstruction, the relatively young areas such as growth modeling and electrophysiological imaging, and the use of computational techniques in image-based understanding, diagnosis, and surgery planning of cardiac diseases. The continuing effort in all these expanding and interconnected areas will likely improve our understanding

of the mechanism, treatment, and prevention of cardiac diseases.

Acknowledgments

We would like to express our deep appreciation to all reviewers who devoted their time and efforts to assisting us with selecting high quality original research to be presented in this special issue. We are grateful for all researchers in the field of cardiac imaging and computing who supported the development of the special issue.

Linwei Wang
Vicky Y. Wang
Heye Zhang

References

- [1] M. K. Rausch, A. Dam, S. Göktepe, O. J. Abilez, and E. Kuhl, "Computational modeling of growth: systemic and pulmonary hypertension in the heart," *Biomechanics and Modeling in Mechanobiology*, vol. 10, no. 6, pp. 799–811, 2011.
- [2] M. Lustig, D. Donoho, and J. M. Pauly, "Sparse MRI: the application of compressed sensing for rapid MR imaging," *Magnetic Resonance in Medicine*, vol. 58, no. 6, pp. 1182–1195, 2007.
- [3] Y. Rudy, "Noninvasive electrocardiographic imaging of arrhythmogenic substrates in humans," *Circulation Research*, vol. 112, pp. 863–874, 2013.
- [4] L. Wang, H. Zhang, K. C. L. Wong, H. Liu, and P. Shi, "Physiological-model-constrained noninvasive reconstruction of volumetric myocardial transmembrane potentials," *IEEE Transactions on Bio-Medical Engineering*, vol. 57, no. 2, pp. 296–315, 2010.
- [5] C. Petitjean and J. Dacher, "A review of segmentation methods in short axis cardiac MR images," *Medical Image Analysis*, vol. 15, no. 2, pp. 169–184, 2011.
- [6] R. J. Chilton, "Pathophysiology of coronary heart disease: a brief review," *The Journal of the American Osteopathic Association*, vol. 104, no. 9, supplement 7, pp. S5–S8, 2004.
- [7] K. Cleary and T. M. Peters, "Image-guided interventions: technology review and clinical applications," *Annual Review of Biomedical Engineering*, vol. 12, pp. 119–142, 2010.

Research Article

Fitting C^2 Continuous Parametric Surfaces to Frontiers Delimiting Physiologic Structures

Jason D. Bayer,¹ Matthew Epstein,² and Jacques Beaumont³

¹ *L'Institut de Rythmologie et Modélisation Cardiaque, Université de Bordeaux, 166 Cours de l'Argonne, 33000 Bordeaux, France*

² *Department of Bioengineering, Binghamton University, P.O. Box 6000, Binghamton, NY 13902, USA*

³ *Department of Pharmacology, SUNY Upstate Medical University, 3135 Weiskotten Hall, 750 East Adams Street, Syracuse, NY 13210, USA*

Correspondence should be addressed to Jacques Beaumont; beaumontj@upstate.edu

Received 7 October 2013; Revised 16 January 2014; Accepted 23 January 2014; Published 24 March 2014

Academic Editor: Linwei Wang

Copyright © 2014 Jason D. Bayer et al. This is an open access article distributed under the Creative Commons Attribution License, which permits unrestricted use, distribution, and reproduction in any medium, provided the original work is properly cited.

We present a technique to fit C^2 continuous parametric surfaces to scattered geometric data points forming frontiers delimiting physiologic structures in segmented images. Such mathematical representation is interesting because it facilitates a large number of operations in modeling. While the fitting of C^2 continuous parametric curves to scattered geometric data points is quite trivial, the fitting of C^2 continuous parametric surfaces is not. The difficulty comes from the fact that each scattered data point should be assigned a unique parametric coordinate, and the fit is quite sensitive to their distribution on the parametric plane. We present a new approach where a polygonal (quadrilateral or triangular) surface is extracted from the segmented image. This surface is subsequently projected onto a parametric plane in a manner to ensure a one-to-one mapping. The resulting polygonal mesh is then regularized for area and edge length. Finally, from this point, surface fitting is relatively trivial. The novelty of our approach lies in the regularization of the polygonal mesh. Process performance is assessed with the reconstruction of a geometric model of mouse heart ventricles from a computerized tomography scan. Our results show an excellent reproduction of the geometric data with surfaces that are C^2 continuous.

1. Introduction

High-resolution *in vivo* imaging has become an essential tool for the practice of modern day medicine. As a matter of fact, hospitals have upgraded their infrastructure to acquire and visualize terabytes of digital medical data and to make these data readily available to the clinician. Prompted by this success, more and more clinicians introduce cutting edge technology in diagnosis. We can say we witnessed the rise of what we have come to term computational medicine.

In this trend, among various options to capitalize on the wealth of medical data is the simulation of biophysical processes. This option is particularly appealing as it equips the clinician with advanced means to make elaborate interpretations from data collected non- or semi-invasively, which can potentially lead to a better understanding of the molecular mechanisms of diseases, detection of trends in a population, and risk/benefit analysis of various therapeutic options.

A major facet of computational medicine is the reconstruction of image-based computer models of physiologic structures, for example, tissue, organs, and limbs, in order to effectively interface with the clinician. In cardiology, we count a number of contributions in heart model reconstruction [1–5] that enable us to be optimistic in terms of practical clinical applications in the near future. Clearly, the same applies to neuroscience [6–8].

A very important step in the reconstruction of image-based models is the mathematical description of surfaces bounding the physiologic structure of interest. Here our goal is to generate a compact C^2 continuous representation of surfaces. We elect to use dimension 3 (3 physical coordinates) and codimension 2 (2 parametric coordinates) parametric B-splines. Such surfaces have a number of advantages for modeling; that is, they are compact and facilitate the calculation of areas, volumes, curvatures, crests, tangent planes, and many other operations which are useful by themselves and essential

in several modeling phases, like mesh generation, application of boundary conditions, and coupling with several field equations.

While the fitting of curves to scattered geometric data points is quite trivial, the fitting of surfaces to scattered geometric data points is not. Surface fitting is problematic because a unique parametric coordinate should be assigned to each geometric data point, and the precision of the fit is quite sensitive to the distribution of these parametric coordinates. To our knowledge, there are no documented techniques to assign unique parametric coordinates and to distribute them in a manner that guarantees a precise fit.

There has been significant work on this question. So far two different approaches have been proposed. In the first approach, the surface in question is the zero level set of a three-dimensional function that is fitted to the data. This avoids the mapping of the geometric data onto a parametric plane since the function in question is defined in the same space as the original image. Most algorithms have been implemented with polygonal surfaces, but could also be implemented with B-splines [9].

The second approach, deformable models, deforms an initial template model until it matches the target geometric data points. The technique initially introduced by Kass et al. [10] has been given considerable attention. The contributions of McNerney and Trezopoulos [11, 12] and Yoo [13] are particularly remarkable to the subject. The template model can be defined with a polygonal or parametric B-Spline surface, and various rules can be used to guide the deformations, for example, intensity gradient, point-to-surface signed distance, mechanical properties of the surface, inertia in displacement, and others like energy, which depends on the physics of the problem. In a version of this approach, the conventional rules to guide deformation (e.g., intensity gradient) are replaced by a function based on the comparison of pixel intensity with the average intensity of pixels inside and outside regions delimited by the displaced boundary [14]. This version is particularly robust (no manual assistance required) in the presence of noise and low contrast. Although this advantage comes at the expense of an additional computational load due operations performed on all image pixels at each iteration, which may be acceptable in a number of cases. Finally, see Park et al. [15] for a recent extensive application, and the review of image segmentation by Ma et al. [16] for a summary of applications.

Here we propose a different approach, that is, a direct fit of codimension 2 parametric B-splines to a polygonal surface extracted from a segmented image. After its extraction, the polygonal surface is projected onto a parametric plane. The projection preserves vertex connectivity and ensures a one-to-one mapping between the physical and parametric spaces. Afterward, the projected polygonal surface is regularized for polygonal area and edge length. The spatial variation in polygonal area and edge length is quantified by a function, the minimization of which governs the regularization. Finally, from this point parametric surface fitting, constrained or not, is quite trivial. The main advantages of our technique are its accuracy and computational simplicity.

The method is applied to an X-ray computerized tomography scan of a mouse heart. The results show that C^2 continuous parametric surfaces with only 9×9 degrees of freedom can accurately fit convoluted geometries like the endocardial surface of the heart.

2. Methods

2.1. Acquisition of Test Medical Imaging Data. An adult mouse heart is excised, Langendorff perfused, fixed in diastole, and then embedded in vegetal grease. It is subsequently imaged with an X-ray laboratory scanner (SkyScan) at $7.5 \mu\text{m}$ resolution. A computerized tomography (CT) scan is generated with 720 projections. Each projection is integrated over 1.8 s. The background is subtracted; the signal is compensated for fluctuations and converted on a logarithmic scale. The signal is finally postprocessed with a modified Feldkamp tomographic reconstruction algorithm [17]. See Methods in Bayer et al. [18] for more details on the specimen preparation and CT imaging.

The same heart is also imaged for tissue microstructure with a laser scanning confocal microscope. To this end, the heart is sliced every $20 \mu\text{m}$ along its short axis with a vibrotome. Each slice is stained for myofibrils with rhodamine phalloidin. They are subsequently imaged with a Zeiss 510 META confocal microscope. The images are acquired on optical planes separated by $5 \mu\text{m}$. Further details on staining and imaging are given in Slamani et al. [19]. Acquisition at this high resolution requires assembling the images in order to appropriately visualize the physiologic structure, which we perform with a Fourier transform [19, 20].

2.2. Polygonal Surfaces Extraction. The CT data is composed of gray scale images (pixel intensities 0–255) stacked along the long axis of the heart. They comprise a total of 860 planes. The contrast is excellent, and the edges of the heart cavities, as well as the epicardium, are simply delineated with thresholding. Specifically, all voxels crossing a threshold intensity of 100 are labeled as edge voxels. The external faces of these voxels (quads) constitute the polygonal surface we project onto the parametric plane.

When we need to extract a triangulated surface for visualization purposes, or because a very high precision is required, we extract it from the boundary voxels with the marching cube algorithm of Lorensen and Cline [21], along with modifications introduced by Lewiner et al. [22].

We denote the set of vertices and triangles or quadrilaterals generated from the surface extraction by $V(x, y, z)$ and $T(V)$ or $Q(V)$, respectively. Then the inverse connectivity vertices-triangles $V(T)$ or vertices-quads $V(Q)$ is generated. Finally, a graph of the nodes $C(V)$ (table of vertices adjacent to a vertex) is readily generated from the connectivity table $T(V)$ or $Q(V)$.

2.3. Polygonal Surface Projection onto a Parametric Plane. Direct parametric surface fitting requires that we first assign a unique parametric coordinate to each of the N vertices of $V(x, y, z)$. We achieve this by projecting the polygonal

surface onto a $u - v$ parametric plane; $u \in [u_{\min}, u_{\max}]$, $v \in [v_{\min}, v_{\max}]$. The projection assigns parametric coordinates $\mathcal{Z}(u, v)$ to each vertex in $V(x, y, z)$. We then refer to the projected surface by $T(\mathcal{Z})$ or $Q(\mathcal{Z})$. To project the polygonal surfaces, the user selects a region to map onto the polygonal surface, which is delimited by 4 anchor points joined by 4 segments. Each of the 4 anchor points are mapped to one corner of the parametric plane, and the vertices on the segments joining them are equidistributed along the edges $\Gamma \in [\Gamma_a, \Gamma_b, \Gamma_c, \Gamma_d]$, that we label $a-d$ while following a boolean order, that is, $u_{\min}, u_{\max}, v_{\min}, v_{\max}$. We denote the set of indices of the vertices mapped to the edges of the parametric plane by g . The region inside the 4 segments is mapped onto the parametric plane. The rule employed to perform a one-to-one mapping is deduced from the function

$$\vartheta(\mathbf{u}, \mathbf{v}) = \sum_{n=0}^{N-1} \sum_{m=0}^{M_n-1} (u_n - u_m^{(n)})^2 + (v_n - v_m^{(n)})^2, \quad (1)$$

where (\mathbf{u}, \mathbf{v}) denote the u and v parametric coordinates of the vertices of $V(x, y, z)$. Throughout this paper we denote vectors and matrices by lower- and uppercase bold letters, respectively. Therefore, the parameter M_n is the number of adjacent vertices to vertex n with coordinates (u_n, v_n) . The M_n adjacent vertices to u_n, v_n are denoted by $u_m^{(n)}, v_m^{(n)}$. These indices correspond to line n in the graph $C(V)$.

The function $\vartheta(\mathbf{u}, \mathbf{v})$ expresses for each vertex of $V(x, y, z)$ the sum of squared distance to its neighbors. The $\text{Min}\{\vartheta(\mathbf{u}, \mathbf{v})\}$ with respect to (\mathbf{u}, \mathbf{v}) ,

$$\begin{aligned} \frac{\partial \vartheta(\mathbf{u}, \mathbf{v})}{\partial u_\alpha} &= M_\alpha u_\alpha - \sum_{m=0}^{M_\alpha-1} u_m^\alpha = 0, \\ \frac{\partial \vartheta(\mathbf{u}, \mathbf{v})}{\partial v_\alpha} &= M_\alpha v_\alpha - \sum_{m=0}^{M_\alpha-1} v_m^\alpha = 0 \end{aligned} \quad (2)$$

$\forall \alpha \in [0, N-1],$

leads to the matrix systems

$$\mathbf{A}^u \mathbf{u} = \mathbf{c}^{(u)} \quad \mathbf{A}^v \mathbf{v} = \mathbf{c}^{(v)}. \quad (3)$$

Since we fix the coordinates of the vertices along the edges of the parametric plane, the lines and columns of (3) corresponding to indices g are moved to the right hand side, which lead to the reduced matrix systems

$$\widehat{\mathbf{A}}^u \widehat{\mathbf{u}} = \widehat{\mathbf{c}}^{(u)} \quad \widehat{\mathbf{A}}^v \widehat{\mathbf{v}} = \widehat{\mathbf{c}}^{(v)}. \quad (4)$$

Since $\widehat{\mathbf{A}}^u, \widehat{\mathbf{A}}^v$ are nonsingular, this matrix system generates a one-to-one mapping. The coordinates obtained in this manner correspond to a distribution where each vertex tends to be at an equal distance from all its immediate neighbors. This confers interesting properties to the map, but does not mean all points are equidistant from one another. This property is desirable at the expense of additional processing.

Note the particular structure of the matrices $\widehat{\mathbf{A}}^u, \widehat{\mathbf{A}}^v$. First, they are sparse and the number of nonzero coefficients

in each line is given by the number of neighbors in the parametric plane. The diagonal is $M_n, n \in [0, N-1], n \ni g$ and the off diagonal elements are -1 . The matrices are diagonally dominant, and thus positive definite. Furthermore, since the coefficients are constant we need only to store in memory their diagonal. Such matrices have a small condition number and can be readily solved with a conjugate gradient method.

When the point cloud is really dense, we may sometimes need to postprocess the map to avoid a collision between vertices. If the bounding box of two segments intersects in the parametric plane, we replace the endpoint on each segment closest to the intersection by their intersection. Finally, when segments sharing one vertex are nearly parallel, we fuse them. Note that such postprocessing is necessary only when the point cloud is really dense. In most applications this can be avoided by decomposing the reconstruction.

2.4. Regularization of a Polygonal Mesh. While the mapping of the polygonal surface to the parametric plane is a one-to-one mapping, this does not guarantee the size of the polygons (triangles or quadrilaterals) to be regular. Irregularity in size dramatically affects the quality of the final parametric surface fit because areas that are extensively compressed in the parametric plane are given less weight, if not totally ignored, in the fit. This may be alleviated by increasing the number of elements of the final parametric surface, but this does not solve the problem.

We address this problem by regularizing the polygons of the mesh for area and edge length. To do so, we borrow a mesh regularization concept introduced by Jacquotte in [23]. The concept consists of adjusting the grid-point coordinates in a manner that minimizes polygonal element deformations with respect to a reference element.

First, we define a transformation or a mapping from the space $\xi - \eta$ to the parametric space $u - v$,

$$\mathcal{T}(\xi, \eta) = [U(\xi, \eta), V(\xi, \eta)], \quad (5)$$

where $U(\xi, \eta), V(\xi, \eta)$ are two functions mapping the ξ, η coordinates of a reference element defined on $\xi, \eta \in [-1, 1]$ to the (u, v) coordinates of the parametric plane, respectively. The reader is referred to Appendix A for details regarding the construction of mapping functions for both quadrilateral and triangular meshes. The transformation $\mathcal{T}(\xi, \eta)$ maps a reference quadrilateral to a mesh element according to solid mechanics, where the element deformation gradient is given by

$$\overline{\mathcal{V}} \mathcal{T}(\xi, \eta) = \begin{bmatrix} U_\xi & U_\eta \\ V_\xi & V_\eta \end{bmatrix}, \quad \overline{\mathcal{V}} = \begin{bmatrix} \frac{\partial}{\partial \xi} & \frac{\partial}{\partial \eta} \end{bmatrix}, \quad (6)$$

and the subscripts indicate derivative with respect to this variable. Note from (6), the deformation gradient is also the Jacobian matrix \mathcal{J} of the mapping between the $\xi - \eta$ and $u - v$ spaces. This quantity is precisely what we wish to minimize; that is, a regularization is nothing else than a minimization of the variation in element deformation. However, performing this minimization over the $u - v$ parametric domain is not trivial. For the function to reach the condition we are looking

for, that is, $\mathcal{V}(u, v)$ having polygons with quasi-equal areas and edges length in the parametric plane, the function should be convex with one minimum reflecting that condition. This implies our measure of deformation to be invariant of rotation, since rotation does not change area and edge length.

Jacquotte in [23] addressed this problem by minimizing the Matrix $\mathbf{H} = \mathcal{F}^T \mathcal{F}$ with respect to three invariants. From this point, our approach differs from Jacquotte's approach since we find new parametric grid coordinates $(\mathbf{u}', \mathbf{v}')$ satisfying,

$$(\mathbf{u}', \mathbf{v}') : \text{Min} \left\{ \sum_{e=0}^{N_e-1} \left\| \mathcal{F}^e - \frac{\text{Adj}(\mathcal{F}^e)}{|\mathcal{F}^e|} \right\|_{F, \Omega_e} \right\}, \quad (7)$$

where N_e is the number of elements in the polygonal surface, \mathcal{F}^e is the Jacobian of element e , $\text{Adj}\{\cdot\}$ is the adjugate, $|\cdot|$ is the determinant, Ω_e is the domain of an element in the $\xi - \eta$ plane, and $\|\cdot\|_{F, \Omega}$ is a modified Frobenius norm

$$\|(\cdot)\|_{F, \Omega} = \sum_i \sum_j \int_{\Omega} [(\cdot)_{i,j}(\Omega)]^2 d\Omega, \quad (8)$$

which needs to be introduced because the matrix coefficients are a function of (ξ, η) . Recall, the rightmost term is nothing else than \mathcal{F}^{-1} . The motivation for this condition is that when the reference element is subjected only to a translation, $\mathcal{F} = I$. In this case $\mathcal{F} = \mathcal{F}^{-1}$, and condition (7) is strictly met. The modified Frobenius norm of $\mathcal{F} - \mathcal{F}^{-1}$ increases with scaling, and changes slightly with rotation. Thus, the minimization of (7) tends to keep all elements shapes closed to the reference one.

2.5. Constrained Parametric Surface Fitting. The final surface is represented with a codimension 2, dimension 3 parametric B-Spline. The parametric plane is subdivided into $N_{bx} \times N_{by}$ elements of equal size. This subdivision defines $(N_{bx} + 1) \times (N_{by} + 1)$ junction points that we term the control points. Functions $X(u, v)$, $Y(u, v)$, $Z(u, v)$ mapping the $u - v$ space to the $x - y - z$ space, one for each of the (x, y, z) coordinates, respectively, are defined with an expansion of codimension 2 B-Splines, one B-spline $B_s(u, v)$ for each control point, "s" indexing them. To the control points defined in the parametric plane, we add a row and a column at each end so the elements bordering the parametric plane have the same degree of freedom as the elements inside the plane. Thus, the total number of control points is $(N_{bx} + 3) \times (N_{by} + 3)$. Parametric surface fitting consists in finding the coefficients $\zeta^{(x)}, \zeta^{(y)}, \zeta^{(z)}$ of the expansion

$$\begin{aligned} X(u, v) &= \sum_{s=0}^{\bar{s}} \zeta_s^{(x)} B_s(u, v), \\ Y(u, v) &= \sum_{s=0}^{\bar{s}} \zeta_s^{(y)} B_s(u, v), \\ Z(u, v) &= \sum_{s=0}^{\bar{s}} \zeta_s^{(z)} B_s(u, v), \end{aligned} \quad (9)$$

$\bar{s} = (N_{bx} + 2) \times (N_{by} + 2)$ such that the distance between the geometric data points and points on the surface with the same parametric coordinate is minimized.

The $B_s(u, v)$ are indexed according to a boolean order, u -coordinate first then the v -coordinate. They are built with a tensor product of elementary 1-D B-Splines,

$$B(u, v) = \mathbf{b}(u) \otimes \mathbf{b}(v). \quad (10)$$

At control point "n" of a one-dimensional axis, we define the elementary B-spline by

$$b(u)^3 = \begin{cases} b_0(u) = \frac{(1 - 3\bar{u} + 3\bar{u}^3 - \bar{u}^3)}{48}, \\ \bar{u} = 2u - \frac{(u_{n+2} + u_{n+1})}{(u_{n+2} - u_{n+1})}, \\ \text{for } u_{n+1} < u < u_{n+2}, \\ b_1(u) = \frac{(23 - 15\bar{u} - 3\bar{u}^2 + 3\bar{u}^3)}{48}, \\ \bar{u} = 2u - \frac{(u_{n+1} + u_n)}{(u_{n+1} - u_n)}, \\ \text{for } u_n < u < u_{n+1}, \\ b_2(u) = \frac{(23 + 15\bar{u} - 3\bar{u}^2 - 3\bar{u}^3)}{48}, \\ \bar{u} = 2u - \frac{(u_n + u_{n-1})}{(u_n - u_{n-1})}, \\ \text{for } u_{n-1} < u < u_n, \\ b_3(u) = \frac{(1 + 3\bar{u} + 3\bar{u}^2 + 3\bar{u}^3)}{48}, \\ \bar{u} = 2u - \frac{(u_{n-1} + u_{n-2})}{(u_{n-1} - u_{n-2})}, \\ \text{for } u_{n-2} < u < u_{n-1}, \end{cases} \quad (11)$$

where it should be clear that the support (range where the function is nonnull) of an elementary 1D B-spline extends over 4 segments, and the support of a 2-D B-spline over 4×4 elements. The B-Spline (1-D or 2-D) and its first 2 derivatives vanish at the border of the support. This way any linear combination remains C^2 continuous. More information on B-splines can be found in Bartels et al. [24].

Least square fitting for this case is quite trivial. It consists to find $\zeta^{(x)}, \zeta^{(y)}, \zeta^{(z)}$ that minimizes

$$\begin{aligned} \|\mathbf{x} - X(\mathbf{u}, \mathbf{v})\|_2, \quad \|\mathbf{y} - Y(\mathbf{u}, \mathbf{v})\|_2, \\ \|\mathbf{z} - Z(\mathbf{u}, \mathbf{v})\|_2, \end{aligned} \quad (12)$$

with $\mathbf{x}, \mathbf{y}, \mathbf{z}$ being the vectors of x, y, z coordinates of the geometric data points. This leads to solving 3 matrix systems, each of small dimension. Excellent results were obtained with 9×9 elements. In addition, the matrices are sparse with nonnull coefficients in each row and are well conditioned as a result of the regularization. Thus, they can be

readily solved with an iterative method like the Generalized Minimal Residual (GMRES) [25, Chapter 6].

For practical reasons the fit is constrained in two ways. First, we impose a degree of stiffness to the surface. Second, we sometimes require the parametric surface to exactly match a predefined contour. After visual inspection a user may wish to limit the excursion of a surface in zones not having enough geometric data points. This can be done by imposing the surface to be more stiff. The second constraint allows to decompose of the reconstruction of a complex physiological structure. This version of our reconstruction technique does not allow imposing C^1 continuity at the junction between parametric surfaces, but this could be added by extending the treatment presented in Appendix B.

Stiffness is added by constraining the fit with curvature and twist. In this case the objective function to optimize the x -component becomes

$$\begin{aligned} \Theta_x &= (1 - \lambda) \|\mathbf{x} - X(\mathbf{u}, \mathbf{v})\|_2 \\ &+ \lambda \int_{\Omega_p} (X_{uu}^2 + 2X_{uv}^2 + X_{vv}^2) d\Omega_p, \quad (13) \\ \lambda &\in [0, 1], \end{aligned}$$

Ω_p : parametric plane, and similarly for the (y, z) components.

To clamp the parametric surface along any of its edges, we fit the contour with a codimension 1 B-spline. The codimension 1 B-spline should have exactly the same number of control points as the codimension 2 B-spline along the axis of the clamp. Also, the parametric segments should be exactly the same length as the sides of the quads of the codimension 2 B-splines along the axis of the clamp. To guarantee an exact clamp, we remove some coefficients from the expansion of the codimension 2 B-spline and fix them with algebraic relations that guarantee the parametric surface to match the codimension 1 B-spline along the clamped edge. Details of this calculation are given in Appendix B.

2.6. Distance Metrics. We assessed the performance of our fitting algorithm by measuring the distance between the target geometric data points and the model surface. For a data point “ n ” in $V(x, y, z)$, the distance between this point and the model $D_n(u, v)$ is the closest distance from this point to the model surface. Determination of minimal distance by sweeping points on the parametric surface can be time consuming and even inaccurate since the surface can undergo significant excursion between the sampled data points. On the other hand, bicubic B-Splines are too complex for analytical determination of minimal distance.

Here we explore the flexibility of the parametric surface representation to tackle this problem. First, we seek the minimal distance along $u = \text{constant}$ and $v = \text{constant}$ coordinate lines, 4 in each direction on any element. The derivatives

$$\frac{\partial D_n^2(u, v)}{\partial u}, \quad \frac{\partial D_n^2(u, v)}{\partial v}, \quad (14)$$

along a v or u coordinate line is a 5th degree polynomial. We find its zeros with an eigenvalue method [26]; that is, we write a companion matrix, the eigenvalues of which are the polynomial zeros. The eigenvalues in question are found with the method outlined in LAPACK [27, Section 2.4.5]. The companion matrix is transformed into an upper Hessenberg form, which is subsequently reduced to a tridiagonal form, the diagonal of which contains the eigenvalues. Our implementation exploits the sparsity pattern of the companion matrix which makes the root finding fast, but still accurate. $D_n(u, v)$ is evaluated on all roots of the 8 coordinate lines if the corresponding u, v coordinate is in the B-spline element. It is also evaluated on the 4-element vertices.

The search is further refined with a fixed point method, starting from the closest of the above distances u_c, v_c . The surface $D_n(u, v)$ is approximated ($\widehat{D}_n(u, v)$) at u_c, v_c , with

$$\begin{aligned} \widehat{D}_n(u, v) &= [(u - u_c), (v - v_c)] \mathbf{H} \begin{bmatrix} (u - u_c) \\ (v - v_c) \end{bmatrix} \\ &+ \mathbf{g} \begin{bmatrix} (u - u_c) \\ (v - v_c) \end{bmatrix} + D_n(u_c, v_c), \end{aligned} \quad (15)$$

where \mathbf{H} and \mathbf{g} are the Hessian and gradient of $D_n(u, v)$ at u_c, v_c . The minimum of (15) is found by solving the 2×2 matrix system expressing the minimum condition, $(u, v) \rightarrow (u_c, v_c)$, whose operation is repeated until $|\mathbf{g}| < \epsilon$, a predetermined threshold, or when the line segment joining the current minimum to the new one crosses an element edge. The final minimal distance is the minimum of the minimal distance over all elements.

3. Results

3.1. The Cardiac Imaging Data. The test data set (Figure 1) is an X-ray computerized tomography scan of an excised mouse heart fixed in diastole. The data were collected on a laboratory microscanner (CT) at $7.5 \mu\text{m}$ resolution. See the Methods for specimen preparation and data acquisition. Figure 1 shows three sections across this data set: one longitudinal section perpendicular to the septum and two cross sections along the short axis of the heart. The right and left ventricles are labeled RV and LV, respectively. The blue and green lines indicate the height of the section. The longitudinal section is 1.125 mm from the epicardial surface, and the two cross sections are 2.475 mm (blue) and 2.775 mm (green) from the atrial apex, respectively. The distance from the base to the ventricular apex is 7.050 mm, and the diameter at the base is 1.880 mm.

The longitudinal view exposes a papillary muscle (red rectangle) extending from the left endocardial surface to the aortic valve. The cross section at 2.775 mm shows the root of the papillary muscle. The other section at 2.475 mm clearly delineates a cross section of the papillary muscle which is detached from the endocardial surface. We believe papillary muscles play an important role in the initiation of abnormal beats since cardiac fiber changes rapidly in such region. Therefore, accurate modeling of these structures is a main motivation for the geometric modeling technique developed here.

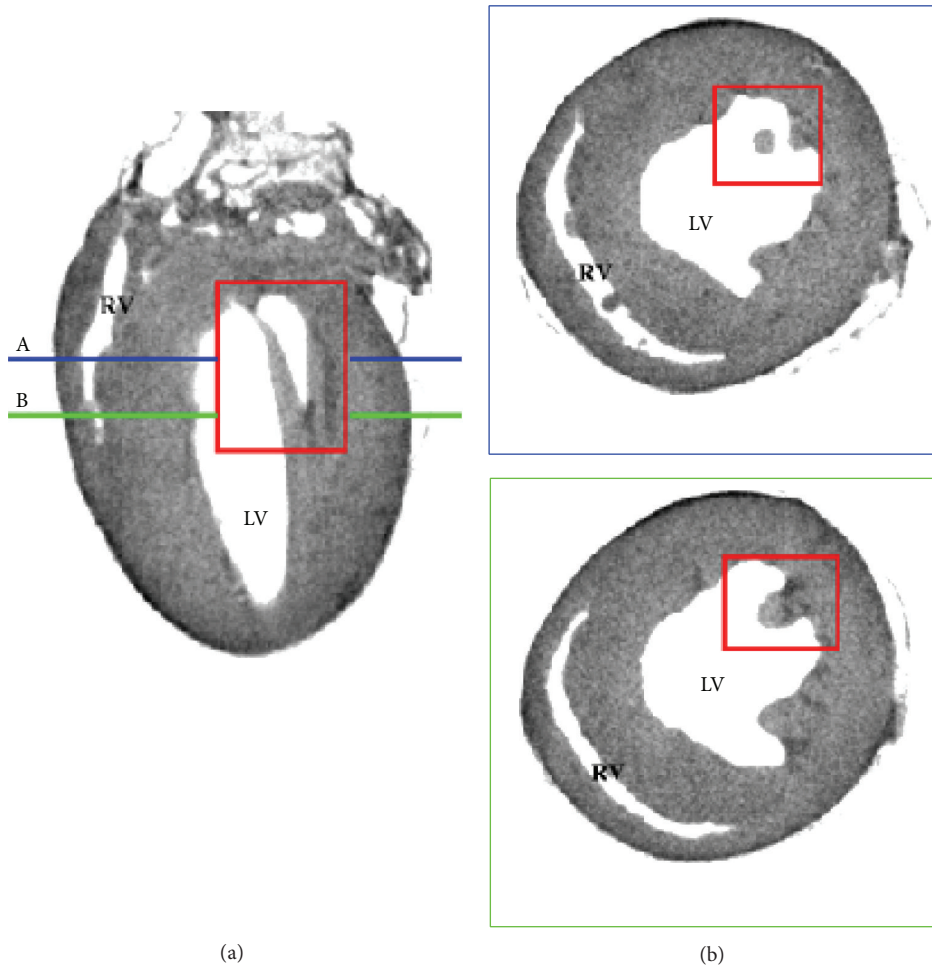


FIGURE 1: Computerized tomography scan of a mouse heart fixed in diastole. (a) Longitudinal section of the heart perpendicular to the septum. (b) Two sections along the short axis of the heart.

Two other masses are visible in the cross section at 2.475 mm of the right ventricle. These are probably papillary muscles torn during the heart preparation. The injection of grease, although done at relatively low pressure, may have damaged the fragile papillary muscles.

Finally, from this image the reader can appreciate the fact that contrast is excellent. No additional processing was performed after the tomographic reconstruction; still the edges of the cavity and epicardium are clearly visible.

3.2. Polygonal Surface Extraction. The ventricular cavities and epicardium of the heart CT scan of Figure 1 were delineated with a thresholding algorithm. Figure 2 shows the external faces of hexahedra with vertices crossing the 100 gray level. This results in a brick wall texture, but, as shown in *constrained surface fitting* below, the polygonal surface becomes quite smooth when triangles are extracted with a marching cube algorithm [21, 28] from the hexahedra.

Figure 2(a) illustrates the practicality of geometric model reconstruction. The two holes in the edges of the right ventricular cavity are clearly artifacts. They appeared because we did not have any voxels crossing the prescribed threshold

value. There are limits to CT, which could be compared to shadows in visible light. The reconstruction problem is partly a local operation and partly a global one. Local operations are needed to detect edges in general, but global information with a priori knowledge of the physiology is necessary to overcome limitations of local operations. Here the holes in the frontier of the RV cavity could be filled with user-assisted operations, which is time consuming. Alternatively, our approach prescribes rules to fit a smooth parametric surface on the polygonal surface. The RV displays this problem since the surfaces bounding the geometry are close to one another. However, for many problems including modeling and simulation, a smooth representation along this edge is quite adequate. Note that this problem could have potentially been eliminated by thresholding the intensity gradient instead of the absolute intensity value, or by using a more elaborate surface extraction method. However, at this stage the precision is sufficient to meet modeling needs.

As shown in Figure 2(b), when the edges of the structure imaged are not too close to one another, the surface can be accurately delineated. For example, we see very well the endocardial surface of the left ventricular cavity, even in

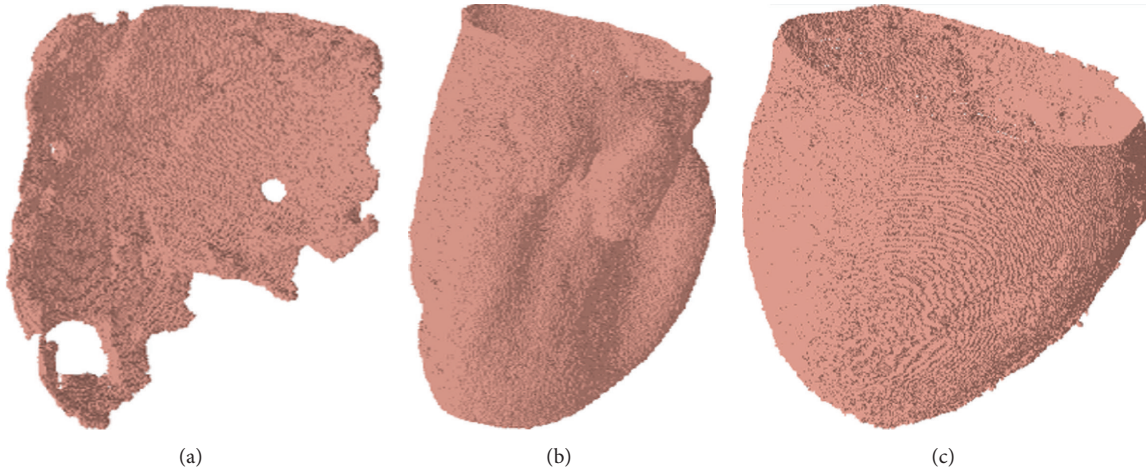


FIGURE 2: Polygonal surfaces delineating the right ventricular cavity (a) the left ventricular cavity (b), and the epicardium (c) of the mouse heart shown in Figure 1. The surfaces were extracted automatically by thresholding.

the papillary muscle region despite the fact that it is quite convoluted.

Finally, the delineation of the epicardial surface is quite trivial. Thus, as long as the imaging modality offers good contrast and surfaces are not too close to one another, they can be delineated relatively accurately with thresholding.

3.3. Polygonal Surface Projection onto a Parametric Plane. Figure 3 shows $Q(\mathcal{V})$ obtained by projecting $Q(V)$ of Figure 2 onto $(u - v)$ parametric planes. Each parametric axis has 100 units, which is arbitrary. For the projections in Figure 3, line segments of $Q(\mathcal{V})$ do not intersect and a one-to-one mapping was achieved. The epicardial surface is relatively regular and, as a result, the polygonal mesh generated by the projection is also relatively regular. The quads are more dense around the center compared to the periphery, but the difference is not very large. This is in contrast to the RV and LV surfaces. In these 2 cases, the density of quads is much larger around the center. In addition, the RV surface has several epicenters. The difference in quad density between these epicenters and the periphery is quite large, which is typical for convoluted geometries.

The RV and LV polygonal meshes illustrate well the parametric surface fitting problem. When we fit a codimension 2 parametric B-spline, the $u - v$ parametric plane is subdivided into elements of equal size. A set of geometric data points is associated to each element based on their position in the plane. This way, the coordinates of the geometric data points in high density regions are averaged, and the parametric surface cannot accurately mold the geometric data points in these regions. An increase in the number of control points can alleviate the problem, but does not solve it.

The RV polygonal mesh is particularly interesting, because the holes in the endocardial surface simply disappeared. This happened because the mapping algorithm generates a point distribution that expands in a manner to maximally fill the $u - v$ parametric plane. The outer boundary

is constrained but not the contours delimiting the holes. Thus, they are filled during the projection.

3.4. Polygonal Mesh Regularization. In order to accurately fit a parametric B-spline surface to the geometric data points, $Q(\mathcal{V})$ was regularized with respect to polygon area and edge length. To this end, we minimized a measure of variation in polygon deformation with respect to a reference polygon (7). See Appendix A for the details of this approach.

Figure 4 shows the polygonal mesh of Figure 3 after regularization. The regularized meshes are now quite uniform in polygon area and edge length. This is quite remarkable considering the initial variation in polygon density and the nonlinearity of the minimization problem. As a result of this regularization, the mapping is more conformal, and each element of the polygonal surface is given the same weight in the parametric surface fit (compare Figure 6 with Figure 5).

The polygon density of the regularized mesh is slightly higher along a diagonal in the RV surface. In order to refine regularization, one could reduce ϵ in the termination criteria $\|\mathbf{g}\|_2 < \epsilon$, though the increased number of iterations to solve the matrix system could dramatically increase the computation time (see Appendix A).

A note is in order regarding the computation time associated to with the regularization. Excluding regularization, the algorithm is quite fast; the projection and parametric surface fitting requires solving relatively simple matrix systems, both of which could be solved in the order of a second. On the other hand, the regularization is more demanding computationally since the procedure is iterative and the matrix expressing the minimization problem needs to be rebuilt at each iteration (see Appendix A). However, this task is not very time consuming if the algorithm is well implemented since most of the operations can be preprocessed.

3.5. Constrained Parametric Surface Fitting. Figures 5–8 show the parametric surfaces fitted to the geometric data points. In each panel of Figure 5, the red surfaces are composed

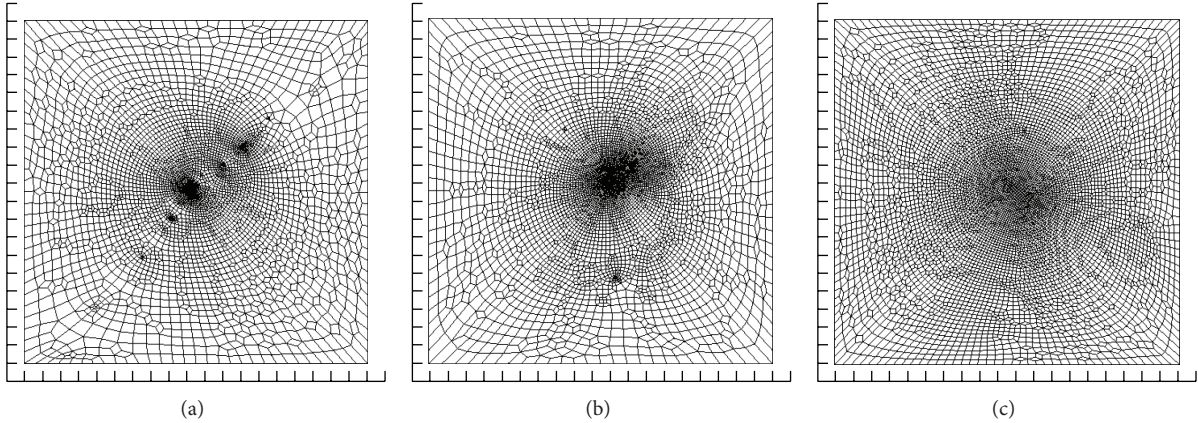


FIGURE 3: Polygonal surfaces (Figure 2), projected onto the $(u - v)$ parametric plane. The surfaces delineate the endocardial surface of the right ventricular cavity (a), the endocardial surface of left ventricular cavity (b), and the epicardial surface (c).

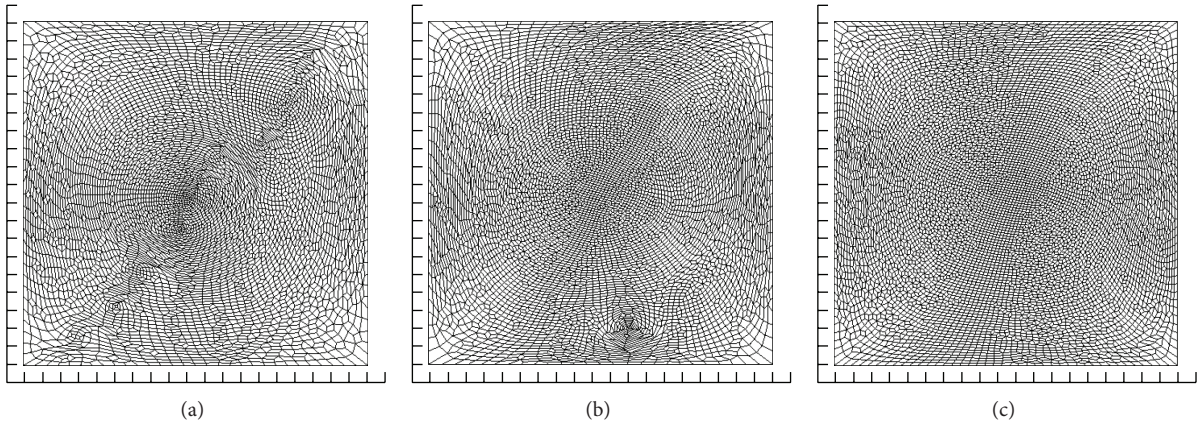


FIGURE 4: Polygonal meshes shown in Figure 3, regularized for polygons area and edges length.

of a triangle array extracted from the brick wall texture of Figure 2. The grey surfaces are the codimension 2 B-splines fitted on the geometric data points of $Q(\mathcal{V})$ of Figure 4. The fit is performed according to the algorithm presented in the Methods. Table 1 gives the parameter for the surface fits. All fits were performed by imposing a relatively low stiffness. This parameter is assigned by trial and error during visual inspection. It is convenient to proceed this way since, once the regularization completed, the fit is practically instantaneous.

As judged by Figure 5, the match between the parametric surfaces and the geometric data points is excellent. Convoluted surfaces, are accurately represented with only 9×9 elements, which is remarkable for the LV. Statistics on the distances between the parametric surface and the geometric data points are given in Table 2. Considering the number of polygons in each case (Table 1), this constitutes a dramatic reduction in the complexity of the representation and significantly impacts the computational labor of any task aiming to evaluate geometric information on this physiologic structure. Note the fit of the epicardial surface seems to be less accurate; that is, minimal, maximal, and averaged distances are larger than the one of the left and right ventricular cavities. However, also remark the variance is larger. The epicardial

TABLE 1: Parameters of the surface fitting. Number of polygons: number of polygons in the polygonal surfaces of Figure 2. N_u, N_v : number of elements along the u and v coordinates of the parametric plane. Stiffness: parameter λ in (13).

Surface	Number of polygons	N_u	N_v	Stiffness
Right ventricle	374,369	7	7	0.3
Left ventricle	377,863	9	9	0.2
Epicardium	1,013,085	11	11	0.1

surface from CT is not as smooth as the surface of the cavities. There are local variations that could not be captured with the number of elements we used.

The right side of the RV parametric surface is smoother than the triangulated surface, but this result was desirable. The computerized tomography and the surface extraction are not highly accurate in this region since the surfaces nearly intersect one another. It was judged here that the smooth surface corrects some of these errors. Note that the holes in the RV polygonal surface (Figure 5) have been filled in the parametric surface without any manual interventions. There is a steep transition in the $x - y - z$ coordinates near the holes, but they are smoothed out by the fit.

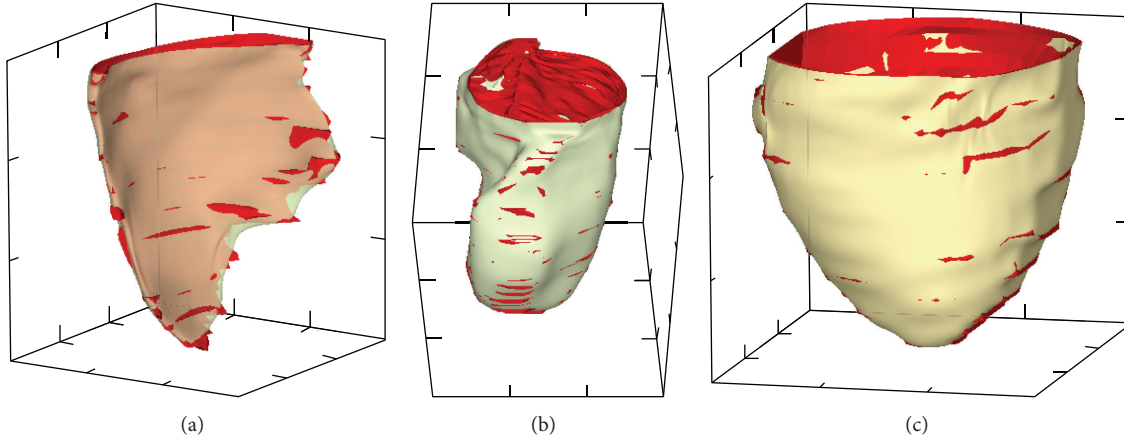


FIGURE 5: Parametric surfaces fitted to the $x - y - z$ coordinates of the regularized polygonal meshes shown in Figure 4. (a) Right ventricular cavity; (b) left ventricular cavity; (c) epicardium. Gray: parametric surface. Red: Surface composed of triangles array generated from the brick wall texture of Figure 2.

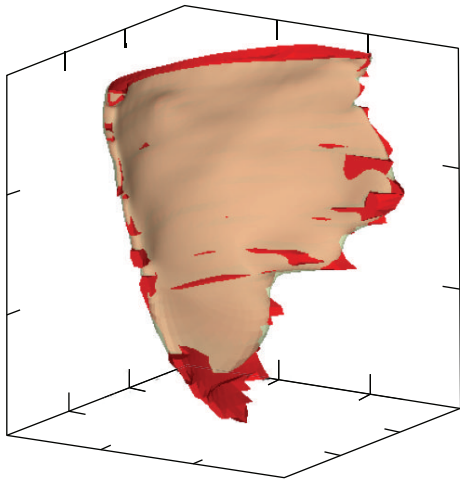


FIGURE 6: Parametric surface fitted to the $x - y - z$ coordinates of the RV polygonal mesh before regularization, that is, Figure 3(a).

TABLE 2: Min., Max., Avg. dist: minimal, maximal, and averaged distances, respectively. Distances refer to the distance between the geometric data points and the model surface, as calculated with the metric presented in Section 2. Rightmost column, variance of the distances. All distances and variance are in μm .

Surface	Min. dist.	Max. dist.	Avg. dist.	Variance
Right ventricle	0.0334	25.9825	8.0064	15.5450
Left ventricle	0.0214	32.1468	5.2053	16.4575
Epicardium	0.1198	51.9895	13.8509	53.3334

The fit of the LV surface is the most striking. The reproduction is excellent using only 9×9 elements in the parametric B-spline; this despite the fact that the surface is quite convoluted. The papillary muscle was accurately reproduced from its root in the endocardial surface all the way up to its tip near the aortic valve. Clearly the parametric surface fit is excellent. On average, the distance between

a geometric data point and the surface is less than $8.0 \mu\text{m}$, $5.2 \mu\text{m}$, and $13.8 \mu\text{m}$ for the surfaces bounding the RV cavity, LV cavity, and endocardium, respectively. In addition, we can observe the triangulated surface crossing in and out the parametric surface all around due to their proximity.

Figure 6 is a fit of the parametric surface of the RV polygonal mesh before its regularization (Figure 3). In this case, the apex is not well reproduced and important details are missed along the right side of the RV. In addition, the distance between the triangulated and parametric surfaces is larger. In this case, the triangulated and parametric surfaces do not cross one another as in Figure 5. Without regularization, the distance between the parametric surface and the geometric data can be quite large; that is, a convoluted geometry is smoothed out.

It is interesting to examine several views of the LV cavity in order to appreciate the accuracy of the reproduction, despite the convoluted nature of the geometry. Panel (a) of Figure 7 is a top view of the LV cavity exposing the papillary muscle. The surface is starting to close in its upper part because it is getting close to the heart valves. In panels (b) and (c), we have an outside view of several ridges, cavities, and protrusions.

Finally, Figure 8(a) shows a cut open view of the LV endocardial surface. The model includes protrusions, invagination, and a papillary muscle, while the surface remains smooth. Clearly, the representation is sufficiently flexible to generate a realistic model of the heart ventricles, with as few as 9×9 elements. We have not constrained the fit to the base, but could have done so. With the ability to constrain the fit on specific contours, we could have decomposed the geometric reconstruction to address more complex reconstruction problems.

Figure 8(b) is a confocal laser microscopy image of a cross-section of the heart near the root of the papillary muscle. The image was obtained at a 4x enlargement and after staining the cardiac fibers (see Methods). It illustrates how complex the subendocardial layer is. The cardiac fibers follow a feather-like pattern. They are oriented along the periphery

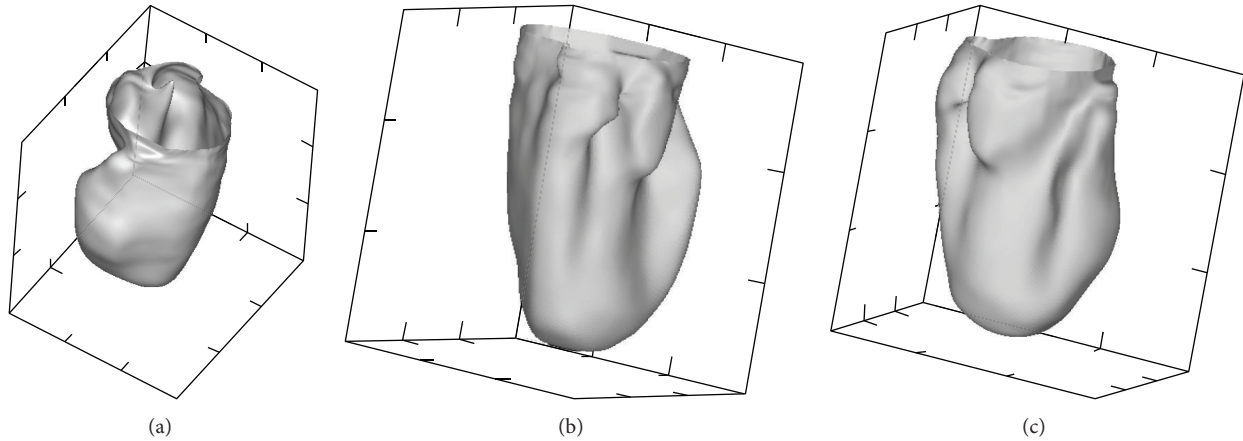


FIGURE 7: Multiple views of the parametric B-Spline surface fitted to the edge of the left ventricular cavity (Figure 2(b)).

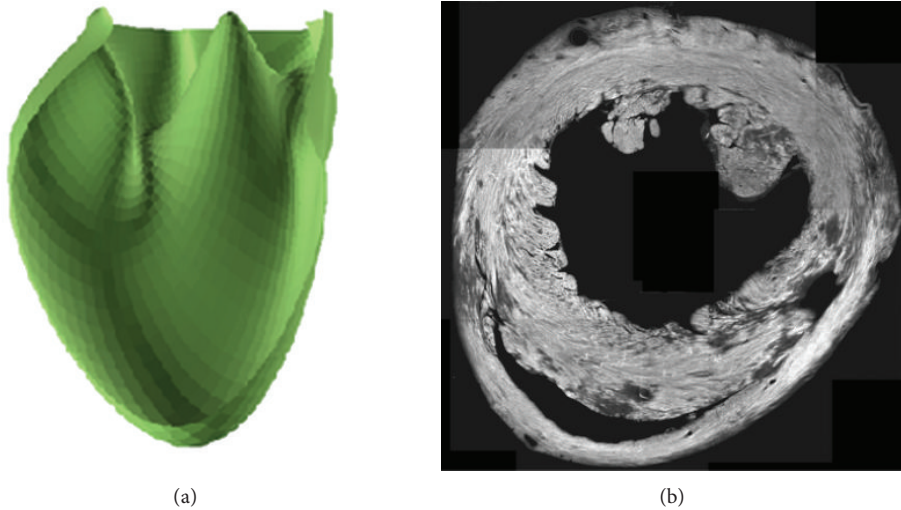


FIGURE 8: (a) Cut open view of the left ventricular cavity model, same as Figure 5(b). The view exposes the papillary muscle. (b) Laser scanning confocal microscopy image (4x enlargement) of a cross section of the same heart near the papillary muscle.

in midmyocardium, but fan out as we move toward the periphery. The fibers enter the large protrusions along their long axis. In the papillary muscle we observe dots instead of lines, because at this level the fibers are oriented along the long axis of the papillary muscle. A detailed histology study by Robinson et al. [29] corroborates this result. We can also remark that the fibers are more separated in the protrusions and papillary muscle, thereby suggesting more collagen in these areas. Thus, clearly the ventricular walls have a complex structure. The interested reader is invited to consult Slamani et al. [19], Poddar et al. [20], and Subramanian et al. [30] for a high resolution three-dimensional reconstruction of cardiac fiber orientations based on laser scanning confocal microscopy data.

4. Discussion

4.1. Motivation for the Developed Technique. What motivated the developed technique was the specifications for geometric

models employed to study problems in cardiac electrophysiology with computer simulations. Now that we illustrated a reconstruction with our method, we can elaborate on its application in investigative cardiology.

Several cardiac arrhythmias are initiated by an abnormal heart beat originating in the ventricles. The initiation site of these beats remains mysterious for a number of arrhythmias like congenital arrhythmias (e.g., Long QT syndrome), idiopathic ventricular tachycardias (IVT), catecholaminergic ventricular tachycardias (CVT), and many others. It is likely that the triggering of abnormal beats occurs at sites displaying steep changes in electrical conduction because such sites are associated with local changes in propagation velocity, action potential duration (wave may pivot), and spatiotemporal distribution of intracellular calcium. All of which may favor wavefront and wavetail interactions, and in turn, the triggering of abnormal beats.

The root of large protrusions, the root of heart valves, the fascicles, the outflow tract, or any other convoluted region can display the above mentioned characteristics. There are

two main reasons for this. First, these sites exhibit rapid changes in fiber orientation. For example, cardiac fibers are oriented along the tangent to the heart circumference in midmyocardium, but along the long axis of the protrusions, which implies a steep change in cardiac fiber orientation around the root of the protrusions. Second, in many instances these sites have higher collagen density because they play a structural role. Therefore, there is a need to investigate the role played by these sites in electrical conduction at a mesoscopic scale.

Cardiac modeling is definitively a good instrument for such investigation as it allows reconstructing electrical excitation from the ground up, and then studying the interplay between several contributing factors. The technique presented here offers the flexibility necessary for geometric heart reconstruction at the mesoscopic scale and all elements required for the formulation of an accurate electrical conduction model. Note that to perform simulations, one should add to the geometry a mathematical description of fiber and lamina orientations. An interesting technique to accomplish this, also based on C_2 parametric representation, was documented by Bayer et al. [31].

4.2. Advantages and Limitations of Our Geometric Modeling Technique. We have presented a method to fit C^2 continuous parametric surfaces to scattered geometric data points on frontiers delimiting physiologic structures. Such surfaces meet the modeling needs stated above. So far the best way to generate them was through deformable models or level set methods. The approach we presented here is more direct and is likely to perform better. Briefly, once a polygonal surface is extracted from a segmented image, it is projected onto a parametric plane. The resulting polygonal mesh is regularized for polygon area and edge length. Then a parametric surface is fitted to the projected geometric data points, whose operation also assigns a unique parametric coordinate to each data point. The fit requires to adjust the control points of a codimension 2 B-spline in a manner to minimize the distance between the geometric data point and points on the surface with the same parametric coordinate. The computational load is relatively small. The projection and parametric surface fit necessitate solving a symmetric sparse matrix system with small bandwidth. When the polygonal surface is composed of quads, $N_d \times 9$ coefficients, N_d : number of data points for the projection and $N_b \times 49$ coefficients N_b : number of B-spline coefficients for the fit. These matrix systems can be solved in the order of seconds. The regularization is the time limiting step. It requires finding a function minimum. This is done with an iterative method, where each step includes the calculation of matrix coefficients and matrix-to-vector multiplications. The matrix in question is sparse and has a small bandwidth (dimension: $N_d \times 9$ coefficients with quads).

Our results show it is possible to represent convoluted geometries in a compact manner with codimension 2 parametric B-splines. Specifically, a representation with 9×9 elements, or 121 control points, are sufficient to accurately describe the LV, including protrusions, invaginations, and even a papillary muscle.

The examination of advantages and disadvantages of this approach has to be contextualized. A reconstruction technique can serve several purposes, for example, visualize a structure, detect features, measure areas and volumes, or investigate the role played by geometry with modeling and simulations. Obviously, each technique has advantages with respect to the targeted use. For visualization, when the image is not noisy and the contrast is high, thresholding with polygonal surface extraction is simple and fast, which meets the needs of this task. However, when the image is noisy the manual assistance required may make the technique too time consuming to be practical. A deformable model or a level set method would be more appropriate in this case. When there is too much noise, or the contrast is low, a technique replacing or adding to the function to minimize a comparison of each pixel's intensity with the averaged intensity of pixels inside and outside regions delimited by the moving boundary [14] is quite effective. However, this is done at the cost of a significant additional computational load. Still, this may be beneficial considering the manual labor involved by the alternative. In addition, for many tasks batch processing is quite acceptable. When one needs to perform measurements on the geometric reconstruction, as in oncology since the rate of uptake of a compound may depend on surface and dose on volume, then a mathematical representation amenable to such computation offers important advantages. Surfaces can be easily computed with triangle arrays. Deformable and level set methods can both provide such representation; however, the level set method necessitates an additional step to extract the surface. The calculation of volumes is more delicate. In this case a parametric representation dramatically facilitates this calculation. This also applies to the calculations required in modeling and simulations. Indeed, in this case the availability of C_2 continuous surfaces is a great advantage since in addition to volume, precise calculations of curvature, distances on curved surfaces, and areas of curvilinear surfaces are needed. Such representation can be built with the deformable model or level set methods, but could significantly complicate the process. Alternatively, it could be included as a postprocessing operation, but as explained in the Introduction and Methods, it is not trivial to generate the C_2 continuous parametric surface even when we know the frontier of the object in question. This is precisely the problem our technique addresses.

When the noise level is low and the contrast is high, which is the case for a large number of medical imaging modalities, the geometric reconstruction can be performed with thresholding and polygonal surface extraction followed with a fit of a C_2 continuous surface like we did here. The computational load is minimal, results are obtained rapidly, and as illustrated here, accuracy is excellent. When the noise level is high or contrast is low, it would become advantageous to replace thresholding and polygonal surface extraction with a deformable model or a level set method. No need to say automaticity and robustness will come at the price of significant additional computational load.

Lastly, another limitation of our method is that the computational load rapidly increases with problem size. However, this can be addressed by decomposing the reconstruction

problem. This means identifying, from the surface extraction, critical sections where the geometric model could be split, then fitting the border of these sections with C_2 codimension 1 parametric B-splines to fit each portion separately by imposing the fitted surface to match the boundary curves. This could be further constrained by imposing a continuous surface normal orientation.

4.3. *The Future of Medicine.* With the use of imaging and genomic data, medicine is becoming more and more quantitative. This is to our benefit since it has significantly advanced diagnostics and the optimization of a number of therapeutic interventions. Nevertheless, there may be even more with the introduction of advanced computation; that is, modeling and simulations can provide unprecedented means to discover mechanisms of diseases.

As stated in “*motivation for the technique developed*”, we expect heart geometry and cardiac tissue microstructure to play an important role in the initiation of fatal arrhythmias. However, this role needs to be precisely discovered. Considering the unknown, it is appealing to approach this problem from the population scale, that is, finding in the population trends between symptoms or triggering conditions, with geometry and microstructure features. Considering the clinical data and the computational resources available to date, it is not unrealistic to attempt to tackle the problem this way.

First, it is common practice for any patient displaying recurrent episodes of tachycardia or syncopies to have a CT or MR or both scans. We could perform geometric heart reconstructions for this population, but this would require the reconstruction procedure to be automatic. Fortunately, such problem has been previously addressed. Few reconstructions are performed for cases displaying different geometries/microstructures. These reconstructions form an atlas which constitutes a basis of information that drives the automatic reconstructions. The approach is based on the *active shape modeling* introduced by Cootes et al. [32]. The variance of predefined markers coordinates are captured in a covariance matrix (our reconstruction method would facilitate this task). The first few eigenvectors corresponding to the largest eigenvalues of the covariance matrix provide axes to guide the constrained deformations. Indeed Frangi et al. [33] and Zheng et al. [34] built on this concept to develop elaborate computational infrastructure to reconstruct heart models automatically. Zheng et al. [34] even supplemented the technique with learning algorithms to generate classes of geometric models semiautomatically.

Once the reconstruction is performed at the population scale, features associated to electrophysiologic properties could be captured in several parameters. Then based on these parameters, model categories can be generated automatically with a classifier. In a subsequent step, correlations could be drawn between categories and conditions of initiation of arrhythmias. This specifies a number of parameters for the performance of elaborate simulations aiming at finding the causes triggering life threatening arrhythmias. The computational resources required for such an endeavor are

considerable, but available at supercomputer centers. Such efforts could lead to the systematic discovery of mechanisms of arrhythmias, and in turn equip clinicians with new means to prevent life threatening arrhythmias and to optimize medical devices.

Appendix

A. Numerical Solution of the Grid Regularization Equation

A.1. *Quadrilateral Mesh.* We minimize $F(\mathbf{u}, \mathbf{v})$

$$F(\mathbf{u}, \mathbf{v}) = \sum_{e=0}^{N_e-1} \sum_{i=0}^1 \sum_{j=0}^1 \int_{\Omega_e} [r_{i,j}^{(e)}]^2 d\Omega, \quad (\text{A.1})$$

$$\mathbf{R}^{(e)} = \mathcal{F}^{(e)} - \frac{\text{Adj}\{\mathcal{F}^{(e)}\}}{|\mathcal{F}^{(e)}|},$$

where

$$\mathcal{F}^{(e)} = \begin{bmatrix} U_\xi^{(e)} & U_\eta^{(e)} \\ V_\xi^{(e)} & V_\eta^{(e)} \end{bmatrix}, \quad \text{Adj}\{\mathcal{F}\} = \begin{bmatrix} V_\eta^{(e)} & -U_\eta^{(e)} \\ -V_\xi^{(e)} & U_\xi^{(e)} \end{bmatrix},$$

$$\mathcal{F}^{(e)} = U_\xi^{(e)} V_\eta^{(e)} - U_\eta^{(e)} V_\xi^{(e)}, \quad (\text{A.2})$$

with respect to (\mathbf{u}, \mathbf{v}) . Above the mapping functions are described with degree 1 Lagrange polynomials,

$$U^{(e)}(\xi, \eta) = \sum_{i=0}^3 u_i^{(e)} \Psi_i(\xi, \eta), \quad (\text{A.3})$$

$$V^{(e)}(\xi, \eta) = \sum_{i=0}^3 v_i^{(e)} \Psi_i(\xi, \eta),$$

built with tensor product of one-dimensional Lagrange polynomials,

$$\Psi(\xi, \eta) = \psi(\xi) \otimes \psi(\eta),$$

$$\psi(\xi) = [\psi_0(\xi), \psi_1(\xi)], \quad (\text{A.4})$$

$$\psi_0(\xi) = \frac{1-\xi}{2}, \quad \psi_1(\xi) = \frac{\xi-1}{2}.$$

We find this minimum with a fixed point method. To this end, $F(\mathbf{u}, \mathbf{v})$ is approximated ($\tilde{F}(\mathbf{u}, \mathbf{v})$) around $(\mathbf{u}_0, \mathbf{v}_0)$ with a multidimensional quadratic

$$\tilde{F}(\mathbf{u}, \mathbf{v}) = \frac{1}{2} (\mathbf{u} - \mathbf{u}_0, \mathbf{v} - \mathbf{v}_0)^T \mathbf{H} (\mathbf{u} - \mathbf{u}_0, \mathbf{v} - \mathbf{v}_0) + \mathbf{g}^T (\mathbf{u} - \mathbf{u}_0, \mathbf{v} - \mathbf{v}_0) + F(\mathbf{u}_0, \mathbf{v}_0) \quad (\text{A.5})$$

admitting its minimum at

$$\mathbf{H} \begin{bmatrix} \mathbf{u} \\ \mathbf{v} \end{bmatrix} = \mathbf{g}, \quad (\text{A.6})$$

where \mathbf{H} and \mathbf{g} are the Hessian (also called the Jacobian) and gradient of $F(\mathbf{u}, \mathbf{v})$ evaluated at $(\mathbf{u}_0, \mathbf{v}_0)$.

The gradient $\mathbf{g}^{(e)} \in \mathfrak{R}^8$ of an element “e”

$$\mathbf{g}^{(e)} = \left(\frac{\partial F^{(e)}}{\partial u_\alpha^{(e)}}, \frac{\partial F^{(e)}}{\partial v_\alpha^{(e)}} \right)^T, \quad \alpha \in [0, 3] \quad (\text{A.7})$$

is calculated taking the derivative of each component of $\mathbf{R}^{(e)}$

$$\begin{aligned} r_{0,0}^{(e)} &= U_\xi^{(e)} - \frac{V_\eta^{(e)}}{(U_\xi^{(e)} V_\eta^{(e)} - U_\eta^{(e)} V_\xi^{(e)})}, \\ r_{0,1}^{(e)} &= U_\eta^{(e)} - \frac{U_\eta^{(e)}}{(U_\xi^{(e)} V_\eta^{(e)} - U_\eta^{(e)} V_\xi^{(e)})}, \\ r_{1,0}^{(e)} &= U_\xi^{(e)} - \frac{V_\xi^{(e)}}{(U_\xi^{(e)} V_\eta^{(e)} - U_\eta^{(e)} V_\xi^{(e)})}, \\ r_{1,1}^{(e)} &= U_\xi^{(e)} - \frac{U_\xi^{(e)}}{(U_\xi^{(e)} V_\eta^{(e)} - U_\eta^{(e)} V_\xi^{(e)})}, \end{aligned} \quad (\text{A.8})$$

with respect to $\mathbf{u}^{(e)}, \mathbf{v}^{(e)}$, that is,

$$\begin{aligned} \frac{\partial F^{(e)}}{\partial u_\alpha^{(e)}} &= \sum_i \sum_j \int_{-1}^1 \int_{-1}^1 2r_{i,j}^{(e)} \left(\frac{\partial r_{i,j}^{(e)}}{\partial u_\alpha^{(e)}} \right) d\xi d\eta \\ \frac{\partial F^{(e)}}{\partial v_\alpha^{(e)}} &= \sum_i \sum_j \int_{-1}^1 \int_{-1}^1 2r_{i,j}^{(e)} \left(\frac{\partial r_{i,j}^{(e)}}{\partial v_\alpha^{(e)}} \right) d\xi d\eta, \end{aligned} \quad (\text{A.9})$$

with

$$\begin{aligned} \frac{\partial r_{i,j}^{(e)}}{\partial u_\alpha^{(e)}} &= \frac{\partial r_{i,j}^{(e)}}{\partial U_\xi^{(e)}} \frac{\partial \Psi_\alpha}{\partial \xi} + \frac{\partial r_{i,j}^{(e)}}{\partial U_\eta^{(e)}} \frac{\partial \Psi_\alpha}{\partial \eta}, \\ \frac{\partial r_{i,j}^{(e)}}{\partial v_\alpha^{(e)}} &= \frac{\partial r_{i,j}^{(e)}}{\partial V_\xi^{(e)}} \frac{\partial \Psi_\alpha}{\partial \xi} + \frac{\partial r_{i,j}^{(e)}}{\partial V_\eta^{(e)}} \frac{\partial \Psi_\alpha}{\partial \eta}. \end{aligned} \quad (\text{A.10})$$

Once $\mathbf{g}^{(e)}$ is evaluated, it is added to \mathbf{g} with appropriate embedding based on $C(Q)$.

Similarly, the Hessian $\mathbf{H}^{(e)} \in \mathfrak{R}^{8 \times 8}$ of an element “e,”

$$\mathbf{H}^{(e)} = \begin{bmatrix} \frac{\partial}{\partial u_\beta^{(e)}} \left(\frac{\partial F^{(e)}}{\partial u_\alpha^{(e)}} \right) & \frac{\partial}{\partial u_\beta^{(e)}} \left(\frac{\partial F^{(e)}}{\partial v_\alpha^{(e)}} \right) \\ \frac{\partial}{\partial v_\beta^{(e)}} \left(\frac{\partial F^{(e)}}{\partial u_\alpha^{(e)}} \right) & \frac{\partial}{\partial v_\beta^{(e)}} \left(\frac{\partial F^{(e)}}{\partial v_\alpha^{(e)}} \right) \end{bmatrix}, \quad (\text{A.11})$$

$$\alpha, \beta \in [0, 3],$$

is obtained taking the derivative of (A.9) with respect to $\mathbf{u}^{(e)}, \mathbf{v}^{(e)}$,

$$\begin{aligned} &\frac{\partial}{\partial u_\beta^{(e)}} \left(\frac{\partial F^{(e)}}{\partial u_\alpha^{(e)}} \right) \\ &= \sum_i \sum_j \int_{-1}^1 \int_{-1}^1 2 \left[\left(\frac{\partial r_{i,j}^{(e)}}{\partial u_\beta^{(e)}} \frac{\partial r_{i,j}^{(e)}}{\partial u_\alpha^{(e)}} \right) \right. \\ &\quad \left. + r_{i,j}^{(e)} \left(\frac{\partial^2 r_{i,j}^{(e)}}{\partial u_\beta^{(e)} \partial u_\alpha^{(e)}} \right) \right] d\xi d\eta, \end{aligned}$$

$$\begin{aligned} &\frac{\partial}{\partial u_\beta^{(e)}} \left(\frac{\partial F^{(e)}}{\partial v_\alpha^{(e)}} \right) \\ &= \sum_i \sum_j \int_{-1}^1 \int_{-1}^1 2 \left[\left(\frac{\partial r_{i,j}^{(e)}}{\partial u_\beta^{(e)}} \frac{\partial r_{i,j}^{(e)}}{\partial v_\alpha^{(e)}} \right) \right. \\ &\quad \left. + r_{i,j}^{(e)} \left(\frac{\partial^2 r_{i,j}^{(e)}}{\partial u_\beta^{(e)} \partial v_\alpha^{(e)}} \right) \right] d\xi d\eta, \end{aligned}$$

$$\frac{\partial}{\partial v_\beta^{(e)}} \left(\frac{\partial F^{(e)}}{\partial u_\alpha^{(e)}} \right) = \left[\frac{\partial}{\partial u_\beta^{(e)}} \left(\frac{\partial F^{(e)}}{\partial v_\alpha^{(e)}} \right) \right]^T$$

$$\begin{aligned} &\frac{\partial}{\partial v_\beta^{(e)}} \left(\frac{\partial F^{(e)}}{\partial v_\alpha^{(e)}} \right) \\ &= \sum_i \sum_j \int_{-1}^1 \int_{-1}^1 2 \left[\left(\frac{\partial r_{i,j}^{(e)}}{\partial v_\beta^{(e)}} \frac{\partial r_{i,j}^{(e)}}{\partial v_\alpha^{(e)}} \right) \right. \\ &\quad \left. + r_{i,j}^{(e)} \left(\frac{\partial^2 r_{i,j}^{(e)}}{\partial v_\beta^{(e)} \partial v_\alpha^{(e)}} \right) \right] d\xi d\eta \end{aligned} \quad (\text{A.12})$$

with

$$\begin{aligned} &\frac{\partial^2 r_{i,j}^{(e)}}{\partial u_\beta^{(e)} \partial u_\alpha^{(e)}} \\ &= \left(\frac{\partial \Psi_\beta}{\partial \xi} \frac{\partial \Psi_\alpha}{\partial \xi} \right) \frac{\partial^2 r_{i,j}^{(e)}}{\partial U_\xi^{(e)} \partial U_\xi^{(e)}} \\ &\quad + \left(\frac{\partial \Psi_\beta}{\partial \eta} \frac{\partial \Psi_\alpha}{\partial \xi} \right) \frac{\partial^2 r_{i,j}^{(e)}}{\partial U_\xi^{(e)} \partial U_\eta^{(e)}} \\ &\quad + \left(\frac{\partial \Psi_\beta}{\partial \xi} \frac{\partial \Psi_\alpha}{\partial \eta} \right) \frac{\partial^2 r_{i,j}^{(e)}}{\partial U_\xi^{(e)} \partial U_\eta^{(e)}} \end{aligned}$$

$$\begin{aligned}
& + \left(\frac{\partial \Psi_\beta}{\partial \eta} \frac{\partial \Psi_\alpha}{\partial \eta} \right) \frac{\partial^2 r_{i,j}^{(e)}}{\partial U_\eta^{(e)} U_\eta^{(e)}}, \\
& \frac{\partial^2 r_{i,j}^{(e)}}{\partial u_\beta^{(e)} \partial v_\alpha^{(e)}} \\
& = \left(\frac{\partial \Psi_\beta}{\partial \xi} \frac{\partial \Psi_\alpha}{\partial \xi} \right) \frac{\partial^2 r_{i,j}^{(e)}}{\partial V_\xi^{(e)} \partial U_\xi^{(e)}} \\
& + \left(\frac{\partial \Psi_\beta}{\partial \eta} \frac{\partial \Psi_\alpha}{\partial \xi} \right) \frac{\partial^2 r_{i,j}^{(e)}}{\partial V_\eta^{(e)} \partial U_\eta^{(e)}} \\
& + \left(\frac{\partial \Psi_\beta}{\partial \xi} \frac{\partial \Psi_\alpha}{\partial \eta} \right) \frac{\partial^2 r_{i,j}^{(e)}}{\partial V_\xi^{(e)} \partial U_\eta^{(e)}} \\
& + \left(\frac{\partial \Psi_\beta}{\partial \eta} \frac{\partial \Psi_\alpha}{\partial \eta} \right) \frac{\partial^2 r_{i,j}^{(e)}}{\partial V_\eta^{(e)} U_\eta^{(e)}}, \\
& \frac{\partial^2 r_{i,j}^{(e)}}{\partial v_\beta^{(e)} \partial v_\alpha^{(e)}} \\
& = \left(\frac{\partial \Psi_\beta}{\partial \xi} \frac{\partial \Psi_\alpha}{\partial \xi} \right) \frac{\partial^2 r_{i,j}^{(e)}}{\partial V_\xi^{(e)} \partial V_\xi^{(e)}} \\
& + \left(\frac{\partial \Psi_\beta}{\partial \eta} \frac{\partial \Psi_\alpha}{\partial \xi} \right) \frac{\partial^2 r_{i,j}^{(e)}}{\partial V_\xi^{(e)} \partial V_\eta^{(e)}} \\
& + \left(\frac{\partial \Psi_\beta}{\partial \xi} \frac{\partial \Psi_\alpha}{\partial \eta} \right) \frac{\partial^2 r_{i,j}^{(e)}}{\partial V_\xi^{(e)} \partial V_\eta^{(e)}} \\
& + \left(\frac{\partial \Psi_\beta}{\partial \eta} \frac{\partial \Psi_\alpha}{\partial \eta} \right) \frac{\partial^2 r_{i,j}^{(e)}}{\partial V_\eta^{(e)} V_\eta^{(e)}}.
\end{aligned} \tag{A.13}$$

Once evaluated, $\mathbf{H}^{(e)}$ is added to \mathbf{H} with appropriate embedding as specified by $C(Q)$. The derivatives with respect to $U_\xi^{(e)}$, $U_\eta^{(e)}$, $V_\xi^{(e)}$, $V_\eta^{(e)}$ are known analytically from (A.8) and derivatives of $\Psi(\xi, \eta)$ with respect to ξ , η are linear in η , ξ .

All integrals are evaluated numerically with a Gauss-Legendre quadrature. We use 5 sampling points in each direction. The Vectors Ψ and their derivative are evaluated once and stored in memory. Then the solution proceeds as follows. Solve (A.6) for $(\mathbf{u} - \mathbf{u}_0, \mathbf{v} - \mathbf{v}_0)$, $(\mathbf{u}, \mathbf{v}) \rightarrow (\mathbf{u}_0, \mathbf{v}_0)$, rebuild \mathbf{g} , \mathbf{H} , and keep iterating until $\|\mathbf{g}\|_2 < \epsilon$.

A.2. Triangular Mesh. The algorithm for a triangular mesh is obtained replacing the quad mapping functions with triangle mapping functions (triangle to triangle). With quads

Ψ is built with a tensor product of elementary Lagrange polynomials. Instead with triangles,

$$\begin{aligned}
U^{(e)}(\xi, \eta) &= \sum_{i=0}^2 u_i^{(e)} \Psi_i(\xi, \eta), \\
V^{(e)}(\xi, \eta) &= \sum_{i=0}^2 v_i^{(e)} \Psi_i(\xi, \eta), \\
\Psi_0(\xi, \eta) &= 1 - (\xi + \eta), \\
\Psi_1(\xi, \eta) &= \xi, \\
\Psi_2(\xi, \eta) &= \eta
\end{aligned} \tag{A.14}$$

and one of the bound of integration in the $\xi - \eta$ plane varies with one variable

$$\int_{\eta=0}^{\eta=1} \int_{\xi=0}^{\xi=1-\eta} f(\xi, \eta) d\xi d\eta. \tag{A.15}$$

This is quite conventional in finite element computation. The reader is referred to a finite element method textbook for more details on the subject. Indeed a good coverage of the subject can be found in Huebner et al. [35, Chapter 5]. Then embedding of the elementary vectors and matrices in the global matrix is done as specified by $C(T)$. All the rest of the algorithm is the same as for the treatment of the quadrilateral mesh.

B. Imposition of Boundary Conditions on Codimension 2 B-Splines

Consider the specific case illustrated in Figure 9. The parametric plane $(u - v)$ is subdivided in 7 elements. The control points (blue) and elements (red) are numbered according to the directions of the $u - v$ axes, u -coordinate first then v . Two additional rows and columns of control points are added along the edges of the plane to ensure the B-Spline on boundary elements are represented with the same degrees of freedom as the other elements inside the plane. When assigning boundary conditions we fix values on these control points.

We clamp the edge $u = 0$ of the parametric plane with a contour $\ell(v)$. A codimension 1 B-spline is fitted to this contour. The parametric axis of this B-Spline is displayed on the left side, with elements and control points number in orange and green, respectively. This parametric axis is identical to the edge $u = 0$ of the $u - v$ plane, that is, same length, same number of segments, each of them having the same length. The reader's attention is drawn to element 1 of the contour which corresponds to 7 in the plane. The part of the codimension 1 B-spline expansion contributing to this edge $\ell^{(1)}(v)$ is

$$\begin{aligned}
\ell^{(1)}(v) &= \rho_1 b_0(\bar{v}) + \rho_2 b_1(\bar{v}) + \rho_3 b_2(\bar{v}) \\
&+ \rho_4 b_3(\bar{v}), \\
\bar{v} &= 2v - \frac{v_3 + v_2}{(v_3 - v_2)}.
\end{aligned} \tag{B.1}$$

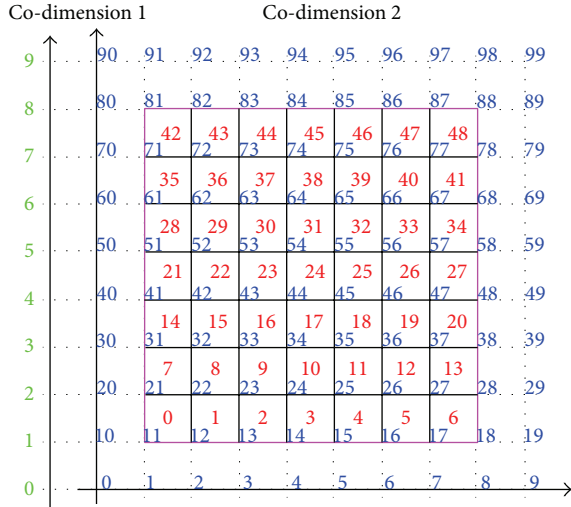


FIGURE 9: Parametric plane subdivided into 7×7 elements. Red labels: elements number. Blue labels: control points number. The border of the $u - v$ parametric plane is in magenta.

On any horizontal line, $\mathbf{b}(u = 0)$ take the values $(1/6, 2/3, 1/6, 0)$. Thus the part of codimension 2 B-Spline expansion contributing to this edge is

$$\begin{aligned}
 \ell^{(1)}(v) &= \frac{1}{6}\zeta_{10}b_0(\bar{v}) + \frac{2}{3}\zeta_{11}b_0(\bar{v}) + \frac{1}{6}\zeta_{12}b_0(\bar{v}) \\
 &+ \frac{1}{6}\zeta_{20}b_1(\bar{v}) + \frac{2}{3}\zeta_{21}b_1(\bar{v}) + \frac{1}{6}\zeta_{22}b_1(\bar{v}) \quad (\text{B.2}) \\
 &+ \frac{1}{6}\zeta_{30}b_2(\bar{v}) + \frac{2}{3}\zeta_{31}b_2(\bar{v}) + \frac{1}{6}\zeta_{32}b_2(\bar{v}) \\
 &+ \frac{1}{6}\zeta_{40}b_3(\bar{v}) + \frac{2}{3}\zeta_{41}b_3(\bar{v}) + \frac{1}{6}\zeta_{42}b_3(\bar{v}).
 \end{aligned}$$

We Fix the coefficients on the boundary layer of the codimension 2 B-spline such that the coefficients factoring the same $b_i(v)$ $i \in [0, 3]$ in the codimension 1 and 2 B-splines are identical. This leads to

$$\begin{bmatrix} \frac{\zeta_{10}}{6} \\ \frac{\zeta_{20}}{6} \\ \frac{\zeta_{30}}{6} \\ \frac{\zeta_{40}}{6} \end{bmatrix} = \begin{bmatrix} \rho_1 \\ \rho_2 \\ \rho_3 \\ \rho_4 \end{bmatrix} - \begin{bmatrix} \frac{2}{3}\zeta_{11} + \frac{1}{6}\zeta_{12} \\ \frac{2}{3}\zeta_{21} + \frac{1}{6}\zeta_{22} \\ \frac{2}{3}\zeta_{31} + \frac{1}{6}\zeta_{32} \\ \frac{2}{3}\zeta_{41} + \frac{1}{6}\zeta_{42} \end{bmatrix} \quad (\text{B.3})$$

a similar condition applies to the sides of the boundary elements along $u = 0$. An elementary B-spline on the codimension 1 contour has exactly 3 matching elementary B-splines on the codimension 2 surface, and their coefficients should be equal.

The boundary coefficients as determined by algebraic relation (B.3) for each boundary elements are introduced

in the codimension 2 B-spline, eliminating the boundary layer from the codimension 2 expansion. The surface is fitted with this new system of equations. This condition guarantees the surface to exactly match the contour. As a rule we reintroduced the boundary layer coefficients in the original form of the codimension 2 expansion where each ζ_s factors a $B_s(u, v)$. This way all B-spline expansions always have the same format no matter what boundary conditions have been imposed to them.

Conflict of Interests

The authors declare that there are no conflict of interests regarding the publication of this paper.

Acknowledgments

Work is supported by NSF TeraGrid Grant no. BCS110013 to Jacques Beaumont, and in part by the French Government through the Agence Nationale de la Recherche (<http://www.agence-nationale-recherche.fr/>) program “Investissements d’avenir” with Grant ANR-10-IAHU-04 and funding provided by the Whitaker International Program administered by the Institute of International Education to Jason D. Bayer. The authors thank Arkady Pertsov professor of Pharmacology at SUNY Upstate Medical University, Andrzej Krol professor of Radiology at SUNY Upstate Medical University, and Anthony Costantino, research assistant at Binghamton University for editorial comments.

References

- [1] G. Plank, R. A. B. Burton, P. Hales et al., “Generation of histologically representative models of the individual heart: tools and application,” *Philosophical Transactions of the Royal Society A*, vol. 367, no. 1896, pp. 2257–2292, 2009.
- [2] N. A. Trayanova, “Whole-heart modeling : applications to cardiac electrophysiology and electromechanics,” *Circulation Research*, vol. 108, no. 1, pp. 113–128, 2011.
- [3] J. V. Tranquillo, J. Hlavacek, and C. S. Henriquez, “An integrative model of mouse cardiac electrophysiology from cell to torso,” *Europace*, vol. 7, supplement 2, pp. S56–S70, 2005.
- [4] D. M. Harrild and C. S. Henriquez, “A computer model of normal conduction in the human atria,” *Circulation research*, vol. 87, no. 7, pp. e25–e36, 2000.
- [5] F. Vadakkumpadan, L. J. Rantner, B. Tice et al., “Image-based models of cardiac structure with applications in arrhythmia and defibrillation studies,” *Journal of Electrocardiology*, vol. 42, no. 2, pp. 157.e1–157.e10, 2009.
- [6] V. J. Wedeen, D. L. Rosene, R. Wang et al., “The geometric structure of the brain fiber pathways,” *Science*, vol. 335, no. 6076, pp. 1628–1634, 2012.
- [7] M. Lee, W. Cho, S. Kim, S. Park, and J. H. Kim, “Segmentation of interest region in medical volume images using geometric deformable model,” *Computers in Biology and Medicine*, vol. 42, no. 5, pp. 523–537, 2012.
- [8] J. Lefèvre and J. -F. Mangin, “A reaction-diffusion model of human brain development,” *PLoS Computational Biology*, vol. 6, no. 4, Article ID e1000749, 2010.

- [9] B. Jüttler and A. Felis, "Least-squares fitting of algebraic spline surfaces," *Advances in Computational Mathematics*, vol. 17, no. 1-2, pp. 135–152, 2002.
- [10] M. Kass, A. Witkin, and D. Terzopoulos, "Snakes: active contour models," *International Journal of Computer Vision*, vol. 1, no. 4, pp. 321–331, 1988.
- [11] T. McInerney and D. Terzopoulos, "Deformable models in medical image analysis: a survey," *Medical Image Analysis*, vol. 1, no. 2, pp. 91–108, 1996.
- [12] T. McInerney and D. Terzopoulos, "Topology adaptive deformable surfaces for medical image volume segmentation," *IEEE Transactions on Medical Imaging*, vol. 18, no. 10, pp. 840–850, 1999.
- [13] D. N. Metaxas, T. Chen, and A. K. Peters, "Deformable Models," in *Insight Into Images: Principles and Practice for Segmentation, Registration, and Image Analysis*, T. S. Yoo, Ed., Lavoisier, Paris, France, 2004.
- [14] T. F. Chan and L. A. Vese, "Active contours without edges," *IEEE Transactions on Image Processing*, vol. 10, no. 2, pp. 266–277, 2001.
- [15] K. Park, A. Montillo, D. Metaxas, and L. Axel, "Volumetric heart modelling and analysis," *Communications of the ACM*, vol. 48, no. 2, pp. 43–48, 2005.
- [16] Z. Ma, J. M. R. S. Tavares, R. N. Jorge, and T. Mascarenhas, "A review of algorithms for medical image segmentation and their applications to the female pelvic cavity," *Computer Methods in Biomechanics and Biomedical Engineering*, vol. 13, no. 2, pp. 235–246, 2010.
- [17] I. A. Feldkamp, L. C. Davis, and J. W. Kress, "Practical cone-beam algorithm," *Journal of the Optical Society of America A*, vol. 1, no. 6, pp. 612–619, 1984.
- [18] J. D. Bayer, J. Beaumont, and A. Krol, "Laplace-Dirichlet energy field specification for deformable models. An FEM approach to active contour fitting," *Annals of Biomedical Engineering*, vol. 33, no. 9, pp. 1175–1186, 2005.
- [19] M.-A. Slamani, A. Krol, J. Beaumont, R. L. Price, I. L. Coman, and E. D. Lipson, "Application of phase correlation to the montage synthesis and three-dimensional reconstruction of large tissue volumes from confocal laser scanning microscopy," *Microscopy and Microanalysis*, vol. 12, no. 2, pp. 106–112, 2006.
- [20] A. H. Poddar, A. Krol, J. Beaumont et al., "Ultrahigh resolution 3D model of murine heart from micro-CT and serial confocal laser scanning microscopy images," in *Proceedings of the IEEE Nuclear Science Symposium Conference Record*, vol. 5, pp. 2615–2617, Fajardo, Puerto Rico, October 2005.
- [21] W. E. Lorensen and H. E. Cline, "Marching cubes: a high resolution 3D surface construction algorithm," *Computer Graphics*, vol. 21, no. 4, pp. 163–169, 1987.
- [22] T. Lewiner, H. Lopes, A. W. Vieira, and G. Tavares, "Efficient implementation of marching cubes' cases with topological guarantees," *Journal of Graphics Tools*, vol. 8, no. 2, pp. 1–15, 2003.
- [23] O.-P. Jacquotte, "Grid optimization methods for quality improvement and adaptation," in *Handbook of Grid Generation*, J. F. Thompson, B. K. Soni, and N. P. Weatherill, Eds., CRC Press, London, UK, 1st edition, 1999.
- [24] R. Bartels, J. Beatty, and B. Barsky, *An Introduction to Splines for Use in Computer Graphics and Geometric Modeling*, Morgan Kaufmann, San Francisco, Calif, USA, 1987.
- [25] Y. Saad, *Iterative Methods for Sparse Linear Systems*, SIAM, Philadelphia, Pa, USA, 2nd edition, 2003.
- [26] V. Y. Pan, "Solving a polynomial equation: some history and recent progress," *SIAM Review*, vol. 39, no. 2, pp. 187–220, 1997.
- [27] E. Anderson, Z. Bai, S. Bischof et al., *LAPACK Users' Guide*, SIAM, Philadelphia, Pa, USA, 3rd edition, 1999.
- [28] T. S. Newman and H. Yi, "A survey of the marching cubes algorithm," *Computers & Graphics*, vol. 30, no. 5, pp. 854–879, 2006.
- [29] T. F. Robinson, M. A. Geraci, E. H. Sonnenblick, and S. M. Factor, "Coiled perimysial fibers of papillary muscle in rat heart: morphology, distribution, and changes in configuration," *Circulation Research*, vol. 63, no. 3, pp. 577–592, 1988.
- [30] A. Subramanian, A. Krol, A. H. Poddar, R. L. Price, R. Swarnkar, and D. H. Feiglin, "Large volume reconstruction from laser scanning microscopy using micro-CT as a template for deformation compensation," in *Medical Imaging: Image Processing*, vol. 6512 of *Proceedings of SPIE*, San Diego, Calif, USA, February 2007.
- [31] J. D. Bayer, R. C. Blake, G. Plank, and A. Trayanova, "A novel rule-based algorithm for assigning myocardial fiber orientation to computational heart models," *Annals of Biomedical Engineering*, vol. 40, no. 10, pp. 2243–2254, 2012.
- [32] T. F. Cootes, C. J. Taylor, D. H. Cooper, and J. Graham, "Active shape models—their training and application," *Computer Vision and Image Understanding*, vol. 61, no. 1, pp. 38–59, 1995.
- [33] A. F. Frangi, D. Rueckert, J. A. Schnabel, and W. J. Niessen, "Automatic construction of multiple-object three-dimensional statistical shape models: application to cardiac modeling," *IEEE Transactions on Medical Imaging*, vol. 21, no. 9, pp. 1151–1166, 2002.
- [34] Y. Zheng, A. Barbu, B. Georgescu, M. Scheuering, and D. Comaniciu, "Four-chamber heart modeling and automatic segmentation for 3-D cardiac CT volumes using marginal space learning and steerable features," *IEEE Transactions on Medical Imaging*, vol. 27, no. 11, pp. 1668–1681, 2008.
- [35] K. H. Huebner, D. L. Dewhurst, D. E. Smith, and T. G. Byrom, *The Finite Element Method for Engineers*, John Wiley & Sons, New York, NY, USA, 2001.

Research Article

The Relationship between the 24 h Blood Pressure Variability and Carotid Intima-Media Thickness: A Compared Study

Huahua Xiong,¹ Dan Wu,^{2,3} Xiaohong Tian,⁴ Wan-Hua Lin,^{2,3} Chunyue Li,^{2,3} Heye Zhang,^{2,3} Yunpeng Cai,^{2,3} and Yuan-Ting Zhang^{2,3,5}

¹ Department of Ultrasound, The Second Peoples' Hospital of Shenzhen, Shenzhen 518029, China

² Institute of Biomedical and Health Engineering, Shenzhen Institutes of Advanced Technology, Shenzhen 518055, China

³ Key Lab for Health Informatics, Chinese Academy of Sciences, Shenzhen 518055, China

⁴ Cardiac Electrocardiogram Room, The Second Peoples' Hospital of Shenzhen, Shenzhen 518029, China

⁵ Joint Research Center for Biomedical Engineering, The Chinese University of Hong Kong, Shatin, New Territories, Hong Kong

Correspondence should be addressed to Heye Zhang; hy.zhang@siat.ac.cn

Received 19 October 2013; Revised 17 December 2013; Accepted 24 December 2013; Published 11 February 2014

Academic Editor: Vicky Wang

Copyright © 2014 Huahua Xiong et al. This is an open access article distributed under the Creative Commons Attribution License, which permits unrestricted use, distribution, and reproduction in any medium, provided the original work is properly cited.

Large blood pressure variability (BPV) will not only harm the target organ but also increase the possibility of the cardiovascular events. Since the damage of vascular system always leads to the alteration of the carotid wall, the structure and function of the carotid artery have been extensively examined in previous studies. In this work we conduct a study (60 subjects, aged 33–79) to evaluate the relationship between BPV and carotid intima-media thickness (IMT) in Shenzhen, which is one large city in the southern area of China. In our study, the blood pressure (BP) was collected using the 24 h ambulatory BP monitoring, and the BPV was evaluated using standard deviation (SD), coefficient of variation (CV), and average real variability (ARV) during 24 h, daytime and nighttime. All the IMT measurements are collected by ultrasound. The results show that both the daytime, and 24 h systolic BPV evaluated by three indices are positively associated with IMT. Among them, daytime systolic BPV evaluated with ARV is the best variable to represent the increasing of carotid IMT. In addition, after adjusting by age, sex, smoking, hypertension, and mean BP and PP values, 24 h diastolic BPV evaluated with SD also presents the favorable performance.

1. Introduction

A large number of studies have suggested that hypertension can be the potential cause of cardiovascular disease (CVD) [1–3]. Therefore, the blood pressure (BP) level becomes one risk factor that has been frequently examined in the previous studies [4, 5]. Recently, blood pressure variability (BPV) has been proved to be promising in providing potential regulatory mechanisms of the cardiovascular system [6], and it can be simply classified as the short-term BPV and long-term BPV. Although the long-term BPV is strongly prognostic of cardiovascular morbidity and mortality [7], it is a very time-consuming process to collect the visit-to-visit BP measurements from the patients and calculate the BPV for each of them, and it may take more than several years to finish the whole study. However, for the short-term BPV analysis,

we could obtain the extensive information on BP profile and identify the patterns of circadian BP variation using the ambulatory blood pressure measurement (ABPM) [8]. Therefore, researchers are looking for the BPV analysis on ABPM; for example, from the analysis of ABPM, 24 h mean BP, different indices of BPV, and day-to-night BP changes can be obtained. Indeed, some studies have found that the BPV calculated from ABPM data could be a valuable predictor for progression of subclinical organ damage and also a risk factor for cardiovascular mortality in the Japanese population [9, 10]. Because of high economical development speed in China, the CVD and stroke are more often found in the southern area of China, which is traditionally considered as low endemic area. Hence, it is worthy to conduct a study to examine the prognostic significance of ABPM and its BPV over the population in the southern area of China.

In order to evaluate the effect of BPV on the carotid artery alteration or the damage progress of organ, one straightforward way is to examine the correlation between the BPV and the structure of vascular vessel [11, 12]. For the change of vascular structure, B-mode ultrasound is one widely applied tool to assess the carotid artery imaging and measure the carotid intima-media thickness (IMT). The increased IMT can be used as one predictor of the atherosclerosis and it is also a predictor for the cardiovascular events associated with the incident stroke [13, 14].

Accordingly, it will be one meaningful topic to examine the effects of different indices of BPV on the carotid artery alteration especially in the vascular structures over the population of the southern area in China. Stabouli et al. have reported that the carotid IMT was positively correlated to systolic ABPM value, but not the diastolic value [15]. It indicates that the systolic blood pressure (SBP) has a strong relation to the vascular lesions. In the study of García-García et al. [16], they found that systolic blood pressure variability (SBPV) had positive relationship with pulse wave velocity, and ambulatory arterial stiffness index in hypertensive patients. Zakopoulos et al. evaluated the time rate of BP and the extent of common carotid artery IMT in the normotensive and hypertensive subjects [17]. Although several studies have suggested that the increased BPV is associated with an increase in subsequent cardiovascular events, there are other studies where the cited association was not found [18, 19]. An explanation for these apparently contradictory results may be the selection of the index used for quantifying variability.

Thus, the aim of this study is to find out the possible relationship between the 24 h ambulatory BPV and carotid IMT over the population of the southern area in China. Furthermore, IMT has been well recognized as one predictive factor of CVD, and the change of BPV will definitely affect the structure and function of the carotid artery. Hence, it is worthy to evaluate the correlation between the carotid IMT and the BPV and compare the prognostic significance of different indices of BPV.

2. Methods

2.1. Study Design and Population. The study was conducted in the Second Peoples' Hospital of Shenzhen, Guangdong Province, China. 60 individuals aged 33–79 years (53.3% male gender) were enrolled in this study. They fulfilled the following inclusion criteria: (1) no history or clinical evidence of diabetes mellitus (fasting serum glucose <7.0 mmol/L; nonfasting serum glucose <11.1 mmol/L); (2) both 24 h BP monitoring and carotid artery ultrasound measurement were performed; (3) the valid BP measurements within 24 h $\geq 90\%$. This study was approved by the Institutional Ethics Committee of the Second Peoples' Hospital of Shenzhen (China), and the informed consent was obtained from every subject.

2.2. Ambulatory Blood Pressure Measurement. All of the subjects underwent 24 h ABPM on a day of daily activity. A proper cuff was selected according to the size of subject's arm and placed on the nondominant arm. The subjects were asked to keep their arms still at the time of measurements.

The ambulatory BP was recorded automatically using a commercial device (Mobil Graph 24 h ABP-Control). The daytime BP monitoring was from 7:00 to 22:59, measured automatically every 30 minutes, and during the nighttime, from 23:00 to 6:59, the BP was measured once an hour.

According to the recorded 24 h BP measurements, BPV was evaluated through the standard deviation (SD), coefficient of variation (CV), and average real variability (ARV) of the SBP and diastolic BP (DBP) during daytime, nighttime, and over 24 hours. For the short-term (with 24 h) BPV analysis, SD, CV, and ARV are the common indices of BPV in time domain. SD is calculated by the following formula

$$SD = \sqrt{\frac{1}{N-1} \sum_{k=1}^{k=N} (BP_k - BP_{\text{mean}})^2}, \quad (1)$$

where N is the number of valid BP measurements. The average SD of BP can also be divided by the corresponding mean BP and multiplied by 100 to express a normalized measure of BPV as a CV; the formula is as follows

$$CV = \frac{SD}{\text{mean}} \times 100\%. \quad (2)$$

ARV showed the average of the absolute differences between consecutive BP measurements, which was calculated as follows:

$$ARV = \frac{1}{N-1} \sum_{k=1}^{N-1} |BP_{k+1} - BP_k|, \quad (3)$$

where N is also the number of valid BP measurements.

2.3. Carotid Artery Ultrasound Examination. The carotid artery ultrasound was examined using a high-resolution ultrasound Doppler system (iU22, Philips Ultrasound, Bothell, WA, USA), with a 7.5 MHz liner array transducer. During the examination, the subjects were supine in the bed, with the head turned 45° away from the examined side. The left and right common carotid arteries, carotid bulbs, and internal carotid arteries were scanned in three angles (lateral, anterior, and posterior). Thus, we can assess the mean IMT in each position from the three measurements in different angles. The specific places we measured in the carotid artery were defined as follows: the IMT at the common carotid artery was measured on the far wall of blood vessel, 10–20 mm proximal to the carotid bifurcation. The carotid bulb we measured was in the carotid bifurcation, and the IMT at the internal carotid artery was measured over a distance of 10–20 mm from the bifurcation. In our study, the correlation analysis will focus on the common carotid artery, and thus carotid IMT in this paper represents the IMT at the common carotid artery, which is an average of right and left IMT. Besides, the abnormal IMT is defined that the IMT at the common carotid artery is more than 1.0 mm.

2.4. Statistical Analysis. The correlation between the BPV and the IMT was analyzed using a two-tailed Pearson's test. When the correlation coefficient r was close to 1, it indicated that

TABLE 1: Clinical characteristics of all the subjects and the two subgroups: normal IMT group and abnormal IMT group.

Characteristics	All subjects ($N = 60$)	IMT < 1.0 mm ($N = 26$)	IMT \geq 1.0 mm ($N = 34$)	P value
Age (years)	58.7 \pm 12.1	52.4 \pm 10.6	63.2 \pm 11.1	0.000**
Male gender (%)	53.3	38.5	64.7	0.273
Smoking (%)	23.3	11.5	32.4	0.573
IMT \geq 1.0 mm (%)	56.7	0	100	<0.001**
Presence of plaque (%)	46.7	19.2	67.6	<0.001**
Hypertensive patients (%)	76.7	69.2	82.4	0.196
CCA IMT (mm)	0.9 \pm 0.2	0.76 \pm 0.11	1.08 \pm 0.15	<0.001**
Bulb IMT (mm)	0.8 \pm 0.3	0.62 \pm 0.10	0.89 \pm 0.29	<0.001**
ICA IMT (mm)	0.6 \pm 0.1	0.54 \pm 0.08	0.64 \pm 0.10	<0.001**
24 h SBP (mmHg)	120.2 \pm 16.3	121.3 \pm 17.4	119.3 \pm 15.6	0.813
24 h DBP (mmHg)	76.6 \pm 12.9	78.4 \pm 14.4	75.2 \pm 11.6	0.148
24 h PP (mmHg)	43.6 \pm 9.2	42.8 \pm 7.6	44.1 \pm 10.4	0.142
Daytime SBP (mmHg)	121.2 \pm 16.0	122.1 \pm 17.0	120.4 \pm 15.4	0.763
Daytime DBP (mmHg)	77.5 \pm 12.8	79.2 \pm 14.2	76.2 \pm 11.7	0.131
Daytime PP (mmHg)	43.7 \pm 9.1	43.0 \pm 7.8	44.2 \pm 10.1	0.125
Nighttime SBP (mmHg)	116.7 \pm 18.7	118.6 \pm 19.2	115.2 \pm 18.4	0.860
Nighttime DBP (mmHg)	73.5 \pm 13.6	76.1 \pm 15.1	71.5 \pm 12.2	0.204
Nighttime PP (mmHg)	43.2 \pm 10.4	42.4 \pm 8.0	43.8 \pm 11.9	0.234
SBP decrease (%)	3.6 \pm 6.8	3.5 \pm 5.5	3.8 \pm 7.8	0.838
DBP decrease (%)	5.0 \pm 6.9	4.5 \pm 5.0	5.3 \pm 8.1	0.723

IMT: intima-media thickness; CCA: common carotid artery; ICA: internal carotid artery; SBP: systolic blood pressure; DBP: diastolic blood pressure; PP: pulse pressure. **Correlation is significant at the 0.01 level.

the BPV had highly positive correlation with IMT. On the contrary, when r was close to -1 , the relativity about BPV and IMT was negative. P value < 0.05 was considered statistically significant. Furthermore, simple linear regression analysis was applied to detect the linear relationship between the BPV indices and IMT. Besides, multiple linear regression analysis was performed to estimate the relation between different indices of BPV and IMT. We defined the carotid IMT as the dependent factor and the BPV estimated with SD, CV, and ARV as the independent factors, respectively. Finally, we carried out a multiple linear regression analysis using the backward selection method to verify which BPV index was independent of the baseline characteristics, mean BP, and pulse pressure (PP) values. All of the analyses were performed using SPSS 15.0 statistical package (SPSS Inc., Chicago, Illinois, USA).

3. Results

Among all of the participants, we excluded the cases that had the incomplete or invalid measurements. Finally, a total of 60 patients aged 33–79 (male 53.3%) were successfully obtained in the study. Of those, 26 subjects had the normal carotid IMT, and 34 subjects had a carotid IMT more than 1.0 mm, which is defined as the abnormal IMT. Table 1 summarized the clinical characteristics of all the subjects and two subgroups: the subjects with the normal IMT and the subjects with the abnormal IMT. The data of clinical characteristics were expressed as means \pm SDs or percentages. In this table, mean SBP, DBP, and PP values in different

periods of time, BP decreasing percent from day to night, IMTs at different carotid arteries, the plaque, and smoking status were reported. No significant differences were documented between the normal IMT group and abnormal IMT group regarding the BP values. However, for the baseline characteristics, the subjects in the abnormal IMT group were significantly older than the subjects in the normal IMT group ($P < 0.001$). Besides, in the abnormal IMT group, 67.6% of subjects had the plaques, which is higher than that in the normal IMT group ($P < 0.001$). Moreover, the abnormal IMT group had a significantly greater IMT both at bulb and internal carotid artery than the normal IMT group ($P < 0.001$), and most of them tended to suffer from the prevalence of the atherosclerotic plaques ($P < 0.001$).

We evaluated the BPV using SD, CV, and ARV, and the average BPV values quantified with three indices in 24 h were reported in Table 2. We compared the correlations of these BPV values in each group of the two using Pearson's test. No significant differences were found among the three indices of BPV; they had strongly positive correlation ($P < 0.01$). Moreover, we found that all of the SBPV values were greater than those of DBPV when evaluated using SD and ARV. In contrast, the DBPV values were found to be greater than SBPV when using CV as a measure.

Table 3 depicted the correlation coefficients between different indices of BPV and carotid IMT in all subjects. As the results showed, for all the subjects, the SD, CV, and ARV of daytime SBP showed a positive correlation with IMT ($r = 0.408$, $P = 0.001$; $r = 0.381$, $P = 0.003$; $r = 0.396$, $P = 0.002$, resp.). Similarly, all of the indices of 24 h SBPV were

TABLE 2: The blood pressure variabilities evaluated with SD, CV, and ARV in all of the subjects ($N = 60$).

Variables	SD (mmHg)		CV (%)		ARV (mmHg)	
	Mean \pm SD	r (P) ¹	Mean \pm SD	r (P) ²	Mean \pm SD	r (P) ³
Daytime SBPV	11.5 \pm 3.7	0.879 (<0.001)	9.6 \pm 2.7	0.717 (<0.001)	9.5 \pm 3.1	0.819 (<0.001)
Daytime DBPV	9.0 \pm 2.3	0.458 (<0.001)	13.6 \pm 4.6	0.439 (<0.001)	8.0 \pm 2.2	0.660 (<0.001)
Nighttime SBPV	9.8 \pm 3.7	0.765 (<0.001)	9.2 \pm 3.5	0.643 (<0.001)	10.0 \pm 4.1	0.805 (<0.001)
Nighttime DBPV	8.4 \pm 2.8	0.526 (<0.001)	13.9 \pm 5.4	0.383 (0.002)	9.3 \pm 3.1	0.734 (<0.001)
24 h SBPV	11.7 \pm 3.5	0.889 (<0.001)	9.9 \pm 2.8	0.773 (0.001)	9.5 \pm 2.9	0.880 (<0.001)
24 h DBPV	9.2 \pm 2.0	0.449 (<0.001)	14.0 \pm 4.5	0.390 (0.002)	8.3 \pm 2.0	0.675 (<0.001)

SD: standard deviation; CV: coefficient of variation; ARV: average real variability; SBPV: systolic blood pressure variability; DBPV: diastolic blood pressure variability. ¹The correlation between the BPV evaluated with SD and CV; ²the correlation between the BPV evaluated with CV and ARV; ³the correlation between the BPV evaluated with SD and ARV.

TABLE 3: The correlation between the blood pressure variability (evaluated with SD, CV, and ARV) and carotid intima-media thickness in all the subjects.

Variables	SD		CV		ARV	
	r	P value	r	P value	r	P value
Daytime SBPV	0.408	0.001**	0.381	0.003**	0.396	0.002**
Daytime DBPV	0.293	0.023*	0.302	0.019*	0.177	0.177
Nighttime SBPV	0.087	0.508	0.192	0.142	0.075	0.567
Nighttime DBPV	0.159	0.226	0.234	0.072	0.123	0.351
24 h SBPV	0.399	0.002**	0.376	0.003**	0.339	0.008**
24 h DBPV	0.328	0.010**	0.323	0.012*	0.214	0.101

Abbreviations as in Table 2. *Correlation is significant at the 0.05 level. **Correlation is significant at the 0.01 level.

significantly associated with the IMT ($r = 0.399$, $P = 0.002$; $r = 0.376$, $P = 0.003$; $r = 0.339$, $P = 0.008$, resp.). Conversely, there is no significant correlation between the nighttime BPV and carotid IMT. In addition, for the daytime DBPV and 24 h DBPV, both SD and CV indices were significantly related to IMT (for daytime DBPV, $r = 0.293$, $P = 0.023$; $r = 0.302$, $P = 0.019$, resp.; for 24 h DBPV, $r = 0.328$, $P = 0.010$; $r = 0.323$, $P = 0.012$, resp.), which differed from those evaluated with ARV. To further compare the results, we described these correlations in Figure 1. As Figure 1 showed, the SBPV during daytime and 24 h had greater correlation than DBPV during daytime and 24 h. Moreover, the correlations of the SBPV (evaluated with SD, CV, and ARV) and IMT were almost the same. However, for the DBPV during the daytime and 24 h, the SD and CV indices of BPV had greater correlation with IMT than ARV index.

The correlations between the average BP values and carotid IMT/number of plaques were analyzed using Pearson's test. The results were shown in Table 4. It indicated that there was no significant correlation between these BP variables and carotid IMT, whereas, 24 h PP, daytime PP, and nighttime PP are positively associated with the number of plaques ($r = 0.349$, $P = 0.006$; $r = 0.332$, $P = 0.01$; $r = 0.370$, $P = 0.004$, resp.). Moreover, a negative correlation was found between the nighttime average DBP and the number of plaques ($r = -0.254$, $P = 0.05$).

Before evaluating the effects of different indices of BPV on the carotid IMT, a simple linear regression analysis was performed for each BPV index. 24 h SBPV (SD), 24 h DBPV (CV), and daytime SBPV (ARV) presented the highly linear correlations with carotid IMT, which were shown in Figure 2.

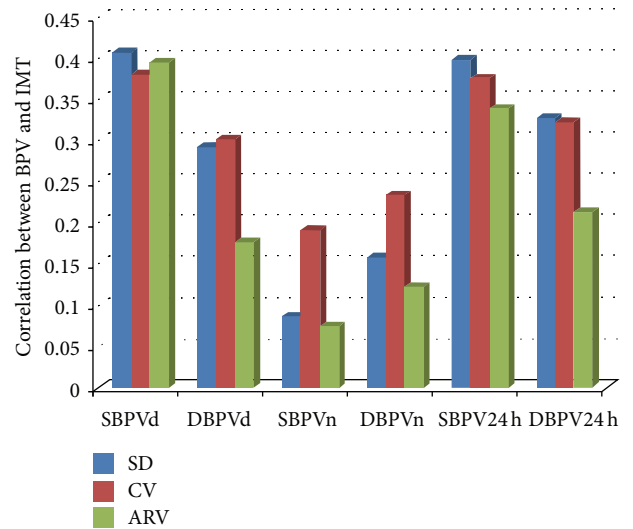


FIGURE 1: The correlation of the blood pressure variability and carotid intima-media thickness in all subjects. BPV, blood pressure variability; IMT, intima-media thickness; CV, coefficient of variation; ARV, average real variability; SBPV, systolic blood pressure variability; DBPV, diastolic blood pressure variability; SBPVd, daytime SBPV; DBPVd, daytime DBPV; SBPVn, nighttime SBPV; DBPVn, nighttime DBPV; SBPV24 h, 24 h SBPV; DBPV24 h, 24 h DBPV.

To further compare the effects of different indices of BPV on IMT, multiple linear regression analyses were performed using the backward selection method for different models in Table 5. P value of 0.1 or less was the criterion for

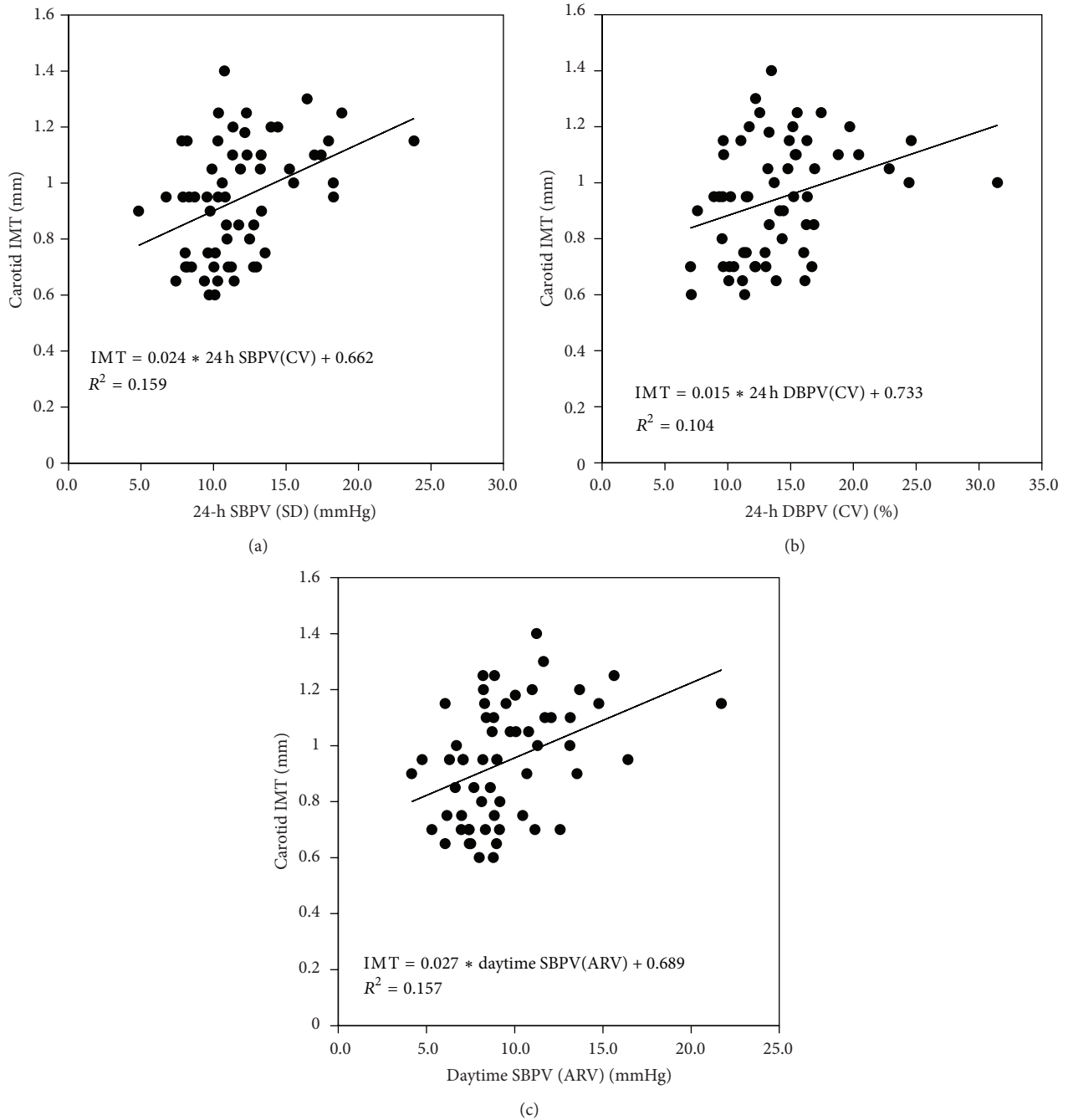


FIGURE 2: Linear correlation between common carotid artery intima-media thickness (IMT) and 24 h systolic blood pressure variability (SBPV) (SD), 24 h diastolic blood pressure variability (DBPV) (CV) and daytime systolic blood pressure variability (SBPV) (ARV).

a variable to remain in the model, and P value less than 0.05 was considered statistically significant. In the multiple regression models (model 1 to model 3), we set carotid IMT as dependent variable and daytime, nighttime, 24 h SBPV, and DBPV evaluated with different BPV indices as independent variables, respectively. The results showed that, for the SD index, 24 h SBPV was the only variable maintained in model 1 ($P = 0.002$, $R^2 = 0.159$). For the CV index, 24 h SBPV remained in model 2 ($P = 0.003$; $R^2 = 0.141$). For the ARV

index, daytime SBPV is the most associated with carotid IMT ($P = 0.002$, $R^2 = 0.157$). Afterward, these significant independent factors from model 1 to model 3 entered into the mixed model as the independent factors and carotid IMT also as the dependent variable. We found that daytime SBPV (ARV) was the only significant factor ($P = 0.002$) remaining in the mixed model. In addition, every BPV variable entered into the multiple linear regression models which are after adjusting for the baseline characteristics and corresponding

TABLE 4: The correlation between mean blood pressure values and carotid intima-media thickness/number of plaques in all the subjects.

Variables	IMT		Number of plaques	
	<i>r</i>	<i>P</i> value	<i>r</i>	<i>P</i> value
24 h SBP	0.017	0.895	0.005	0.972
24 h DBP	-0.099	0.451	-0.245	0.059
24 h PP	0.169	0.196	0.349	0.006**
Daytime SBP	0.016	0.904	-0.006	0.964
Daytime DBP	-0.099	0.454	-0.244	0.060
Daytime PP	0.171	0.191	0.332	0.010**
Nighttime SBP	0.006	0.963	0.016	0.901
Nighttime DBP	-0.105	0.423	-0.254	0.050*
Nighttime PP	0.157	0.231	0.370	0.004**
SBP decrease (%)	-0.031	0.816	-0.075	0.570
DBP decrease (%)	-0.007	0.959	0.051	0.700

Note: correlation coefficients (*r*) by Pearson's test are shown. The abbreviations as in Table 1.

*Correlation is significant at the 0.05 level (2-tailed). **Correlation is significant at the 0.01 level (2-tailed).

mean BP and PP values (please see Table 6, and the SBPV and DBPV values are displayed in bold fonts). We found that there were no obvious differences among three SBPV variables. However, the SD index of 24 h DBPV revealed better performance unexpectedly.

4. Discussion

The previous studies found that the short-term BPV had some effects on the carotid artery alteration (increased IMT and arteriosclerosis) and plaque formation [20–22]. However, the BPV within 24 h can be evaluated by different indices. It is unclear if the effects induced by different indices of BPV can be equal. In our present study, we have found that the SBP fluctuations during daytime and 24 h were significantly associated with the increased carotid IMT. Moreover, from the multiple linear regression models using different indices of BPV as the independent factors, we pointed out that daytime SBPV in ARV index had generally stronger relationship with IMT than SD or CV. It indicated that BPV evaluated with ARV was easier to reflect the effects on the carotid IMT. After adjusting by age, sex, smoking, hypertension, and corresponding mean BP and PP values, we found that the 24 h DBPV evaluated with SD presents the favorable performance in the regression model.

Our first finding corroborates the recently reported results of García-García et al. [16], who examined the relationship of 24 h BPV with vascular structure and function using SD and CV. In their study, both SD and CV of SBP during daytime had significant correlation with IMT ($r = 0.260$, $P < 0.001$; $r = 0.187$, $P < 0.001$); on the contrary, the significant correlations had not been found in DBPV and IMT. The similar conclusions were proposed from the European Lacidipine Study on Atherosclerosis (ELSA) [23]. They indicated that the IMT positively associated with not only

24 h, day, and night average SBP and PP but also the SD of 24 h SBP and PP. However, the relationships between DBPV and IMT were not referred in both of their studies. In our study, the results of correlation analysis were in agreement with their studies, mainly for the relationship between SBPV and IMT. Besides, a new finding in our study is that both daytime DBPV and 24 h DBPV evaluated with SD and CV are associated with IMT. These findings are consistent with some of the conclusions of Shintani et al. [24]. General Japanese population was analyzed in their Ohasama study, and they found that daytime and nighttime DBPV (SD) were both significantly related to the mean IMT ($r = 0.17$, $P < 0.0001$; $r = 0.15$, $P < 0.0001$, resp.). However, only daytime DBPV ($P = 0.015$) maintained the significant correlation with the mean IMT after adjustment for BP level and the 24 h DBPV analysis was not referred.

Besides, one major contribution of our study is to compare the effects on the carotid artery structure for different indices of BPV. Firstly, we found that no significant differences in means \pm SDs were documented among three indices of BPV. However, their correlations with IMT were mostly different, which was further demonstrated in the multiple linear regression analysis. Overall, these findings support the view that the prognostic importance of BPV will be affected by the indices of BPV [25]. Nowadays, most of the studies explored the prognostic significance of BPV for the cardiovascular events, but not the carotid artery alteration or arteriosclerosis. In the population-based study in Latin America [26], Mena et al. found that the commonly used SD index may be more sensitive to the sampling frequency of the ABPM devices, and ARV index ($RR = 1.611$, $P = 0.004$) is a more reliable representation of time series variability than SD ($RR = 1.103$, $P = 0.571$) for the prognostic significance of BPV. The similar conclusions have been shown in the study of Stolarz-Skrzypek et al. [27] and Hansen et al. [28]. In our present study, we not only found the most significant BPV variable to reflect the alteration of carotid IMT for each BPV index but also compared the effects of these BPV variables in the mixed model. Only daytime SBPV (ARV) remained after the backward selection regression. Moreover, the association remained significant even after adjusting for the baseline characteristics and the corresponding mean BP values. Besides, 24 h DBPV and daytime DBPV (SD and CV) were also correlated with the IMT and contributed to the multiple linear regression models after adjustment, which is the new finding of our present study. We speculated the reasons from the calculating formulae of different indices of BPV. SD can only reflect the fluctuation of the BP value. The CV allows the measurement of BPV and eliminates the measurement magnitude effect [16]. However, ARV can reflect the beat-to-beat variation, which is a reliable index for the time series variability [26], especially for the high-sampling BP measurements. However, SD and CV could better present the prognostic significance of DBPV than ARV.

Other findings of our study also deserve to be discussed. Firstly, daytime PP, nighttime PP, and 24 h PP are positively associated with the number of plaques but not with carotid IMT. Moreover, the nighttime average DBP had negative correlation with the number of plaques in the carotid artery. It

TABLE 5: Multiple linear regression analyses performed by backward regression.

Model	Independent factor	β	Lower 95% interval	Upper 95% interval	P value	R^2
Model 1 ^a (SD)	24 h SBPV	0.024	0.009	0.038	0.002	0.159
	Constant	0.662	0.486	0.838	0.000	
Model 2 ^b (CV)	24 h SBPV	0.028	0.010	0.045	0.003	0.141
	Constant	0.671	0.488	0.853	0.000	
Model 3 ^c (ARV)	Daytime SBPV	0.027	0.010	0.043	0.002	0.157
	Constant	0.689	0.527	0.851	0.000	
Model 4 ^d (Mix)	Daytime SBPV (ARV)	0.027	0.010	0.043	0.002	0.157
	Constant	0.689	0.527	0.851	0.000	

^aModel 1: using the SDs of blood pressure as the independent factors. ^bModel 2: using the coefficients of variation of blood pressure as the independent factors. ^cModel 3: using average real variabilities of blood pressure as the independent factors. ^dModel 4: backward regression using the significant independent factors from model 1 to model 3.

TABLE 6: Adjusted multiple regression analysis of carotid intima-media thickness and blood pressure variabilities*.

Factors	β (95% CI)	P value	R^2
Age ⁺	0.069 (0.033–0.105)	0.061	0.449
Smoking	0.150 (0.049–0.251)	0.004	
Hypertension	0.148 (0.047–0.249)	0.005	
24 h SBPV (SD)	0.016 (0.004–0.029)	0.012	
Age ⁺	0.066 (0.029–0.103)	0.001	0.402
Smoking	0.150 (0.048–0.251)	0.005	
Hypertension	0.166 (0.064–0.268)	0.011	
24 h SBPV (CV)	0.019 (0.004–0.035)	0.017	
Age ⁺	0.073 (0.036–0.109)	0.000	0.424
Smoking	0.136 (0.032–0.240)	0.012	
Hypertension	0.133 (0.027–0.238)	0.015	
Daytime SBPV (ARV)	0.015 (0.000–0.029)	0.050	
Age ⁺	0.081 (0.047–0.116)	0.000	0.440
Smoking	0.124 (0.020–0.228)	0.020	
Hypertension	0.136 (0.033–0.239)	0.011	
24 h DBPV (SD)	0.026 (0.004–0.048)	0.020	
Age ⁺	0.071 (0.034–0.107)	0.000	0.427
Smoking	0.150 (0.047–0.253)	0.005	
Hypertension	0.163 (0.060–0.267)	0.003	
24 h DBPV (CV)	0.010 (0.000–0.020)	0.042	

CI: confidence interval. * Adjusted by age, sex, smoking, hypertension, and mean BP values. ⁺ Per 10-year increase.

is consistent with the conclusions of Shintani et al.; nighttime BPV reflects the prevalence of carotid plaque more precisely than daytime BPV in general population [24]. We previously showed that the increased PP is of prognostic importance in the target-organ damage and plaque formation, especially for the cases with the high SBP in the daytime and low DBP in the nighttime. It can be speculated from the physiological mechanism. Oscillatory shear stress had a major effect on regulating the function of human endothelial cell and it stimulates mononuclear leukocyte adhesion and migration in the arterial wall, which is the initiation of the atherosclerotic lesions [29]. Thus, the increased BP variation is assumed to increase oscillatory shear stress in the walls of the carotid

artery. Moreover, the blood vessels are damaged by the oscillatory shear stress and it will finally lead to the carotid plaque formation [24].

Secondly, whether the BPV can be treated as one risk factor independent to the average BP level for arteriosclerosis or cardiovascular events are still not clear in previous studies. Mancina et al. have found that the end-organ damage was determined not only by the degree of the high BP level but also by the magnitude of the BPV occurring over the 24 h period [9, 11]. In addition, Kikuya et al. mentioned that BPV was an independent predictor for cardiovascular mortality in the general population [9]. However, Hansen et al. stated that BPV remained an elusive predictor of cardiovascular outcome, as it was strongly associated with the BP level [30]. In a recent published paper, Nagai et al. found that SD, CV, and delta (maximum-minimum) in visit-to-visit SBP were associated with the max-IMT for the high-risk elderly, whereas only delta SBP had significant correlation with max-IMT independently of average SBP [31]. In our multiple linear regression analysis, it has been demonstrated that all of the BPV variables were not independent of the mean BP and PP values for evaluating the increased carotid IMT but independent of the well-known confounding factors, such as age, smoking, and hypertension. Despite all this, more evidence is still required to assess whether the BPV is an independent predictor of arteriosclerosis or cardiovascular events.

Finally, certain limitations of our study should be briefly discussed. First, the relatively small size of the subjects is the main limitation in our present preliminary study. Although the statistically significant results were obtained in our study and the results can be explained by the physiological mechanism, the number of subjects could be still too small to extrapolate the study findings to general population in the southern area of China. The second limitation is the precision of calculating BPV during nighttime. We set the sampling frequency of ABPM according to the BP monitoring protocol constituted by the Cardiac Electrocardiogram Room, the Second Peoples' Hospital of Shenzhen. Although one-hour interval sampling during nighttime may not disturb the sleeping of patients, it is really an exceedingly low sampling frequency. Once one or more measurements are invalid or lost, the calculated results of BPV will be affected to some extent. Lastly, in our present study, the independent factors are limited

to the baseline characteristics (age, sex, hypertension, and smoking status), average BP values, and BPV variables. It may lose some significant variables which can contribute to the carotid artery alteration. Meanwhile, the influences of confounding variables deserve to be discussed, although we utilized the backward regression to reduce the influence of the confounding variables.

In conclusion, though the number of samples in this compared study was limited, we also obtained the suggestive conclusions on the relationship between ambulatory BPV and carotid IMT. Our findings extended the validation of the correlation of ambulatory BPV and carotid artery alterations from western population study to the population in the southern area of China.

5. Conclusions

In this study, we provide the evidence that, for the subjects from the southern area of China, all of the indices of SBPV for daytime and 24 h had significant correlation with IMT. Among them, daytime SBPV evaluated with ARV can be the best variable to explain the increase of carotid IMT in linear regression model. In addition, daytime DBPV and 24 h DBPV (SD and CV) are also found to be related to the increased IMT. We consider that ARV is a better representation of BPV than SD and CV for the prognostic significance of carotid artery alteration. However, a longitudinal study is needed to verify the prognostic value of different indices of BPV for the cardiovascular events. In the future, we will conduct the large-scale trials and perform multivariate analysis to investigate how to predict the risks of CVD and mortality from the alteration of carotid structure and function.

Conflict of Interests

The authors declare that there is no conflict of interests regarding the publication of this paper.

Authors' Contribution

Huahua Xiong and Dan Wu contributed equally to this work.

Acknowledgments

This work was supported in part by the National Basic Research Program 973 (no. 2010CB732606), the Guangdong Innovation Research Team Fund for Low-cost Health-care Technologies in China, the External Cooperation Program of the Chinese Academy of Sciences (no. GJHZ1212), the Key Lab for Health Informatics of the Chinese Academy of Sciences, the Peacock Program to Attract Overseas High-Caliber Talents to Shenzhen, the National Natural Science Foundation of China (no. 81101120, no. 61002002, and no. 61233012).

References

- [1] W. B. Kannel, "Elevated systolic blood pressure as a cardiovascular risk factor," *The American Journal of Cardiology*, vol. 85, no. 2, pp. 251–255, 2000.
- [2] B. M. Psaty, C. D. Furberg, L. H. Kuller et al., "Isolated systolic hypertension and subclinical cardiovascular disease in the elderly: initial findings from the cardiovascular health study," *Journal of the American Medical Association*, vol. 268, no. 10, pp. 1287–1291, 1992.
- [3] J. Stamler, R. Stamler, and J. D. Neaton, "Blood pressure, systolic and diastolic, and cardiovascular risks: US population data," *Archives of Internal Medicine*, vol. 153, no. 5, pp. 598–615, 1993.
- [4] P. Verdecchia, G. Schillaci, G. Reboldi, S. S. Franklin, and C. Porcellati, "Different prognostic impact of 24-hour mean blood pressure and pulse pressure on stroke and coronary artery disease in essential hypertension," *Circulation*, vol. 103, no. 21, pp. 2579–2584, 2001.
- [5] M. Kikuya, T. Ohkubo, K. Asayama et al., "Ambulatory blood pressure and 10-year risk of cardiovascular and noncardiovascular mortality: the Ohasama study," *Hypertension*, vol. 45, no. 2, pp. 240–245, 2005.
- [6] G. Mancia and G. Grassi, "Mechanisms and clinical implications of blood pressure variability," *Journal of Cardiovascular Pharmacology*, vol. 35, supplement 4, pp. S15–S19, 2000.
- [7] P. M. Rothwell, S. C. Howard, E. Dolan et al., "Prognostic significance of visit-to-visit variability, maximum systolic blood pressure, and episodic hypertension," *The Lancet*, vol. 375, no. 9718, pp. 895–905, 2010.
- [8] G. Parati, J. E. Ochoa, C. Lombardi, and G. Bilo, "Assessment and management of blood-pressure variability," *Nature Reviews Cardiology*, vol. 10, no. 3, pp. 143–155, 2013.
- [9] M. Kikuya, A. Hozawa, T. Ohokubo et al., "Prognostic significance of blood pressure and heart rate variabilities: the Ohasama Study," *Hypertension*, vol. 36, no. 5, pp. 901–906, 2000.
- [10] K. Eguchi, S. Hoshida, J. E. Schwartz, K. Shimada, and K. Kario, "Visit-to-visit and ambulatory blood pressure variability as predictors of incident cardiovascular events in patients with hypertension," *The American Journal of Hypertension*, vol. 25, no. 9, pp. 962–968, 2012.
- [11] R. Sega, G. Corrao, M. Bombelli et al., "Blood pressure variability and organ damage in a general population: results from the PAMELA study," *Hypertension*, vol. 39, no. 2, part 2, pp. 710–714, 2002.
- [12] D. F. Su and C. Y. Miao, "Blood pressure variability and organ damage," *Clinical and Experimental Pharmacology and Physiology*, vol. 28, no. 9, pp. 709–715, 2001.
- [13] J. F. Polak, M. J. Pencina, D. H. O'Leary, and R. B. D'Agostino, "Common carotid artery intima-media thickness progression as a predictor of stroke in multi-ethnic study of atherosclerosis," *Stroke*, vol. 42, no. 11, pp. 3017–3021, 2011.
- [14] D. Baldassarre, A. Hamsten, F. Veglia et al., "Measurements of carotid intima-media thickness and of interadventitia common carotid diameter improve prediction of cardiovascular events: results of the IMPROVE (Carotid Intima Media Thickness [IMT] and IMT-progression as predictors of vascular events in a high risk european population) study," *Journal of the American College of Cardiology*, vol. 60, no. 16, pp. 1489–1499, 2012.
- [15] S. Stabouli, V. Kotsis, C. Karagianni, N. Zakopoulos, and A. Konstantopoulos, "Blood pressure and carotid artery intima-media thickness in children and adolescents: the role of obesity," *Hellenic Journal of Cardiology*, vol. 53, no. 1, pp. 41–47, 2012.
- [16] Á. García-García, L. García-Ortiz, J. I. Recio-Rodríguez et al., "Relationship of 24-h blood pressure variability with vascular structure and function in hypertensive patients," *Blood Pressure Monitoring*, vol. 18, no. 2, pp. 101–106, 2013.

- [17] N. A. Zakopoulos, G. Tsivgoulis, G. Barlas et al., "Time rate of blood pressure variation is associated with increased common carotid artery intima-media thickness," *Hypertension*, vol. 45, no. 4, pp. 505–512, 2005.
- [18] G. Schillaci, P. Verdecchia, C. Borgioni, A. Ciucci, and C. Porcellati, "Lack of association between blood pressure variability and left ventricular mass in essential hypertension," *The American Journal of Hypertension*, vol. 11, no. 5, pp. 515–522, 1998.
- [19] S. D. Mouloupoulos, S. F. Stamatelopoulos, N. A. Zakopoulos et al., "Effect of 24-hour blood pressure and heart rate variations on left ventricular hypertrophy and dilatation in essential hypertension," *The American Heart Journal*, vol. 119, no. 5, pp. 1147–1152, 1990.
- [20] G. Schillaci, G. Bilo, G. Pucci et al., "Relationship between short-term blood pressure variability and large-artery stiffness in human hypertension findings from 2 large databases," *Hypertension*, vol. 60, no. 2, pp. 369–377, 2012.
- [21] D. Sander, C. Kukla, J. Klingelhöfer, K. Winbeck, and B. Conrad, "Relationship between circadian blood pressure patterns and progression of early carotid atherosclerosis: a 3-year follow-up study," *Circulation*, vol. 102, no. 13, pp. 1536–1541, 2000.
- [22] T.-C. Su, Y.-T. Lee, S. Chou, W.-T. Hwang, C.-F. Chen, and J.-D. Wang, "Twenty-four-hour ambulatory blood pressure and duration of hypertension as major determinants for intima-media thickness and atherosclerosis of carotid arteries," *Atherosclerosis*, vol. 184, no. 1, pp. 151–156, 2006.
- [23] G. Mancia, G. Parati, M. Hennig et al., "Relation between blood pressure variability and carotid artery damage in hypertension: Baseline data from the European Lacidipine Study on Atherosclerosis (ELSA)," *Journal of Hypertension*, vol. 19, no. 11, pp. 1981–1989, 2001.
- [24] Y. Shintani, M. Kikuya, A. Hara et al., "Ambulatory blood pressure, blood pressure variability and the prevalence of carotid artery alteration: the Ohasama study," *Journal of Hypertension*, vol. 25, no. 8, pp. 1704–1710, 2007.
- [25] G. Parati, J. E. Ochoa, P. Salvi, C. Lombardi, and G. Bilo, "Prognostic value of blood pressure variability and average blood pressure levels in patients with hypertension and diabetes," *Diabetes Care*, vol. 36, supplement 2, pp. S312–S324, 2013.
- [26] L. Mena, S. Pintos, N. V. Queipo, J. A. Aizpúrua, G. Maestre, and T. Sulbarán, "A reliable index for the prognostic significance of blood pressure variability," *Journal of Hypertension*, vol. 23, no. 3, pp. 505–511, 2005.
- [27] K. Stolarz-Skrzypek, L. Thijs, T. Richart et al., "Blood pressure variability in relation to outcome in the international database of ambulatory blood pressure in relation to cardiovascular outcome," *Hypertension Research*, vol. 33, no. 8, pp. 757–766, 2010.
- [28] T. W. Hansen, L. Thijs, Y. Li et al., "Prognostic value of reading-to-reading blood pressure variability over 24 hours in 8938 subjects from 11 populations," *Hypertension*, vol. 55, no. 4, pp. 1049–1057, 2010.
- [29] D. C. Chappell, S. E. Varner, R. M. Nerem, R. M. Medford, and R. W. Alexander, "Oscillatory shear stress stimulates adhesion molecule expression in cultured human endothelium," *Circulation Research*, vol. 82, no. 5, pp. 532–539, 1998.
- [30] T. W. Hansen, Y. Li, and J. A. Staessen, "Blood pressure variability remains an elusive predictor of cardiovascular outcome," *The American Journal of Hypertension*, vol. 22, no. 1, pp. 3–4, 2009.
- [31] M. Nagai, S. Hoshida, J. Ishikawa, K. Shimada, and K. Kario, "Visit-to-visit blood pressure variations: new independent determinants for cognitive function in the elderly at high risk of cardiovascular disease," *Journal of Hypertension*, vol. 30, no. 8, pp. 1556–1563, 2012.

Research Article

Embryonic Heart Morphogenesis from Confocal Microscopy Imaging and Automatic Segmentation

Hongda Mao,¹ Megan Gribble,² Arkady M. Pertsov,² and Pengcheng Shi¹

¹ *Computational Biomedicine Laboratory, Rochester Institute of Technology, Rochester, NY 14623, USA*

² *Department of Pharmacology, SUNY Upstate Medical University, Syracuse, NY 13210, USA*

Correspondence should be addressed to Hongda Mao; hongda.mao@mail.rit.edu

Received 10 October 2013; Accepted 14 November 2013

Academic Editor: Heye Zhang

Copyright © 2013 Hongda Mao et al. This is an open access article distributed under the Creative Commons Attribution License, which permits unrestricted use, distribution, and reproduction in any medium, provided the original work is properly cited.

Embryonic heart morphogenesis (EHM) is a complex and dynamic process where the heart transforms from a single tube into a four-chambered pump. This process is of great biological and clinical interest but is still poorly understood for two main reasons. On the one hand, the existing imaging modalities for investigating EHM suffered from either limited penetration depth or limited spatial resolution. On the other hand, current works typically adopted manual segmentation, which was tedious, subjective, and time consuming considering the complexity of developing heart geometry and the large size of images. In this paper, we propose to utilize confocal microscopy imaging with tissue optical immersion clearing technique to image the heart at different stages of development for EHM study. The imaging method is able to produce high spatial resolution images and achieve large penetration depth at the same time. Furthermore, we propose a novel convex active contour model for automatic image segmentation. The model has the ability to deal with intensity fall-off in depth which is characterized by confocal microscopy images. We acquired the images of embryonic quail hearts from day 6 to day 14 of incubation for EHM study. The experimental results were promising and provided us with an insight view of early heart growth pattern and also paved the road for data-driven heart growth modeling.

1. Introduction

The heart is the first functioning organ in the embryo. Although the morphology of the heart changes dramatically during development where it transforms from a single tube into a four-chambered pump, the heart functions without interruption to serve the metabolic needs of the rapidly growing embryo [1]. Embryonic heart morphogenesis (EHM) is critically important for long-time survival, and any defects in the developmental mechanism during embryogenesis may result in congenital cardiac anomalies. In fact, congenital heart disease is relatively frequent which affects from 19 to 75 per 1000 births worldwide and has been an important cause of childhood morbidity and mortality [2]. Understanding EHM in normal and malformed hearts, therefore, has been of considerable clinical and biological interest.

Despite a large body of research in the last decades [3–8], EHM is still poorly understood mainly because of the complexity of the growing geometry and extremely small size of the developing heart. Thanks to the rapid development

of imaging techniques, 3D reconstruction of embryonic hearts from biomedical images has dramatically improved our ability to visualize EHM. Several imaging modalities have been proposed for the study of EHM; however, each of them has its own limitations. Histological sectioning was one of the most widely used approaches for rendering 3D structure of the developing heart [6]. Nevertheless, it needed sophisticated manual alignment of all the sections which was difficult and labor-intensive and therefore left it only for lab researchers. Optical scanning techniques were also used for rendering 3D/4D volumes of embryonic hearts [7, 9], but low penetration depth limits their application in imaging late stages of embryonic heart development [8]. There were also other imaging modalities used for understanding EHM which, unfortunately, provided very limited spatial resolution [10]. Recently, micro-CT technique was used to image the chambers of embryonic hearts [8]. However, the sophisticated polymerization process ignored the structure of the peripheral luminal space which is actually very important for EHM understanding. Last but not least,

all the aforementioned works adopted manual segmentation for 3D heart segmentation due to the lack of appropriate automatic segmentation approaches. Nevertheless, manual segmentation is tedious, subjective, and time consuming considering the complexity of the developing heart and high resolution images. Thus, an automatic image segmentation method is badly needed.

In view of the problems, we propose a new imaging approach for studying EHM, utilizing tissue optical immersion clearing and 3D confocal microscopy imaging, which can produce high spatial resolution images and achieve large penetration depth at the same time. Furthermore, considering the intensity fall-off in depth nature of confocal microscopy images, we propose a convex active contour model with image depth information for automatic image segmentation. A recently proposed Split Bregman method was used to minimize the objective function of the model [11, 12]. Embryonic quail hearts at different stages of development were scanned and segmented. Initial heart growth pattern was found through comparison of the structure of hearts at different stages of development. We also quantified the volume change of the whole heart and luminal space from day 6 to day 14 of incubation to provide an insight view of embryonic heart development. Furthermore, realistic continuous growth modeling of the living organs from data sparsely distributed in time has been an emerging field in biomedical field [13, 14], with potential applications to the analysis and prediction of evolving pathologic structures. Thus, this work can be also considered as the first step for data-driven heart growth modeling.

2. Methodology

The human heart becomes a four-chambered organ by approximately week 8, which is almost the same time the embryo can be visualized through ultrasound, a point that is too late to visualize EHM [15]. We chose quail embryos as our model to study EHM because of their rapid development and short embryonic gestation period (a hatch time of 16.5 days of incubation). Except for the time scale, the development of the quail heart parallels that of the human heart.

2.1. Image Acquisition. Optical imaging method has been widely used as a tool for clinical functional imaging owing to its unique informative features, simplicity, safety, and low cost compared to conventional X-ray, MRI, and ultrasound imaging. However, the main limitations of optical imaging techniques, including confocal microscopy, are low contrast and spatial resolution, as well as a small probing depth due to strong light scattering in tissue layers [16]. To utilize its strengths and overcome its weaknesses, we combined confocal microscopy imaging with tissue optical immersion clearing. Optical clearing technique has been used in many areas [16]. However, to the best of our knowledge, this is the first time to use optical clearing with confocal microscopy imaging for EHM study.

In this paper, all the experiments conformed to the *Guide for the Care and Use of Laboratory Animals* (NIH publication

no. 85-23, revised 1996). Embryonic hearts were obtained after incubation of *Coturnix japonica* (GQF Manufacturing Co., Savannah, GA) or Japanese quail eggs to different stages of development. The hearts were stained with di-4-ANBDQBS which was voltage sensitive fluorescent dyes and then were dehydrated by a graded ethanol series. After dehydration, the hearts were cleared using a 1:2 benzyl alcohol to benzyl benzoate mixture. The cleared heart, which appeared virtually transparent, was stored in the clearing solution until imaging. For image acquisition, the cleared hearts were mounted in a special cuvette and scanned by a Zeiss LSM 510 confocal microscope, with its numerical aperture being equal to 0.5 and the radius of back-projected pinhole equal to 2.53 nm. The dye was excited at wavelength of 543 nm and fluorescence recorded the wave length above 560 nm using a long-pass filter. For more details of heart preparation and imaging, we refer the readers to [17].

High spatial resolution images were obtained after heart scanning, which had an intraslice pixel size of $1.75 \mu\text{m} \times 1.75 \mu\text{m}$ and interslice pixel size $12.9000 \mu\text{m}$. In Figure 1, we present 3D view of three hearts at days 6, 8, and 14, respectively. From the images, the evolution of the luminal space of the heart from spongy structure to well-separated chamber structure can be clearly observed.

2.2. Image Formation. In a confocal microscope, a pinhole is used to reject most out-of-focus light. Thus, the amount of light reaching the detector is low, and the noise statistics can be well described by a Poisson process [18]. A general image formation model can be represented as the following equation:

$$I_0(x) = n([h * I](x)), \quad (1)$$

where $x \in \Omega$ is a point in the image domain. I_0 is an observed image. I is an ideal image. h is a point spread function (PSH). $*$ means convolution operation. n models the noise distribution. Based on our imaging setting, the PSF of the microscope is very small compared to our voxel size, and therefore the effect of convolution by PSF can be ignored. In the work, we used median filter to smooth the observed image and assume the noise in the smoothed image can be considered as additive zero mean Gaussian distribution. Thus the final image formation can be represented as the following equation:

$$\tilde{I}_0 \approx I + \mathbf{n}, \quad (2)$$

where \tilde{I}_0 and \mathbf{n} represent smoothed image and image noise, respectively.

2.3. Image Segmentation. The purpose of image segmentation is to find a partition $\psi(\Omega)$ of the image domain Ω and recover the ideal image I as well. Under the assumption that the intensity distribution of the ideal image is piecewise constant, Chan-Vese (CV) model with level set implementation was proposed and has been widely used for image segmentation [19]. Later on, this model was further extended to global CV (G-CV) model by transforming it into a global convex

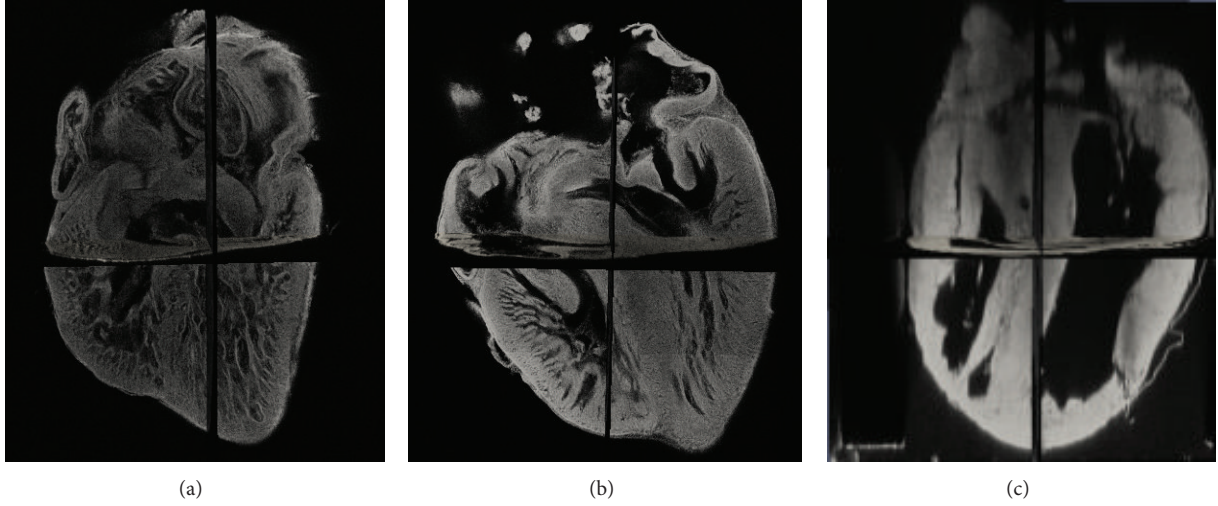


FIGURE 1: 3D view of embryonic quail hearts. From left to right: day 6, day 8, and day 14.

optimization problem [20]. However, confocal microscopy images are characterized by intensity fall-off in depth, which makes G-CV model unsuitable for this purpose. To solve this problem, we further assume the ideal image can be described as the multiplication of an intensity piecewise constant image c and a depth-related bias field b

$$I = \sum_{i=1}^N (c_i \cdot u_i) \cdot b_i, \quad (3)$$

where N is number of regions in the image and u_i is an image partition function. Under this assumption, we developed a new convex active contour model for automatic segmentation of confocal microscopy images. The model can be represented as the following equation:

$$\begin{aligned} \min_{u \in [0,1]} E(c_1, c_2, u) &= \int_{\Omega} |\nabla u(x)| dx \\ &+ \lambda \int_{\Omega} (\tilde{I}_0(x) - I_1(x))^2 u(x) dx \\ &+ \lambda \int_{\Omega} (\tilde{I}_0(x) - I_2(x))^2 (1 - u(x)) dx. \end{aligned} \quad (4)$$

The first term on the right side of (4) is a L1 total variation (TV) norm which is used for smoothing the variable u . The second and third terms are data fidelity terms which keep the intensity distribution of the ideal images close to the original image. Here, u is a partition variable and λ is a weighting constant to keep the balance among the three terms on the right side of (4). $I_1(x) = c_1 \cdot \gamma^{z(x)}$ and $I_2(x) = c_2 \cdot \gamma^{z(x)}$ are two ideal images that represent the intensity on two different subregions. $\gamma^{z(x)}$ is a depth-dependent bias field to characterize the intensity fall-off in depth property of the images, where z is the position of the point x in

z -direction and γ is an experimentally determined decreasing constant.

There are total three unknown variables in our model: c_1 , c_2 , and u . By using first variation with respect to c_1 and c_2 , we can obtain

$$\begin{aligned} c_1 &= \frac{\int_{x \in \Omega} u(x) \tilde{I}_0(x) \gamma^{z(x)} dx}{\int_{x \in \Omega} u(x) \gamma^{2z(x)} dx}, \\ c_2 &= \frac{\int_{x \in \Omega} (1 - u(x)) \tilde{I}_0(x) \gamma^{z(x)} dx}{\int_{x \in \Omega} (1 - u(x)) \gamma^{2z(x)} dx}. \end{aligned} \quad (5)$$

To minimize (4) with respect to u , we adopt the fast and efficient Split Bregman method proposed in [11, 12]. Split Bregman method does not require regularization, continuation, or the enforcement of inequality constraints, and it is very efficient for solving L1-regularized optimization problems like (4). For easier description of Split Bregman method, we rewrite the form of (4):

$$\min_{u \in [0,1]} E = \int_{\Omega} |\nabla u(x)| + \lambda e_r(x) u(x) dx, \quad (6)$$

where $e_r(x) = (\tilde{I}_0(x) - I_1(x))^2 - (\tilde{I}_0(x) - I_2(x))^2$. Here, the term $\lambda \int_{\Omega} (\tilde{I}_0(x) - I_2(x))^2 dx$ has been ignored because it does not include the variable u .

To minimize (6) with respect to u , we introduce an auxiliary variable d , such that $d = \nabla u$. Thus, the problem of minimizing the energy function of (6) becomes to minimize the following energy function:

$$\min_{u \in [0,1], d} \int_{\Omega} |d| + \lambda e_r(x) u(x) dx, \quad \text{with } d = \nabla u. \quad (7)$$

To solve the constrained problem in (7), we use Split Bregman method. The problem becomes to solve the following sequence of optimization problems:

$$(u^{k+1}, d^{k+1}) = \arg \min_{u \in [0,1], d} \int_{\Omega} |d| + \lambda e_r(x) u(x) + \frac{\mu}{2} |d - \nabla u - b^k|^2 dx, \quad (8)$$

$$b^{k+1} = b^k + \nabla u^{k+1} - d^{k+1}. \quad (9)$$

Here, $k = 0, 1, 2, \dots$, the third term on the right side of (8) is used to enforcing the constraint $d = \nabla u$. b^k is the Bregman vector. μ and λ are two constant weighting parameters to keep a balance of two terms. To solve (8), we adopt the alternating minimization scheme. First, we consider the minimization of (8) with respect to u . The minimizing solution u^{k+1} is characterized by the optimality condition

$$\lambda \nabla u = \lambda e_r + \mu \operatorname{div}(b^k - d^k), \quad u \in [0, 1]. \quad (10)$$

By using Gauss-Seidel iterative scheme, we can get an approximate solution for a 3D variable u^{k+1} . ($i = 0, 1, 2, \dots$):

$$\begin{aligned} \zeta_{l,m,n} &= d_{l-1,m,n}^{x,k} - d_{l,m,n}^{x,k} - b_{l-1,m,n}^{x,k} + b_{l,m,n}^{x,k} \\ &+ d_{l-1,m,n}^{y,k} - d_{l,m,n}^{y,k} - b_{l-1,m,n}^{y,k} + b_{l,m,n}^{y,k} \\ &+ d_{l-1,m,n}^{z,k} - d_{l,m,n}^{z,k} - b_{l-1,m,n}^{z,k} + b_{l,m,n}^{z,k}, \\ \phi_{l,m,n} &= \frac{1}{6} \left(u_{l-1,m,n}^{k+1,i} + u_{l+1,m,n}^{k+1,i} + u_{l,m-1,n}^{k+1,i} + u_{l,m+1,n}^{k+1,i} \right. \\ &\left. + u_{l,m,n-1}^{k+1,i} + u_{l,m,n+1}^{k+1,i} + \zeta_{l,m,n} - \frac{\lambda}{\mu} e_{r(l,m,n)} \right), \\ u_{l,m,n}^{k+1,i+1} &= \max \{ \min \{ \phi_{l,m,n}, 1 \}, 0 \}, \end{aligned} \quad (11)$$

where i is the iteration index for Gauss-Seidel iterative method and l, m, n are the indices of the voxel in axes x, y , and z , respectively. One has $u_{l,m,n}^{k+1,0} = u_{l,m,n}^k$.

After calculating an approximate u^{k+1} , we can obtain d^{k+1} by minimizing (8) with respect to d

$$d^{k+1} = \frac{\nabla u^{k+1} + b^k}{|\nabla u^{k+1} + b^k|} \max \left(\left| \nabla u^{k+1} + b^k \right| - \frac{1}{\lambda}, 0 \right). \quad (12)$$

Once u^{k+1} and d^{k+1} are available, the Bregman vector b^k can be updated according to (9). For more details of 2D Split Bregman method, we refer the readers to [11].

As a summary, the procedures of using Split Bregman method to solve (7) contain the following steps.

- (1) Initialization: b^0, d^0 and u^0 .
- (2) Fix u , calculate c_1 and c_2 according to (5), and further calculate e_r .
- (3) Update u^{k+1} by solving (11).
- (4) Update d^{k+1} by solving (12).

(5) Update b^{k+1} by solving (9).

(6) Convergence test: test whether a stable solution u has reached. If not, go to step (2).

(7) The objects are detected by thresholding $\Sigma = \{x : u(x) > \alpha\}$, where $\alpha \in [0, 1]$. In this paper, we choose $\alpha = 0.5$.

3. Experimental Results

3.1. Data. In this study, we selected three groups of quail hearts. Each group had five embryonic quail hearts at the development stage of days 6, 7, 8, 9, and 14, respectively. All the hearts were processed and imaged according to Section 2.1. The image size varied from $768 \times 768 \times 112$ (day 6) to $3075 \times 2560 \times 478$ (day 14). To build a database of manual segmentation for reference, we invited two biologists to independently segment the hearts manually with the software ITK-SNAP [21]. Due to the large size of the image and the complexity of the heart geometry, it typically took a biologist more than one week to finish one heart segmentation. For this reason, we currently only selected one group for manual segmentation.

3.2. Evaluation of Automatic Segmentation. Figure 2 shows one 3D and three 2D slice views of the quail heart at day 14 with two manual segmentations and one automatic segmentation. Although the image exhibits severe intensity inhomogeneity, visual inspection of the results shows that automatic segmentation can correctly capture most of the structures of the heart as manual segmentation. The most difference between manual and automatic segmentation occurs at the regions above the atrioventricular valve which can be observed in both 3D and 2D views. Because the contrast is very low at this region, automatic segmentation algorithm only uses image information can not detect the boundary precisely, while biologists using their knowledge can manually locate the boundary. What is more, we have also observed the presence of small objects within the heart chambers only detected by automatic segmentation. These small objects could be papillary muscle that can be considered as either a part of the myocardium or a part of the blood pool. As a result, both manual and automatic segmentation for these small objects are acceptable.

We also quantitatively evaluate our algorithm by measuring the overlap of automatic segmentation and manual segmentation by using Dice's similarity coefficient (DSC). For two segmentations S_1 and S_2 , the DSC value is defined as $2|S_1 \cap S_2| / (|S_1| + |S_2|)$. The DSC value is normalized, where 0 indicates complete dissimilarity and 1 indicates complete agreement. The overlap values reflecting the variability between the manual segmentations by two biologists are listed in the second row of Table 1. Except for days 6 and 7, all the DSC values are greater than 0.85, which means there is sufficient level of reliability for the two manual segmentations. The reason of low DSC values at days 6 and 7 is that the geometry of the hearts at these days is very complex as shown in Figure 3, and thus it is difficult for the biologists to achieve high agreement. The overlap

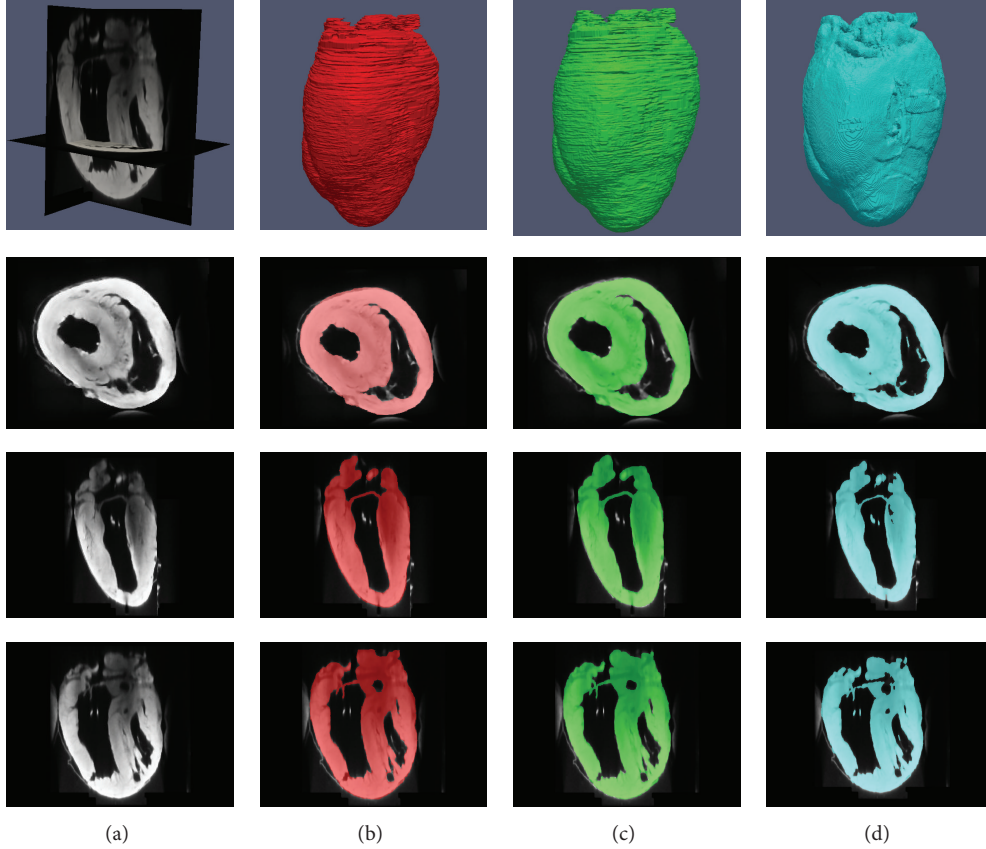


FIGURE 2: Visual comparison between manual segmentation and automatic segmentation. (a) Original 3D image and three slices in different views. (b) Manual segmentation done by the first biologist. (c) Manual segmentation done by the second biologist. (d) Automatic segmentation.

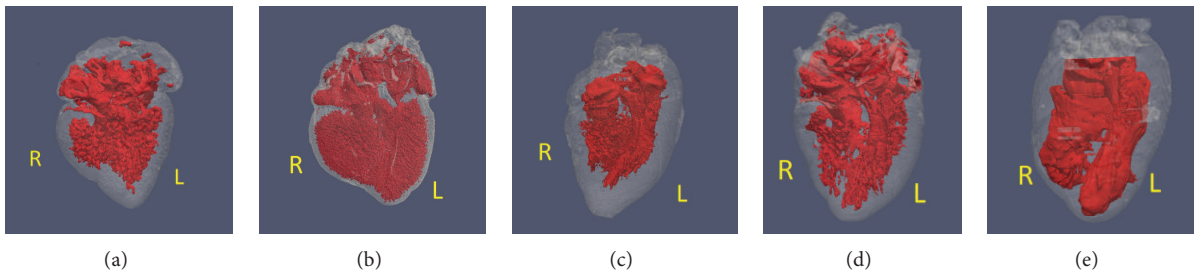


FIGURE 3: 3D segmentation of one group of the hearts. Columns from left to right are the heart at days 6, 7, 8, 9, and 14. For visualization purpose, the outer boundary is rendered as transparent (L: left ventricle. R: right ventricle).

comparison between automatic and manual segmentations is listed in the third and fourth rows of Table 1. Similarly, we can find the DSC values are low at days 6 and 7 and high at the rest. Overall, the overlap measures show that the automatic segmentation method has similar level of variability to the manual segmentation, which means our automatic segmentation method is applicable to EHM study.

3.3. EHM Study. Figure 3 shows automatic segmentation results of one group of hearts. As we can see, an obvious phenomenon of early heart development is the morphology

evolution of the ventricles. The left and right ventricles are merged together and exhibit sponge network structure at days 6 and 7 as the result of cardiac looping [4]. The interventricular septum starts to grow between day 7 and day 8, as the ventricles are partially separated at day 8. At day 9, the interventricular septum eventually forms and divides the ventricles into the left and right ventricle. However, the two ventricles still present some sponge structure at day 9. The shape of the ventricles eventually becomes mature at day 14.

We also quantify the average volume of the whole heart and the luminal space at different stages of development based on the segmentation results. We use the open source

TABLE 1: DSC values that measure the overlap between the two manual segmentations, the first manual segmentation against automatic segmentation and the second manual segmentation against automatic segmentation.

	Day 6	Day 7	Day 8	Day 9	Day 14
Biologist 1 versus biologist 2	0.75	0.79	0.85	0.87	0.93
Automatic versus biologist 1	0.65	0.72	0.78	0.85	0.88
Automatic versus biologist 2	0.68	0.75	0.79	0.81	0.91

TABLE 2: Average volume of the whole heart and the luminal space at different stages of development (mm^3).

	Day 6	Day 7	Day 8	Day 9	Day 14
Total heart	2.6	3.4	6.0	10.2	77.5
Luminal space	0.41	0.62	0.75	1.74	20.2

VTK library (<http://www.vtk.org/>) to calculate the average volume and list the average volume values in Table 2. We find that the average volume of the whole heart and the luminal space increased from 2.6 mm^3 to 77.5 mm^3 and 0.41 mm^3 to 20.2 mm^3 , respectively, which is nearly two orders of magnitude increase in an incubation period of approximately 10 days. This finding is similar in range to the findings in [8]. Furthermore, we also find that the average volume of the whole heart grows faster than the luminal space, which means that the myocardium grows towards both inside and outside.

4. Discussion

The technique outlined in this paper provided the framework of imaging and automatic segmentation of developing hearts for EHM study. By combining confocal microscopy imaging with optical clearing, our method was able to achieve penetration depth over 6 mm that enabled us to acquire volumetric images of the developing heart through the whole incubation period. We believe this imaging data can help biologists to understand more details of early heart development and investigate events that lead to congenital heart defects.

Image segmentation is always a headache for researchers in this field because of the complexity of the developing geometry. The convex active contour model proposed in this paper was a first step towards automatic segmentation in EHM study and showed promising results. One significant challenge in developing heart segmentation is the lack of a gold standard. Due to the expensive labor cost to label the images, we provided limited validation in the paper. In the future, we will build a larger manually segmented database for segmentation algorithm validation. What is more, this database could also be used for training and testing parameter-free machine learning algorithms.

The ultimate goal of this work will be heart growth modeling. Due to the complexity of developing heart, current heart growth modeling mainly focuses on very early stages of EHM [22]. To the best of our knowledge, there exist no works on modeling the whole EHM process from the single tube shape to four-chambered shape. With EHM knowledge from EHM study, we will work towards data-driven heart growth modeling.

5. Conclusion

We proposed an imaging approach and a novel automatic segmentation method for EHM study. We demonstrated the applicability of our imaging method to capture the 3D structure of embryonic quail hearts and also proved the efficiency of our segmentation algorithm for EHM study in both visual inspection and quantitative analysis. Based on the findings from EHM study, we believe this work could help us to further understand the fundamental mechanisms of embryonic heart development.

References

- [1] J. Icardo and F. Manasek, "Cardiogenesis: development mechanisms and embryology," in *The Heart and Cardiovascular System*, pp. 1563–1586, 1992.
- [2] World Health Organization, *Global Atlas on Cardiovascular Disease Prevention and Control*, Expert Review of Medical Devices, 2011.
- [3] J. Lactis and F. Manasek, "An analysis of deformation during a normal morphogenic event," *Morphogenesis and Malformation of the Cardiovascular System*, vol. 17, pp. 205–227, 1978.
- [4] L. A. Taber, B. B. Keller, and E. B. Clark, "Cardiac mechanics in the stage-16 chick embryo," *Journal of Biomechanical Engineering*, vol. 114, no. 4, pp. 427–434, 1992.
- [5] M. Liebling, J. Vermot, and S. E. Fraser, "Double time-scale image reconstruction of the beating and developing embryonic zebrafish heart," in *Proceedings of the 5th IEEE International Symposium on Biomedical Imaging*, pp. 855–858, May 2008.
- [6] B. C. W. Groenendijk, B. P. Hierck, J. Vrolijk et al., "Changes in shear stress-related gene expression after experimentally altered venous return in the chicken embryo," *Circulation Research*, vol. 96, no. 12, pp. 1291–1298, 2005.
- [7] M. Liebling, A. S. Forouhar, R. Wolleschensky et al., "Rapid three-dimensional imaging and analysis of the beating embryonic heart reveals functional changes during development," *Developmental Dynamics*, vol. 235, no. 11, pp. 2940–2948, 2006.
- [8] J. T. Butcher, D. Sedmera, R. E. Guldborg, and R. R. Markwald, "Quantitative volumetric analysis of cardiac morphogenesis assessed through micro-computed tomography," *Developmental Dynamics*, vol. 236, no. 3, pp. 802–809, 2007.
- [9] M. W. Jenkins, F. Rothenberg, D. Roy et al., "4D embryonic cardiography using gated optical coherence tomography," *Optics Express*, vol. 14, no. 2, pp. 736–748, 2006.

- [10] B. Smith, "Magnetic resonance microscopy in cardiac development," *Microscopy Research and Technique*, vol. 52, pp. 323–330, 2001.
- [11] T. Goldstein and S. Osher, "The split Bregman method for L1 regularized problems," *SIAM Journal on Imaging Sciences*, vol. 2, pp. 323–343, 2009.
- [12] H. Mao, H. Liu, and P. Shi, "A convex neighbor-constrained active contour model for image segmentation," in *Proceedings of the 17th IEEE International Conference on Image Processing (ICIP '10)*, pp. 793–796, September 2010.
- [13] J. Fishbaugh, M. Prastawa, S. Durrleman, J. Piven, and G. Gerig, "Analysis of longitudinal shape variability via subject specific growth modeling," in *Medical Image Computing and Computer Assisted Intervention*, pp. 731–738, 2012.
- [14] S. Durrleman, X. Pennec, A. Troune, G. Gerig, and N. Ayache, "Spatiotemporal atlas estimation for developmental delay detection in longitudinal datasets," in *Medical Image Computing and Computer Assisted Intervention*, pp. 297–304, 2009.
- [15] K. W. Fong, A. Toi, S. Salem et al., "Detection of fetal structural abnormalities with US during early pregnancy," *Radiographics*, vol. 24, no. 1, pp. 157–174, 2004.
- [16] E. A. Genina, A. N. Bashkatov, and V. V. Tuchin, "Tissue optical immersion clearing," *Expert Review of Medical Devices*, vol. 7, no. 6, pp. 825–842, 2010.
- [17] R. M. Smith, A. Matiukas, C. W. Zemlin, and A. M. Pertsov, "Nondestructive optical determination of fiber organization in intact myocardial wall," *Microscopy Research and Technique*, vol. 71, no. 7, pp. 510–516, 2008.
- [18] N. Dey, L. Blanc-Feraud, C. Zimmer et al., "Richardson-Lucy algorithm with total variation regularization for 3D confocal microscope deconvolution," *Microscopy Research and Technique*, vol. 69, no. 4, pp. 260–266, 2006.
- [19] T. F. Chan and L. A. Vese, "Active contours without edges," *IEEE Transactions on Image Processing*, vol. 10, no. 2, pp. 266–277, 2001.
- [20] X. Bresson, S. Esedoglu, P. Vandergheynst, J.-P. Thiran, and S. Osher, "Fast global minimization of the active contour/snake model," *Journal of Mathematical Imaging and Vision*, vol. 28, no. 2, pp. 151–167, 2007.
- [21] P. A. Yushkevich, J. Piven, H. C. Hazlett et al., "User-guided 3D active contour segmentation of anatomical structures: significantly improved efficiency and reliability," *NeuroImage*, vol. 31, no. 3, pp. 1116–1128, 2006.
- [22] S. Goenezen, M. Rennie, and S. Rugonyi, "Biomechanics of early cardiac development," *Biomechanics and Modeling in Mechanobiology*, vol. 11, pp. 1187–1204, 2012.

Research Article

Accelerating Dynamic Cardiac MR Imaging Using Structured Sparse Representation

Nian Cai,¹ Shengru Wang,^{1,2,3} Shasha Zhu,¹ and Dong Liang^{2,3}

¹ School of Information Engineering, Guangdong University of Technology, Guangzhou 510006, China

² Paul C. Lauterbur Research Centre for Biomedical Imaging, Shenzhen Institutes of Advanced Technology, Shenzhen 518055, China

³ Shenzhen Key Laboratory for MRI, Guangdong, Shenzhen 518055, China

Correspondence should be addressed to Dong Liang; dong.liang@siat.ac.cn

Received 20 October 2013; Accepted 21 November 2013

Academic Editor: Linwei Wang

Copyright © 2013 Nian Cai et al. This is an open access article distributed under the Creative Commons Attribution License, which permits unrestricted use, distribution, and reproduction in any medium, provided the original work is properly cited.

Compressed sensing (CS) has produced promising results on dynamic cardiac MR imaging by exploiting the sparsity in image series. In this paper, we propose a new method to improve the CS reconstruction for dynamic cardiac MRI based on the theory of structured sparse representation. The proposed method uses the PCA subdictionaries for adaptive sparse representation and suppresses the sparse coding noise to obtain good reconstructions. An accelerated iterative shrinkage algorithm is used to solve the optimization problem and achieve a fast convergence rate. Experimental results demonstrate that the proposed method improves the reconstruction quality of dynamic cardiac cine MRI over the state-of-the-art CS method.

1. Introduction

Dynamic cardiac cine MR imaging aims at simultaneously providing a series of dynamic magnetic resonance image in spatial and temporal domains (x - t space) at a high frame rate. It usually acquires the k -space at each time frame and collects the raw data in the spatial frequency and temporal domain, the so called k - t space. Therefore, it is necessary to reconstruct each time frame and get a series of dynamic images. However, the relatively low acquisition speed of the dynamic MRI is an important factor to limit its application in clinics. How to accelerate k -space sampling for each time frame and reconstruct them without sacrificing spatial resolution is a challenging problem.

In recent years, many advanced techniques [1–10] were proposed to effectively address this issue and can be divided into two categories. One is based on compressed sensing (CS) theory [11, 12] utilizing the sparsity in dynamic images to be reconstructed, and the other is based on the partial separable theory [13] exploiting the low-rank property of images in x - t space. The application of CS in dynamic MRI has drawn a lot of attention, since this theory demonstrates that the signal

can be accurately reconstructed from a small amount of linear undersampled measurements by exploiting the inherent sparsity in signal. For example, Jung et al. [7, 9] uncovered an intriguing link between the compressed sensing and k - t BLAST/SENSE and proposed the k - t FOCUSS algorithm to achieve high spatiotemporal resolution in cardiac cine imaging. Liang et al. [5] developed k - t iterative support detection (k - t ISD) method to further utilize the detected partial support information besides the sparsity in cardiac cine images.

Recently, image restoration with patch-based sparse representations has attracted a lot of attention. The similarity of works in this topic is seeking for a more appropriate way to sparsify the image patches than conventional fixed transform. One approach is to provide additional information when using fixed transform on patches. For example, Qu et al. [14] presented to provide the sparsest representation for each image patch by estimating geometric directions. In [15], the nonlocal patches with intensity similarity, instead of those from neighbors, are grouped and then transformed by using a 3D Haar wavelet to produce sparser representation. These two patch-based methods exhibited consistent improvements in

reconstruction accuracy over conventional CS-MRI methods. Another approach is based on the dictionary learning technique which aims to learn an adaptive basis from image patches and has shown impressive image restoration results [16]. The essential difference between these two approaches is that the latter uses adaptive learned dictionary instead of fixed basis, such as temporal Fourier transform, as the sparsifying transform. Ravishankar and Bresler [17] have applied the dictionary learning technique to static MR image reconstruction and obtained better reconstruction results than the state-of-the-art methods using fixed sparsifying transform. Liu et al. [18] presented to train dictionaries from the patches of the horizontal and vertical gradient images instead of the pixel domain image. The sparser training samples from the gradient images that are already sparsified by gradient operators result in sparser representation. In [19], a two-level Bregman method with dictionary learning updating is developed by applying the outer-level and inner-level Bregman iterative procedures to update the whole image and image patches, respectively. Experimental results on static MR images demonstrate the superiority of the presented algorithm to the state-of-the-art reconstruction methods.

However, dictionary learning based optimization is a large-scale and highly nonconvex problem, which requires high computational complexity. The coherence of the dictionary and the large degree of freedom may become sources of instability and errors. Structured sparse representation model was proposed to reduce the degree of freedom in the estimations and was thus more stable than conventional sparse representation model. The structured learned overcomplete dictionary, composed of a union of bases of principal component analysis (PCA), was widely used in image restoration [20, 21]. Recently, Dong et al. [22] proposed nonlocally centralized sparse representation (NCSR) model for single natural image restoration, specifically, clustering image patches by K -means algorithm at first and then learning PCA subdictionary of each cluster to sparsely represent image patches. Finally, the so-called sparse coding noise (SCN) was minimized to improve the performance of sparsity-constrained image restoration. This model has gotten the satisfactory results on image deblurring, image denoising, and image super resolution.

In this work, motivated by the effective representation ability of NCSR, a novel method based on the NCSR model is proposed to accelerate dynamic cardiac MRI applications. The method utilizes structured sparse dictionary learning to adaptively represent image sequence and reduces the error between the sparse coding coefficients learned by such dictionary and true sparse coding. Improvement of the proposed method over the basic CS approach is demonstrated using retrospectively undersampled in vivo cardiac cine MR datasets.

The rest of the paper is organized as follows. In Section 2, the NCSR model is briefly described and a detailed account of structured sparse representation-based dynamic cardiac MR imaging method is provided. We present experimental validation of our method and compare it to previous state-of-the-art method in Section 3. Conclusions are drawn in Section 4.

2. Materials and Methods

2.1. Nonlocally Centralized Sparse Representation (NCSR). Image restoration often requires solving an inverse problem. It amounts to estimate original image vector x from a vector of measurements y ; that is, we have

$$y = \mathbf{H}x + v, \quad (1)$$

which is obtained through the noninvertible linear degradation operator \mathbf{H} and is contaminated by the additive noise v .

Mathematically, image vector $x \in C^N$ can be represented as $x \approx \Phi\alpha$ under the sparse representation framework, where $\Phi \in C^{N \times M}$, $N < M$ is a dictionary, and $\alpha \in C^M$ represents the sparse coefficients. The sparse decomposition of x can be obtained by solving a convex l_1 -minimization problem:

$$\alpha_x = \arg \min_{\alpha} \left\{ \|x - \Phi\alpha\|_2^2 + \lambda \|\alpha\|_1 \right\}. \quad (2)$$

In the scenario of image restoration, to recover x from the degraded image, y is first sparsely coded with respect to Φ by solving the following optimization problem:

$$\alpha_y = \arg \min_{\alpha} \left\{ \|y - \mathbf{H}\Phi\alpha\|_2^2 + \lambda \|\alpha\|_1 \right\}. \quad (3)$$

And then x is reconstructed by $\hat{x} = \Phi\alpha_y$. In order to achieve an effective image restoration, α_y are expected to be as close as possible to approach the true sparse codes α_x of the original image x . Dong et al. defined the sparse coding noise (SCN) as the difference between α_y and α_x :

$$v_{\alpha} = \alpha_y - \alpha_x. \quad (4)$$

Thus, the quality of image restoration can be improved by suppressing SCN. However, α_x is unknown so SCN cannot be directly measured. To address this issue, a good estimation β of α_x is necessary. There are various ways to obtain an accurate estimate of α_x . Dong et al. tried to learn the estimate β by computing the weighted average of the sparse codes of nonlocal similar patches.

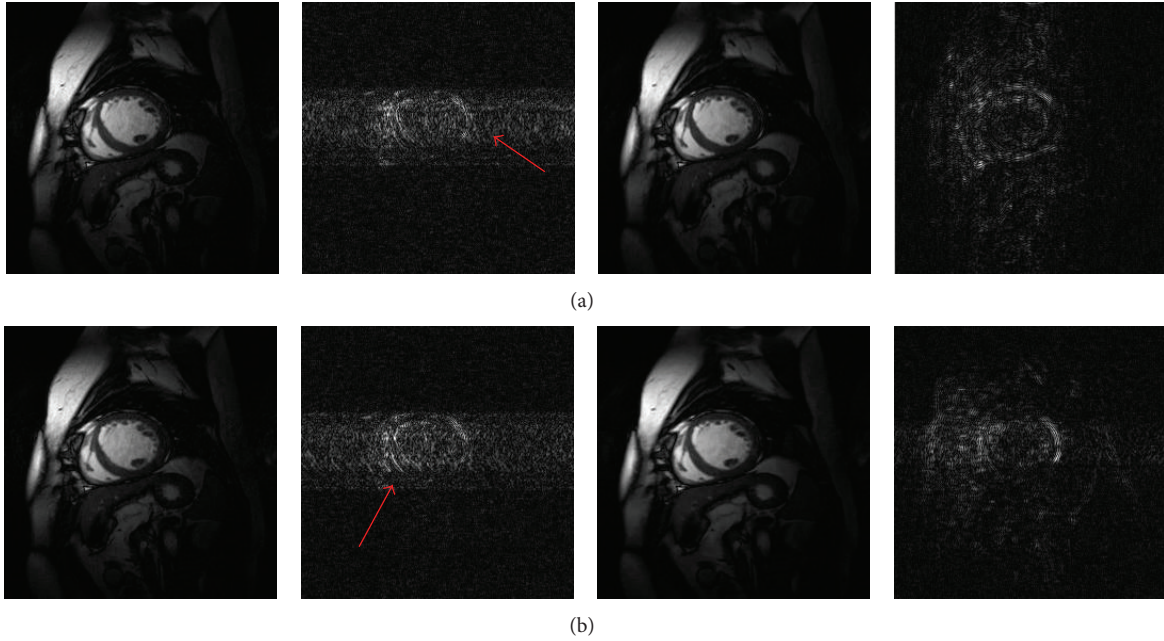
The NCSR model was proposed as follows:

$$\alpha_y = \arg \min_{\alpha} \left\{ \|y - \mathbf{H}\Phi\alpha\|_2^2 + \lambda \sum_i \|\alpha_i - \beta_i\|_1 \right\}, \quad (5)$$

where dictionary Φ can be designed as a PCA-based structured sparse dictionary, α_i denotes the sparse coding vector of i th image patch on a certain subdictionary, and λ is the regularization parameter controlling the tradeoff between data consistency and sparse coding noise. To solve this problem, firstly, the training patches extracted from the given image are clustered into K clusters, and a PCA subdictionary is learned for each corresponding cluster. Then one PCA subdictionary is adaptively selected to code a given patch. Finally, an iterative shrinkage algorithm [23] can be used to solve the NCSR objective function in (5).

- (1) Initialization:
Set the initial estimate $\widehat{\mathbf{X}}^{(1)} = \mathbf{Y}$, $\widehat{\mathbf{X}}^{(0)} = \mathbf{0}$ and the regularization parameter λ ;
- (2) Outer loop (dictionary learning and clustering): iterate on $l = 1, 2, \dots, L$
- (a) Update the dictionaries $\{\Phi_k\}$ via k -means and PCA;
- (b) Inner loop (clustering): iterate on $j = 1, 2, \dots, J$
- (b.1) $a(j) = 1 + (j-1)/(j+2)$, $b(j) = -(j-1)/(j+2)$
- (b.2) Compute $g_s^{(j)} = a(j)x_s^{(j)} + b(j)x_s^{(j-1)}$ and
 $g_s^{(j+1/2)} = g_s^{(j)} + \lambda \mathbf{F}_{\mathbf{u}_s}^T (y_s - \mathbf{F}_{\mathbf{u}_s} g_s^{(j)})$ for $s = 1, 2, \dots, S$;
- (b.3) Compute $v^{(j)} = [\Phi_{k_1}^T \mathbf{X}_1^{(j+1/2)}, \dots, \Phi_{k_N}^T \mathbf{X}_N^{(j+1/2)}]$, where Φ_{k_n} is the dictionary assigned to patch;
- (b.4) Compute the $\alpha_i^{(j+1)}$ using the shrinkage operator given in (8);
- (b.5) Update the estimate $\{\beta_i\}$;
- (b.6) Image matrix estimate update: $\mathbf{X}^{(j+1)} = \Phi \alpha^{(j+1)}$.

ALGORITHM 1: NCSR-based dynamic cardiac cine MR imaging.

FIGURE 1: Experiment results in (a) $R = 3$ and (b) $R = 4$. Reconstructions at the 4th frame using k - t FOCUSS (the 1st column) and proposed method (the 3rd column) and their corresponding difference images (2nd and 4th columns).

2.2. NCSR-Based Dynamic Cardiac MR Imaging. When the degradation operator \mathbf{H} is the under-sampled Fourier encoding operator and y is the acquired k -space data, we can modify the above model to MR image reconstruction. Based on the NCSR model, we propose a new method to reconstruct a time series of dynamic cardiac cine MR images which have high correlations in the spatial- and temporal-domain.

We define a matrix of image series $\mathbf{X} = [x_1, \dots, x_S] \in \mathbb{C}^{N \times S}$, whose columns are the image vectors $\{x_s\}$, $s = 1, \dots, S$. S denotes the number of image frames. In order to reconstruct the image series, we propose the following cardiac cine MRI reconstruction model:

$$\min_{\alpha} \|\mathbf{Y} - \mathbf{F}_{\mathbf{u}_\Omega} \Phi \alpha\|_2^2 + \lambda \sum_{i=1}^N \|\alpha_i - \beta_i\|_1, \quad (6)$$

where $\mathbf{X} = \Phi \alpha$ and $\mathbf{Y} \in \mathbb{C}^{N \times S}$ is the acquired k -space data matrix, whose columns are the vector form of k -space data of images $\{x_s\}$. Matrix operator $\mathbf{F}_{\mathbf{u}_\Omega}$ performs the undersampled Fourier encoding, and set $\Omega = \{1, 2, \dots, S\}$ indicates that the undersampling masks are different for each frame to enforce incoherence. For the selection of the dictionary Φ , we adopt the PCA-based structured sparse dictionary like in NCSR. However, the way to get the patches from the image series $\{x_s\}$ is different from NCSR. We first transform the image series $\{x_s\}$ to the image matrix \mathbf{X} defined above and then regard the transpose vector of each row \mathbf{x}_n , $n = 1, \dots, N$, of \mathbf{X} as a patch vector. In other words, we learn the PCA subdictionaries along the temporal dimension to exploit the inherent correlation in dynamic image series. After getting the patches, we use the K -means algorithm to partition the

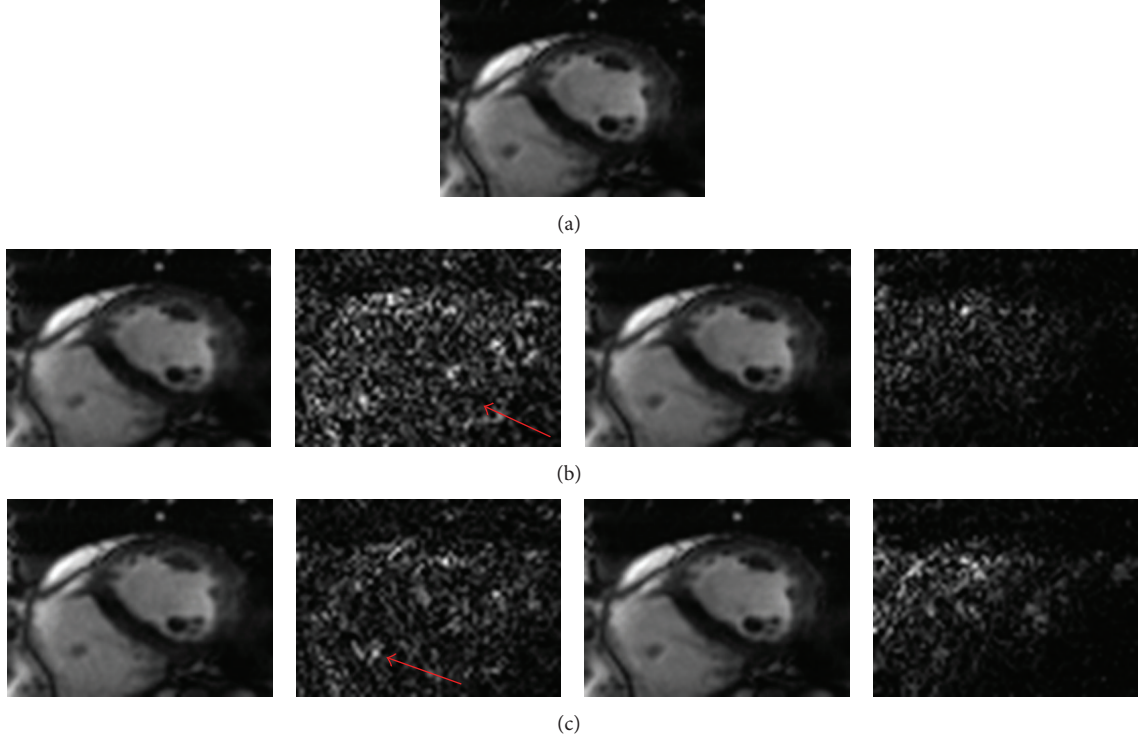


FIGURE 2: Experiment results of the second dataset in (b) $R = 3$ and (c) $R = 4$. Reconstructions at the 15th frame using k - t FOCUSS (the 1st column) and proposed method (the 3rd column) and their corresponding difference images. (a) is the full FOV and ROI reference.

patch set into K clusters $\{C_1, C_2, \dots, C_K\}$ and then compute the covariance matrix Σ_k of each cluster C_k . An orthogonal transformation matrix \mathbf{P}_k can be obtained by applying PCA to Σ_k . We set \mathbf{P}_k as the PCA subdictionary which can constitute the dictionary Φ .

The iterative shrinkage algorithm is used to solve this problem and the final image series can be obtained from the solved sparse coding vector. Specifically, at each iteration, we use the same method as in NCSR to compute β_i . For each local patch, the Euclidean distance was used to search for the first P ($P = 13$ in our experiments) closest patches. We applied the corresponding subdictionary to these nonlocal similar patches to obtain their sparse codes. β_i was estimated by computing the weighted average of these sparse codes. This nonlocal method can produce accurate enough estimates of true sparse codes. Finally, the following minimization problem can be solved for a given β_i :

$$\alpha_y = \arg \min_{\alpha} \left\{ \|\mathbf{Y} - \mathbf{F}_{\mathbf{u}_\Omega} \Phi \alpha\|_2^2 + \sum_i \sum_j \lambda |\alpha_i(j) - \beta_i(j)| \right\}, \quad (7)$$

where $\alpha_i(j)$ and $\beta_i(j)$ are the j th elements of α_i, β_i . We adopted the surrogate algorithm in [23] to solve (7). In the $(l+1)$ th iteration, the proposed shrinkage operator for the j th elements of α_i is

$$\alpha_i^{(l+1)}(j) = S_\tau \left(v_{i,j}^{(l)} - \beta_i(j) \right) + \beta_i(j), \quad (8)$$

where $S_\tau(\cdot)$ is the classic soft thresholding operator. $v^{(l)} = \mathbf{K}^H (\mathbf{Y} - \mathbf{K} \alpha^{(l)}) / c + \alpha^{(l)}$, where $\mathbf{K} = \mathbf{F}_{\mathbf{u}_\Omega} \Phi$, $\tau = \lambda / c$, and c is a parameter guaranteeing the convexity of the surrogate function ($c = 1$ in our experiments).

Since one drawback of this iterative framework is the slow convergence rate of $O(1/n)$, we introduce an accelerated method described in [24] to achieve a fast $O(1/n^2)$ convergence rate. In this method, two prior iterates are used to obtain the next updated solution in the soft thresholding framework. The detailed design is described in Algorithm 1 (b.1) and (b.2).

3. Experimental Results

The feasibility of the proposed method was validated on two sets of in vivo dynamic cardiac cine data. Informed consent was obtained from the volunteer in accordance with the institutional review board policy. The full k -space data with the size of $256 \times 256 \times 25$ (number of frequency encoding \times number of phase encoding \times number of frames) of the first dataset was acquired using a steady-state free precession (SSFP) sequence on a 1.5 T Philips scanner. The flip angle was 50 degrees and TE/TR = 1.7/3.45 msec. The field of view (FOV) was 345 mm \times 270 mm and the slice thickness was 10 mm. Retrospective cardiac gating was used with a heart rate of 66 bpm. The second dataset was acquired on a 3 T Siemens Trio scanner (Siemens Medical Solutions, Erlangen, Germany) with a flip angle of 44 degrees and TE/TR = 42.5/1.22 msec. The fully acquired k - t measurements were of

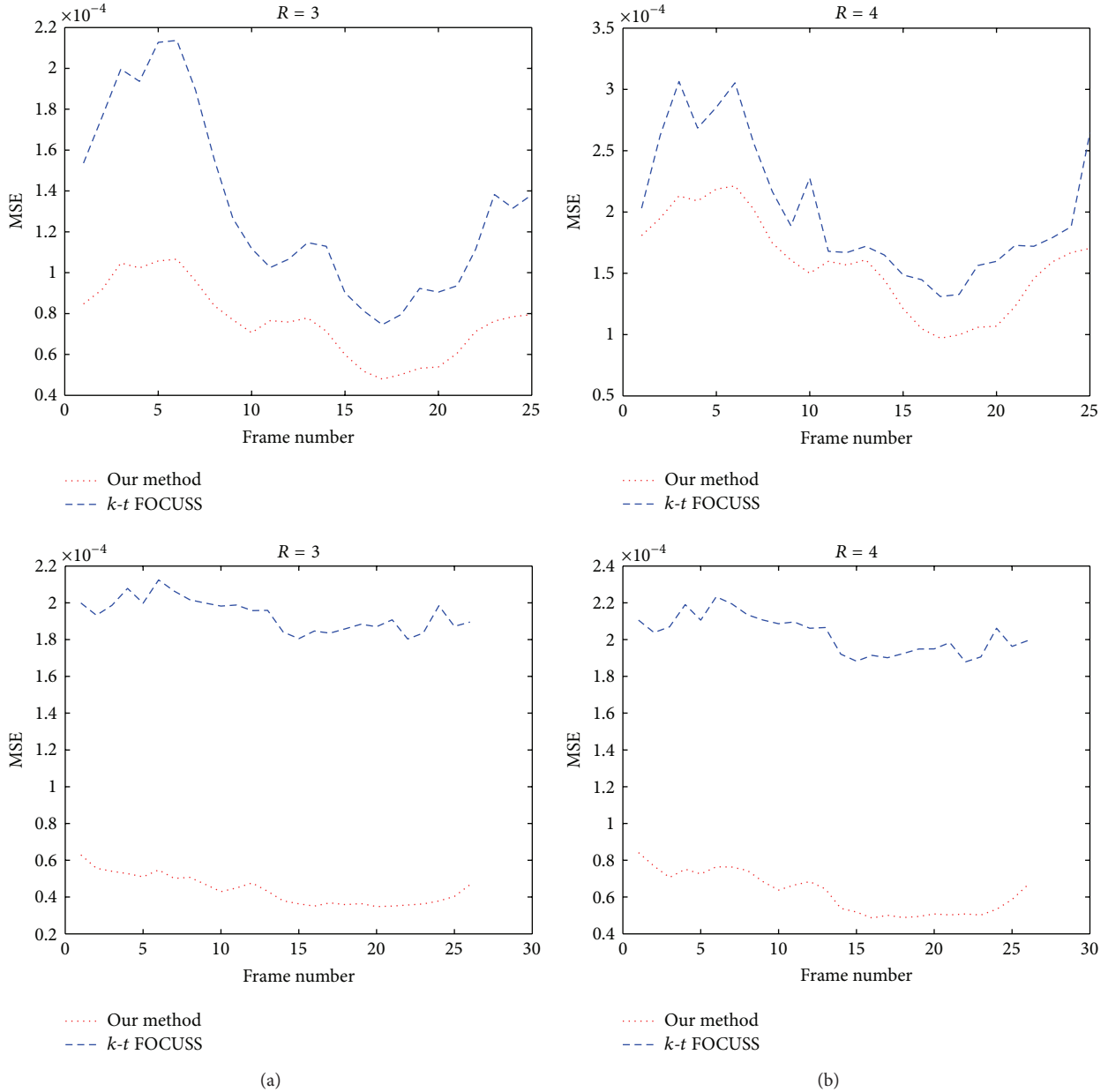


FIGURE 3: Frame-by-frame plots of NMSE for $k-t$ FOCUSS and our method with (a) $R = 3$ and (b) $R = 4$ in the first dataset (the 1st row) and the second dataset (the 2nd row). The dotted lines are for our method and dashed lines for $k-t$ FOCUSS.

size $304 \times 165 \times 26 \times 12$. The FOV was $340 \text{ mm} \times 276 \text{ mm}$ and the slice thickness was 6 mm .

The image series reconstructed from the full $k-t$ data was used as the reference for comparison, while, for the dataset acquired using multiple coils, the image from each channel was reconstructed from full samples and combined using square root of sum-of-squares (SOS) as the reference. To simulate the undersampled k -space data, the sampling masks corresponding to reduction factors, $R = 3$ and 4 , were generated using the function provided in the $k-t$ FOCUSS toolbox, where the central 8 phase encoding lines were fully sampled. The fully sampled data were then retrospectively undersampled using the designed sampling masks.

The proposed NCSR-based method and $k-t$ FOCUSS were used to reconstruct the desired image series with the same sampling patterns for a given undersampled dataset. All methods were implemented in Matlab and the code for $k-t$ FOCUSS was obtained from <http://bisp.kaist.ac.kr/ktFOCUSS.htm>. Simulations run on a dual core 2.6 GHz CPU laptop with 4 GB RAM. The running time of our program is about 30 minutes. This time is relatively long due to slow speed in dictionary learning and K -means clustering and can be reduced by optimizing the code and utilizing GPU for acceleration.

The reconstructions with reduction factors of $R = 3$ and 4 and the corresponding difference images at the fourth

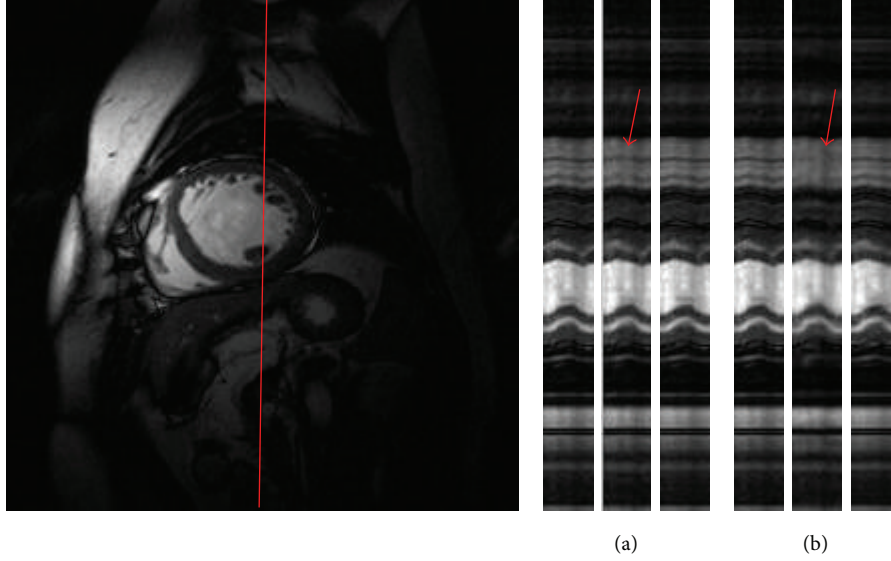


FIGURE 4: The temporal profiles in $x-t$ plane of different reconstruction methods with (a) $R = 3$ and (b) $R = 4$ in the first experiment. The results are from reference (left), $k-t$ FOCUSS (middle), and our method (right) for each reduction factor.

frame of the first dynamic cardiac dataset are shown in Figures 1(a) and 1(b), respectively. In Figure 1, the first row shows the results of $k-t$ FOCUSS (the left two) and proposed method (the right two) in $R = 3$, and the second row is the results of two methods in $R = 4$. It can be seen from the reconstructed images that the $k-t$ FOCUSS presents more undersampling artifacts along the phase encoding direction. Our method greatly suppresses the artifacts and obtains high quality reconstructions. The superiority of structured sparse representation based method is also clearly seen in the difference images as shown by the red arrows. Figures 2(b) and 2(c) show the region-of-interest (ROI) reconstructions using $k-t$ FOCUSS and the proposed method (from left to right) with $R = 3$ and 4 (from top to left) of the second dynamic cardiac dataset. We can find some artifacts appearing in the $k-t$ FOCUSS result especially with a reduction factor of 4.

To quantify the improvement of the proposed method over $k-t$ FOCUSS, the normalized mean-squared error (NMSE) between the reconstruction and the reference at $R = 3$ and 4 was calculated and plotted as a function of time frame in Figures 3(a) and 3(b), respectively. The nRMSE was calculated using the following formula:

$$\text{nRMSE} = \sqrt{\frac{\sum_{i=1}^N (\mathbf{x}_{\text{rec}}(i) - \mathbf{x}(i))^2}{\sum_{i=1}^N \mathbf{x}(i)^2}}, \quad (9)$$

where \mathbf{x}_{rec} is the reconstructed images from the undersampled data, \mathbf{x} is the reference, and N is the image size. The dotted lines are for our method and dashed lines for $k-t$ FOCUSS, respectively. Our method is seen to have a lower MSE than $k-t$ FOCUSS for all frames at specified reduction factors.

The ability to catch the dynamic motion along temporal direction is a key factor for comparing different dynamic

reconstruction methods. To evaluate the temporal fidelity, we show in Figure 4 the reconstructions in $x-t$ plane of the first dataset with $R = 3$ and 4 for a fixed position in the frequency-encoding direction. It is seen that $k-t$ FOCUSS shows some loss of contrast. In comparison, the proposed method preserves more temporal variations especially in regions indicated by red arrows.

In our algorithm, a regularization parameter λ was introduced. This parameter controls the tradeoff between the data fidelity and the accuracy of the sparse codes, and it also affects the thresholds τ in (8). In this work, λ was elaborately tuned in a parameter range. To show the effects of this parameter on final reconstructions, the curves of NMSE with respect to parameter λ for the 10th frame of the first dynamic cardiac dataset at $R = 3$ and 4 were plotted in Figure 5. We can find that the reconstructions are relatively robust to this parameter. Results with least NMSE are obtained when $\lambda = 0.0015$ with $R = 3$ and $\lambda = 0.002$ with $R = 4$. In our experiments, we empirically set $\lambda = 0.002$.

The convergence behavior is an important factor in evaluating the performance of the proposed method. The corresponding NMSE-iteration plots are shown in Figure 6 when $R = 3$ and 4 for the first dataset. It can be seen that the NMSE decreases fast at the first few iterations and then becomes flatter and reaches the convergence zone after 6 outer iterations.

From the above experimental results, we can find that our method produces more accurate reconstruction on image sequence than $k-t$ FOCUSS. It is because we force the sparse coefficients of dictionary learning to approach the true sparse coding, which is estimated through the nonlocal similarity technique. This technique was proved to be an effective method using image redundancy and therefore the accurate sparse representation promotes the quality of reconstruction.

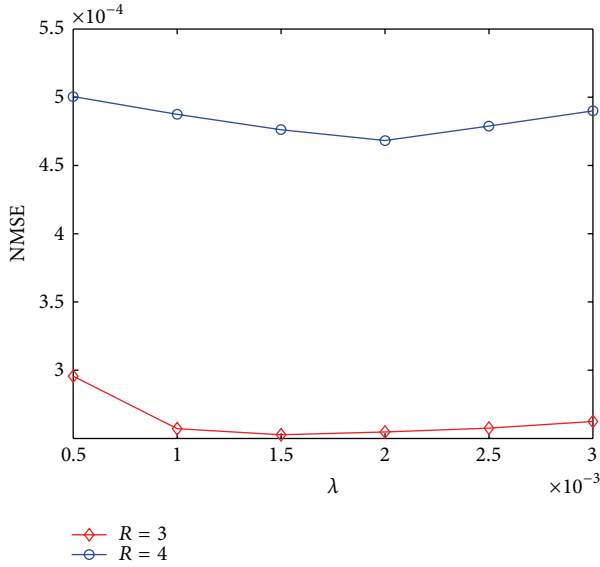


FIGURE 5: NMSE of 10th frame of the first dynamic cardiac dataset versus regularization parameter λ with $R = 3$ and 4.

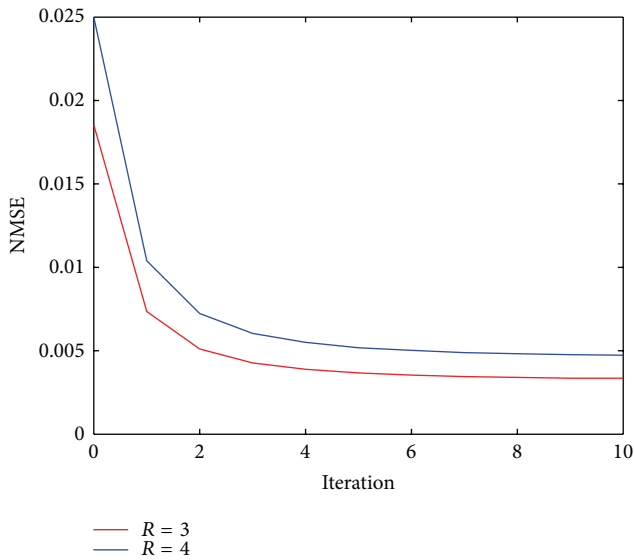


FIGURE 6: NMSE curves of the first dynamic cardiac dataset versus outer iteration number with $R = 3$ and 4.

4. Conclusions

In this work, we propose a novel dynamic cardiac MR imaging method based on the NCSR model. This method sparsely codes the image sequence by adaptively learning PCA-based structured sparse dictionary and recovers the true sparse coding coefficients with a centralized sparse constraint, which effectively exploits the image nonlocal redundancy. An accelerated iterative shrinkage method was presented for solving the proposed model. From the experimental results from in vivo dynamic cardiac cine MR imaging, it is proved that the proposed method could produce fewer artifacts and preserve contrast than the state-of-the-art method.

Conflict of Interests

The authors declare that there is no conflict of interests regarding the publication of this paper.

Acknowledgments

The authors would like to thank Ye et al. for sharing their experiment materials and source codes of k - t FOCUSS. This work was partly supported by the National Natural Science Foundation of China (Grant nos. 61001179, 61102043, 61372173, and 81120108012), the Shenzhen Peacock Plan (KQCX20120816155710259), and the Basic Research Program of Shenzhen (JC201104220219A).

References

- [1] A. Majumdar, R. K. Ward, and T. Aboulnasr, "Compressed sensing based Real-Time dynamic MRI reconstruction," *IEEE Transactions on Medical Imaging*, vol. 31, no. 12, pp. 2253–2266, 2012.
- [2] B. Zhao, J. P. Haldar, C. Brinegar, and Z.-P. Liang, "Low rank matrix recovery for real-time cardiac MRI," in *Proceedings of the 7th IEEE International Symposium on Biomedical Imaging: From Nano to Macro (ISBI '10)*, pp. 996–999, Rotterdam, The Netherlands, April 2010.
- [3] J. P. Haldar and Z.-P. Liang, "Low-rank approximations for dynamic imaging," in *Proceedings of the 8th IEEE International Symposium on Biomedical Imaging: From Nano to Macro (ISBI '11)*, pp. 1052–1055, Chicago, Ill, USA, April 2011.
- [4] S. G. Lingala, Y. Hu, E. Dibella, and M. Jacob, "Accelerated dynamic MRI exploiting sparsity and low-rank structure: k-t SLR," *IEEE Transactions on Medical Imaging*, vol. 30, no. 5, pp. 1042–1054, 2011.
- [5] D. Liang, E. V. R. Dibella, R.-R. Chen, and L. Ying, "k-t ISD: dynamic cardiac MR imaging using compressed sensing with iterative support detection," *Magnetic Resonance in Medicine*, vol. 68, no. 1, pp. 41–53, 2012.
- [6] M. Lustig, J. M. Santos, D. L. Donoho, and J. M. Pauly, "k-t SPARSE: high frame rate dynamic MRI exploiting spatio-temporal sparsity," in *Proceedings of the 14th Annual Meeting of ISMRM*, p. 2420, Seattle, Wash, USA, 2006.
- [7] H. Jung, J. C. Ye, and E. Y. Kim, "Improved k-t BLAST and k-t SENSE using FOCUSS," *Physics in Medicine and Biology*, vol. 52, no. 11, article 018, pp. 3201–3226, 2007.
- [8] U. Gamper, P. Boesiger, and S. Kozerke, "Compressed sensing in dynamic MRI," *Magnetic Resonance in Medicine*, vol. 59, no. 2, pp. 365–373, 2008.
- [9] H. Jung, K. Sung, K. S. Nayak, E. Y. Kim, and J. C. Ye, "k-t FOCUSS: a general compressed sensing framework for high resolution dynamic MRI," *Magnetic Resonance in Medicine*, vol. 61, no. 1, pp. 103–116, 2009.
- [10] L. Feng, M. B. Srichai, R. P. Lim et al., "Highly accelerated real-time cardiac cine MRI using kt SPARSE-SENSE," *Magnetic Resonance in Medicine*, vol. 70, no. 1, pp. 64–74, 2013.
- [11] D. L. Donoho, "Compressed sensing," *IEEE Transactions on Information Theory*, vol. 52, no. 4, pp. 1289–1306, 2006.
- [12] E. J. Candès, J. Romberg, and T. Tao, "Robust uncertainty principles: exact signal reconstruction from highly incomplete frequency information," *IEEE Transactions on Information Theory*, vol. 52, no. 2, pp. 489–509, 2006.

- [13] Z.-P. Liang, "Spatiotemporal imaging with partially separable functions," in *Proceedings of the 4th IEEE International Symposium on Biomedical Imaging: From Nano to Macro (ISBI '07)*, pp. 988–991, Arlington, Va, USA, April 2007.
- [14] X. Qu, D. Guo, B. Ning et al., "Undersampled MRI reconstruction with patch-based directional wavelets," *Magnetic Resonance Imaging*, vol. 30, no. 7, pp. 964–977, 2012.
- [15] X. B. Qu, Y. K. Hou, F. Lam, D. Guo, J. H. Zhong, and Z. Chen, "Magnetic resonance image reconstruction from undersampled measurements using a patch-based nonlocal operator," *Medical Image Analysis*, 2013.
- [16] M. Aharon, M. Elad, and A. Bruckstein, "K-SVD: an algorithm for designing overcomplete dictionaries for sparse representation," *IEEE Transactions on Signal Processing*, vol. 54, no. 11, pp. 4311–4322, 2006.
- [17] S. Ravishankar and Y. Bresler, "MR image reconstruction from highly undersampled k-space data by dictionary learning," *IEEE Transactions on Medical Imaging*, vol. 30, no. 5, pp. 1028–1041, 2011.
- [18] Q. G. Liu, S. S. Wang, L. Ying, X. Peng, Y. J. Zhu, and D. Liang, "Adaptive dictionary learning in sparse gradient domain for image recovery," *IEEE Transactions on Image Processing*, vol. 22, no. 12, pp. 4652–4663, 2013.
- [19] Q. G. Liu, S. S. Wang, K. Yang, J. H. Luo, Y. M. Zhu, and D. Liang, "Highly undersampled magnetic resonance imaging reconstruction using two-level Bregman method with dictionary updating," *IEEE Transactions on Medical Imaging*, vol. 32, no. 7, pp. 1290–1301, 2013.
- [20] G. Yu, G. Sapiro, and S. Mallat, "Solving inverse problems with piecewise linear estimators: from gaussian mixture models to structured sparsity," *IEEE Transactions on Image Processing*, vol. 21, no. 5, pp. 2481–2499, 2012.
- [21] D. Zoran and Y. Weiss, "From learning models of natural image patches to whole image restoration," in *Proceedings of the IEEE International Conference on Computer Vision (ICCV '11)*, pp. 479–486, Barcelona, Spain, November 2011.
- [22] W. Dong, L. Zhang, G. Shi, and X. Li, "Nonlocally centralized sparse representation for image restoration," *IEEE Transactions on Image Processing*, vol. 22, no. 4, pp. 1620–1630, 2013.
- [23] I. Daubechies, M. Defrise, and C. de Mol, "An iterative thresholding algorithm for linear inverse problems with a sparsity constraint," *Communications on Pure and Applied Mathematics*, vol. 57, no. 11, pp. 1413–1457, 2004.
- [24] K. Khare, C. J. Hardy, K. F. King, P. A. Turski, and L. Marinelli, "Accelerated MR imaging using compressive sensing with no free parameters," *Magnetic Resonance in Medicine*, vol. 68, no. 5, pp. 1450–1457, 2012.

Research Article

Three-Dimensional Reconstruction of Thoracic Structures: Based on Chinese Visible Human

Yi Wu,¹ Na Luo,² Liwen Tan,¹ Binji Fang,¹ Ying Li,¹ Bing Xie,¹
Kaijun Liu,¹ Chun Chu,¹ Min Li,³ and Shaoxiang Zhang¹

¹ Institute of Computing Medicine and Department of Human Anatomy, Third Military Medical University, Chongqing 400038, China

² Department of Dermatology, Southwest Hospital, Third Military Medical University, Chongqing 400038, China

³ Institute of Bioengineering, Chongqing University, Chongqing 400044, China

Correspondence should be addressed to Shaoxiang Zhang; zhangsx1021@yahoo.com

Received 25 August 2013; Accepted 31 October 2013

Academic Editor: Heye Zhang

Copyright © 2013 Yi Wu et al. This is an open access article distributed under the Creative Commons Attribution License, which permits unrestricted use, distribution, and reproduction in any medium, provided the original work is properly cited.

We managed to establish three-dimensional digitized visible model of human thoracic structures and to provide morphological data for imaging diagnosis and thoracic and cardiovascular surgery. With Photoshop software, the contour line of lungs and mediastinal structures including heart, aorta and its ramus, azygos vein, superior vena cava, inferior vena cava, thymus, esophagus, diaphragm, phrenic nerve, vagus nerve, sympathetic trunk, thoracic vertebrae, sternum, thoracic duct, and so forth were segmented from the Chinese Visible Human (CVH)-1 data set. The contour data set of segmented thoracic structures was imported to Amira software and 3D thorax models were reconstructed via surface rendering and volume rendering. With Amira software, surface rendering reconstructed model of thoracic organs and its volume rendering reconstructed model were 3D reconstructed and can be displayed together clearly and accurately. It provides a learning tool of interpreting human thoracic anatomy and virtual thoracic and cardiovascular surgery for medical students and junior surgeons.

1. Introduction

The thorax is an important chamber of human body and is protected by the thoracic wall including thoracic cage and associated skin, muscle, and fascia. It is separated from the abdominal cavity by the diaphragm and the upper limit is formed by the manubrium in front, the first ribs laterally, and the spine posteriorly. It contains the main organs relative to respiration and circulation including lung, trachea, bronchia, heart, aorta, superior vena cava, inferior vena cava, and so forth, which nearly control human life. The thoracic diseases including lung cancer, thymus neoplasm, cardiac surgery disease, aortic aneurysm, and mediastinal tumor of nervous tissue are prevalent. If the cardiovascular and thoracic surgeons cannot master the anatomy of human thoracic structures, they may injure thoracic structures such as pulmonary lobe, pericardium, aorta, esophagus, trachea, bronchia, and vagus nerve during operation, leading to pneumothorax, hemothorax, vagus nerve injury, or many other unwanted sever

consequences. Previous anatomical data of lung and mediastinum including clinical image examinations are mostly two-dimensional (2D) images such as CT, CTA, MRI, MRA, and anatomical atlas, obviously, but 2D data cannot fully and faithfully reveal the three-dimensional (3D), full-scale information of the thoracic organs, and sometimes ambiguous conclusions may be reached. This kind of situation cannot efficiently meet the clinical requirement [1–4].

In recent years, theoretical and applied anatomical studies have been carried out on the basis of the American Visible Human Project (VHP) data sets, and visible human models have also been playing an important role in surgical teaching and clinical practice [5–11]. At present, there are several data sets of adult Chinese men and women in China, which lay the foundation for the research on the visible thoracic structures of Chinese people; so far the report of detailed 3D visible thoracic structures' model including lung and mediastinal structures is still not described. So in our study, a 3D visible

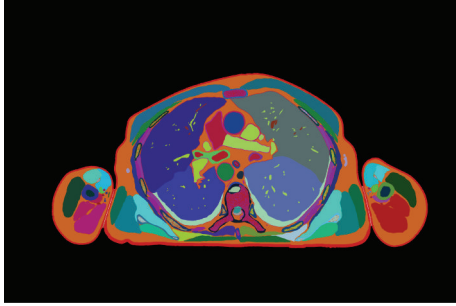


FIGURE 1: Segmentative image of CVH thorax.

model of the thoracic structure was established using CVH-1 data set. The study aims to help medical students and surgeons to master the complicated thoracic structures and to provide a basis for building dynamic thoracic structure and performing virtual cardiovascular and thoracic operations.

2. Materials and Methods

2.1. Retrieval of Sectional Anatomical Images of Thoracic Structures. The serial cross-sectional images of thoracic structures were prepared by using the first Chinese visible human (CVH-1) data sets. The cadaver of CVH-1 is a middle-aged, middle-sized, well-developed cadaver (sex: male; age: 35 years old; body height: 1,700 mm; body weight: 65.0 kg) without organic lesions and has been enrolled into the cadaver donation program. Both donor and his relatives will donate his body to the visible human program, which follows scientific ethic rules of Third Military Medical University and Chinese Ethics Department.

Successive cross-sectional images from the neck (1400) to the upper abdomen (1700) were retrieved from CVH-1 data set. The slice was 1.0 mm thick, and the cross-sections were photographed by digital camera (Canon, made in Japan) at a high-resolution of 6,291, 456 (3,072 × 2,048) pixels [1]. Every cross-section can successively and fully reveal the thoracic organs such as lung, heart, aorta, and so forth. There are 301 slices which we used in our study.

2.2. Segmentation on 2D Images. After registration through four reserved fiducial rods, segmentation was used to outline the thoracic structures on the 2D images with Photoshop 8.0 software (interface is shown in Figure 1). During segmentation, lung, heart, aorta and its ramus, trachea, bronchia, azygos vein, superior vena cava, inferior vena cava, thymus, esophagus, diaphragm, phrenic nerve, vagus nerve, sympathetic trunk, thoracic vertebrae, sternum, and thoracic duct were outlined on 2D sections with magnetic lasso tool. Then each structure was established as a layer and was filled with different RGB colors. Each image layer of segmental anatomical structure was assigned an anatomical name and the files were saved as PSD format. As to some structures such as phrenic nerve, vagus nerve, and sympathetic trunk which were difficult to distinguish where nervous tissue and the adjacent connective tissue mix, contour lines were extracted in some slices where nervous tissue can be observed.

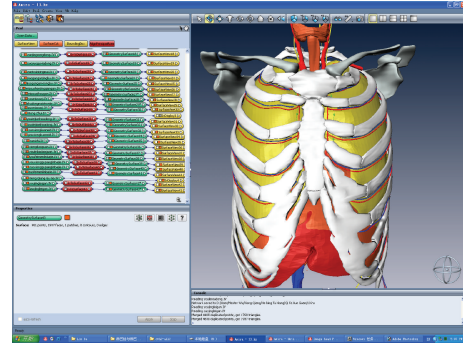


FIGURE 2: Amira software's interface.

2.3. Three-Dimensional Reconstruction and Visualization. After segmentation, the segmented structures were surface rendering reconstructed with Amira 5.2 software (interface is shown in Figure 2). Surface rendering is outlining the contour of the anatomical structures from 2D images and forming 3D surface with triangle grid. As to nervous tissue, interpolation was used in some slices where the nervous tissue cannot be observed clearly, which can be helpful to form consecutive tissue structures. The 3D reconstructed model of nervous tissue was imported to MAYA software and 3D reconstructed to smooth NURBS model.

2.4. Combining Surface Rendering and Volume Rendering Reconstruction. Preserving 3D surface rendering reconstructed model of thoracic organs, above 301 serial transverse cross-sectional images of thoracic structures from CVH-1 data set were imported to Amira software and three-dimensional reconstructed via volume rendering. The 3D reconstructed surface and volume rendering model of thoracic structures were observed clearly and directly using the orthoslice and oblique slice features of the software.

3. Results

3.1. A Three-Dimensional Model Established by Using Amira Software. The thorax model including lung, heart, aorta and its ramus, azygos vein, superior vena cava, inferior vena cava, trachea, bronchia, thymus, esophagus, diaphragm, phrenic nerve, vagus nerve, sympathetic trunk, thoracic vertebrae, sternum, and thoracic duct, which can represent Asia population, was 3D surface-rendering and volume-rendering reconstructed by using Amira software and presented no data loss. The resolution of the cross-section images reached up to 6.3×10^6 pixels. The serial digital images allowed a unique anatomical insight into the thoracic cavity, showing preferably the subtle anatomical structures of thorax. The three-dimensional model can be displayed partially or as a whole or with some structures being transparent and can be observed from any orientation, angle, or position of view. The reconstructed three-dimensional images can demonstrate two-dimensional sectional anatomical structure, which can provide the correct anatomical information, measure the volume and surface area of any reconstructed structure, and also simulate thoracic anatomy from any plane.

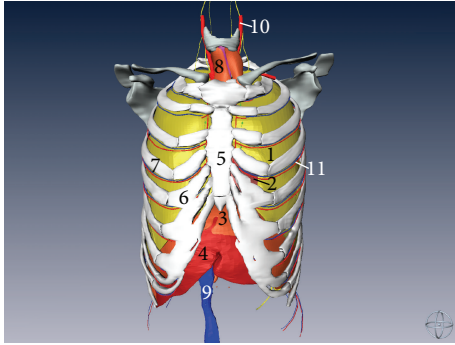


FIGURE 3: Three-dimensional surface rendering reconstructed model of thoracic structures with thoracic cage (anterior aspect) (1) left lung, (2) heart, (3) diaphragm, (4) liver, (5) sternum, (6) costal cartilage, (7) costal bone, (8) thymus, (9) inferior vena cava, (10) common carotid artery, and (11) intercostal artery and vein.

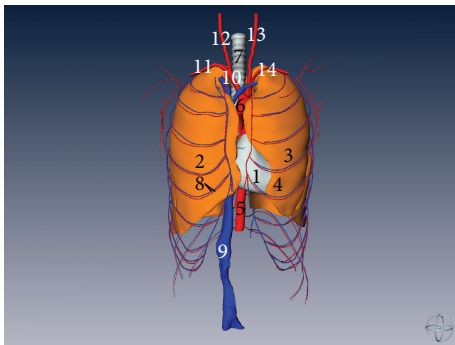


FIGURE 4: Three-dimensional reconstructed model of thoracic structures without thoracic cage (anterior aspect) (1) heart, (2) right lung, (3) left lung, (4) lingula of left lung, (5) abdominal aorta, (6) aorta arch, (7) trachea, (8) intercostal artery and vein, (9) inferior vena cava, (10) brachiocephalic trunk, (11) right subclavian artery, (12) right common carotid artery, (13) left common carotid artery, and (14) left subclavian artery.

Two lungs are nearly embedded by bony thoracic cage. The apex of both lungs is a little above the clavicle and the base of lung is concave. The lingular of left lung is in front of the left border of the heart. The heart is located in the middle mediastinum of the thorax and rest upon the diaphragm. Nearly two-third of the heart lies on the left of the median sagittal plane and the whole heart is nearly embedded by the thoracic cage but that only some part of the heart can show in the intercostal space (as shown in Figures 3 and 4).

All segmental bronchi of two lungs are 3D reconstructed and detailed relationship of lobar bronchi and segmental bronchi can be observed and the ramus of pulmonary artery and vein accompany corresponding bronchi (as shown in Figures 5 and 6).

Right lung is divided into superior, middle, and inferior lobe by a horizontal fissure and an oblique fissure of right lung. Apical, posterior, and anterior segmental bronchus (BI + BII + BIII) enter superior lobe, and lateral and medial segmental bronchus (BIV + BV) enter middle lobe, superior (it cannot be observed clearly because of organs wrapping),

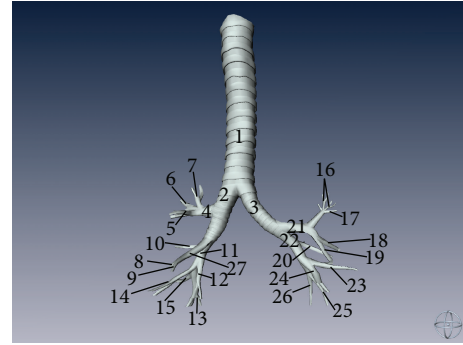


FIGURE 5: Three-dimensional model of trachea and bronchi (anterior aspect). (1) Trachea, (2) left bronchi, (3) right bronchi, (4) right superior lobar bronchus, (5) anterior segmental bronchus (BIII) (right lung), (6) posterior segmental bronchus (BII) (right lung), (7) apical segmental bronchus (BI) (right lung), (8) lateral segmental bronchus (BIV) (right lung), (9) medial segmental bronchus (BV) (right lung), (10) superior segmental bronchus (BVI) (right lung), (11) right inferior lobar bronchus, (12) medial basal segmental bronchus (BVII) (right lung), (13) posterior basal segmental bronchus (BX) (right lung), (14) anterior basal segmental bronchus (BVIII) (right lung), (15) lateral basal segmental bronchus (BIX) (right lung), (16) apicoposterior segmental bronchus (BI+BII) (left lung), (17) anterior segmental bronchus (BIII) (left lung), (18) superior lingular bronchus (BIV) (left lung), (19) inferior lingular bronchus (BV) (left lung), (20) superior segmental bronchus (BVI) (left lung), (21) left superior lobar bronchus, (22) left inferior lobar bronchus, (23) anterior basal segmental bronchus (BVIII) (left lung), (24) medial basal segmental bronchus (BVII) (left lung), (25) lateral basal segmental bronchus (BIX) (left lung), (26) posterior basal segmental bronchus (BX) (left lung), and (27) right middle lobar bronchus.

medial basal, anterior basal, lateral basal, and posterior basal segmental bronchus (BVI + BVII + BVIII + BIX + BX) enter inferior lobe (As shown in Figure 7).

Left lung is divided into superior and inferior lobe by an oblique fissure of left lung. Apical, posterior, anterior, superior lingular, and inferior lingular segmental bronchus (BI+BII+BIII +BIV+BV) enter superior lobe, and superior (it cannot be observed clearly because of organs wrapping), medial basal, anterior basal, lateral basal, and posterior basal segmental bronchus (BVI + BVII + BVIII + BIX + BX) enter inferior lobe (As shown in Figure 8).

After left lung is hidden, the apex of the heart, left auricle of the heart, and the root of left lung can be seen. Among the triangle of ductus arteriosus, which is made up of left vagus nerve, left phrenic nerve, and superior border of pulmonary artery, arterial ligament can be observed clearly. Thymus is located in anterior mediastinum, which is between sternum and pericardium. Esophagus is right and anterior to thoracic aorta. Sympathetic trunk is in front of and close to the transverse process of the thoracic vertebra. Hemiazygos and accessory hemiazygos are located in the anterior and left surface of the thoracic vertebrae and receive many posterior intercostal veins. Left vagus nerve descends between left common carotid and left subclavian arteries, crosses in front of

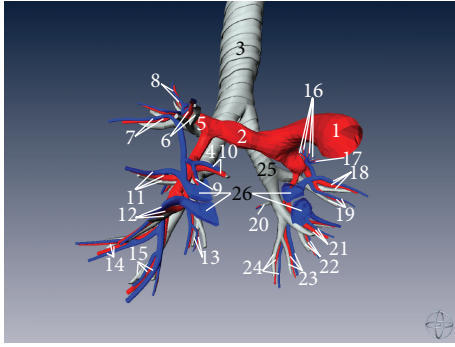


FIGURE 6: Three-dimensional model of trachea, bronchial tree, pulmonary artery and its ramus, and pulmonary vein and its ramus (anterior aspect). (1) Pulmonary artery, (2) right pulmonary artery, (3) trachea, (4) right bronchi, (5) superior lobar branches of right pulmonary artery, (6) anterior segmental bronchus (BIII) and its corresponding branch of pulmonary artery and vein (right lung), (7) posterior segmental bronchus (BII) and its corresponding branch of pulmonary artery and vein (right lung), (8) apical segmental bronchus (BI) and its corresponding branch of pulmonary artery and vein (right lung), (9) lateral segmental bronchus (BIV) and its corresponding branch of pulmonary artery and vein (right lung), (10) medial segmental bronchus (BV) and its corresponding branch of pulmonary artery and vein (right lung), (11) superior segmental bronchus (BVI) and its corresponding branch of pulmonary artery and vein (right lung), (12) anterior basal segmental bronchus (BVIII) and its corresponding branch of pulmonary artery and vein (right lung), (13) medial basal segmental bronchus (BVII) and its corresponding branch of pulmonary artery and vein (right lung), (14) lateral basal segmental bronchus (BIX) and its corresponding branch of pulmonary artery and vein (right lung), (15) posterior basal segmental bronchus (BX) and its corresponding branch of pulmonary artery and vein (right lung), (16) apicoposterior segmental bronchus (BI + BII) and its corresponding branch of pulmonary artery and vein (right lung), (17) anterior segmental bronchus (BIII) and its corresponding branch of pulmonary artery and vein (left lung), (18) superior lingular bronchus (BIV) and its corresponding branch of pulmonary artery and vein (left lung), (19) inferior lingular bronchus (BV) and its corresponding branch of pulmonary artery and vein (left lung), (20) superior segmental bronchus (BVI) and its corresponding branch of pulmonary artery and vein (left lung), (21) anterior basal segmental bronchus (BVIII) and its corresponding branch of pulmonary artery and vein (left lung), (22) medial basal segmental bronchus (BVII) and its corresponding branch of pulmonary artery and vein (left lung), (23) lateral basal segmental bronchus (BIX) and its corresponding branch of pulmonary artery and vein (left lung), and (24) posterior basal segmental bronchus (BX) and its corresponding branch of pulmonary artery and vein (left lung).

the aortic arch, passes behind the root of left lung, and reaches the anterior side of esophagus (as shown in Figure 9).

From the right view and posterior view of mediastinum, the heart, superior vena, inferior vena cava, and lung root of right lung can be observed clearly. At the upper part of thorax, esophagus is located between the trachea and thoracic vertebrae and deviates to the left. At the level of tracheal bifurcation, the esophagus lies posterior to trachea and anterior and left to the azygos vein. At the lower part of thorax (at the level of 8th to 9th thoracic vertebrae), the esophagus

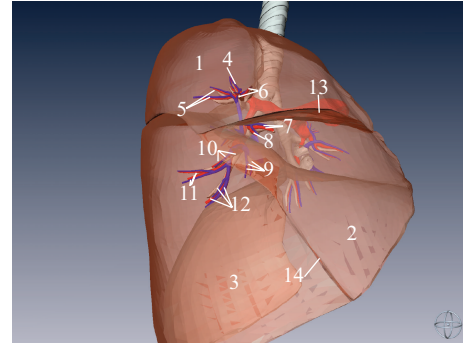


FIGURE 7: Three-dimensional model of right lung and its corresponding bronchial tree, pulmonary artery, pulmonary vein (right aspect). (1) Superior lobe of right lung, (2) middle lobe of right lung, (3) inferior lobe of right lung, (4) apical segmental bronchus (BI) and its corresponding branch of pulmonary artery and vein (right lung), (5) posterior segmental bronchus (BII) and its corresponding branch of pulmonary artery and vein (right lung), (6) anterior segmental bronchus (BIII) and its corresponding branch of pulmonary artery and vein (right lung), (7) medial segmental bronchus (BV) and its corresponding branch of pulmonary artery and vein (right lung), (8) lateral segmental bronchus (BIV) and its corresponding branch of pulmonary artery and vein (right lung), (9) medial basal segmental bronchus (BVII) and its corresponding branch of pulmonary artery and vein (right lung), (10) anterior basal segmental bronchus (BVIII) and its corresponding branch of pulmonary artery and vein (right lung), (11) lateral basal segmental bronchus (BIX) and its corresponding branch of pulmonary artery and vein (right lung), (12) posterior basal segmental bronchus (BX) and its corresponding branch of pulmonary artery and vein (right lung), (13) horizontal fissure of right lung, and (14) oblique fissure.

inclines to the left in front of the thoracic aorta. Thoracic duct ascends between the thoracic aorta and the azygos vein and then posterior to the esophagus. At the level of 4th thoracic vertebrae, it passes obliquely behind the esophagus to reach its left side. Right vagus nerve descends along the right side of the trachea, then passes behind the root of right lung, and reaches the posterior side of esophagus (as shown in Figures 10 and 11).

4. Discussion

4.1. Significance of CVH Male Data Set. Since visible three-dimensional reconstruction is based on two-dimensional images, the quality of original data provided by two-dimensional images is correlated to the fidelity of the reconstructed three-dimensional images. This CVH-1 data set can represent normal Asia-population thoracic anatomy and was more representative than the American VHP data set in terms of anatomical structures [12, 13]. Since most of structures in thorax are parenchyma, it is difficult to set up an archetypal male thorax model through CT, MRI, and ultrasound. However, on the high-resolution CVH 2D cross-sections, normal structures of the pericardium, bronchia, thymus, nervous tissue, and so forth can be displayed distinctly. Moreover, through artery perfusion with 20% red gelatin and the body frozen at -25°C , the CVH male project achieved greater integrity of images and easier blood vessel identification and

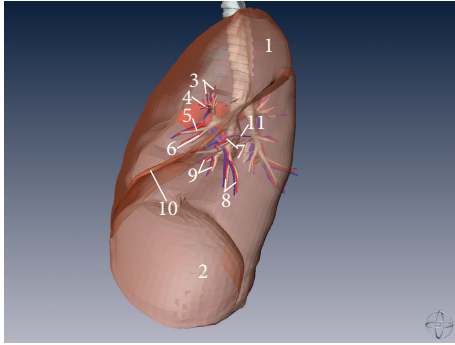


FIGURE 8: Three-dimensional model of left lung and its corresponding bronchial tree, pulmonary artery, and pulmonary vein (left aspect). (1) Superior lobe of left lung, (2) inferior lobe of left lung, (3) apicoposterior segmental bronchus (BI + BII) and its corresponding branch of pulmonary artery and vein (left lung), (4) anterior segmental bronchus (BIII) and its corresponding branch of pulmonary artery and vein (left lung), (5) superior lingular bronchus (BIV) and its corresponding branch of pulmonary artery and vein (left lung), (6) inferior lingular bronchus (BV) and its corresponding branch of pulmonary artery and vein (left lung), (7) anterior basal segmental bronchus (BVIII) and its corresponding branch of pulmonary artery and vein (left lung), (8) lateral basal segmental bronchus (BIX) and its corresponding branch of pulmonary artery and vein (left lung), (9) posterior basal segmental bronchus (BX) and its corresponding branch of pulmonary artery and vein (left lung), (10) oblique fissure, and (11) superior segmental bronchus (BVI) and its corresponding branch of pulmonary artery and vein (left lung).

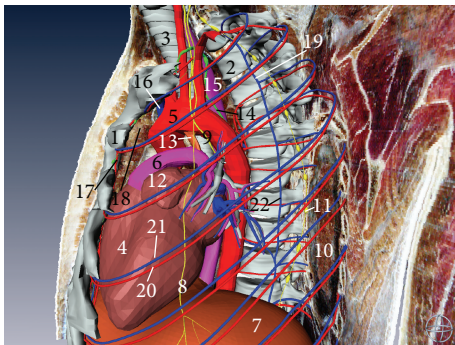


FIGURE 9: Three-dimensional model of mediastinal organs (left aspect). (1) Sternum, (2) thoracic vertebrae, (3) trachea, (4) heart, (5) aorta, (6) pulmonary artery, (7) diaphragm, (8) phrenic nerve, (9) vagus nerve, (10) left lung, (11) sympathetic trunk, (12) left auricle of the heart, (13) arterial ligament, (14) thoracic duct, (15) esophagus, (16) superior vena cava, (17) parasternal lymph nodes, (18) thymus, (19) accessory hemiazygos vein, (20) posterior intercostal artery, (21) posterior intercostal vein, and (22) hemiazygos vein.

were free of organic lesion (unlike the other visible human projects).

4.2. Three-Dimensional Reconstruction of Thorax. After registered and segmented with Photoshop 7.0 software, the sectional images of the data set of anatomical structures in thorax were 3D reconstructed via surface rendering based on marching cubes algorithm and volume rendering with

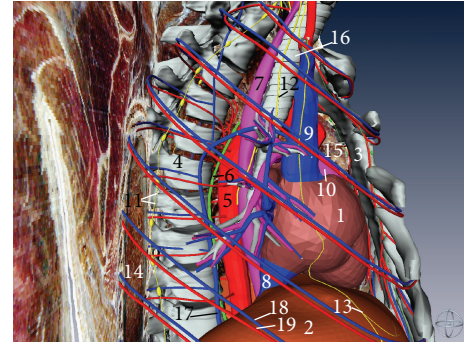


FIGURE 10: Three-dimensional model of mediastinal organs (right aspect). (1) Heart, (2) diaphragm, (3) sternum, (4) thoracic vertebrae, (5) thoracic aorta, (6) thoracic duct, (7) esophagus, (8) inferior vena cava, (9) superior vena cava, (10) pulmonary artery, (11) sympathetic trunk, (12) right vagus nerve, (13) phrenic nerve, (14) right lung, (15) thymus, (16) trachea, (17) azygos vein, (18) posterior intercostal vein, and (19) posterior intercostal artery.

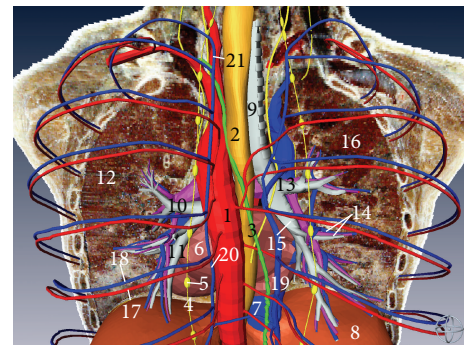


FIGURE 11: Three-dimensional model of mediastinal organs (posterior aspect). (1) Thoracic aorta, (2) esophagus, (3) thoracic duct, (4) sympathetic trunk, (5) ganglia of sympathetic trunk, (6) heart, (7) inferior vena cava, (8) diaphragm, (9) trachea, (10) left superior lobar bronchus, (11) left inferior lobar bronchus, (12) left lung, (13) right superior lobar bronchus, (14) right middle lobar bronchus and its corresponding ramus of pulmonary artery and vein, (15) right inferior lobar bronchus, (16) right lung, (17) posterior intercostal artery, (18) posterior intercostal vein, (19) azygos vein, (20) hemiazygos vein, and (21) accessory hemiazygos vein.

Amira software. With surface rendering, structures can be freely visualized and displayed in three-dimensional space on personal computer partially or as a whole or with some of the structures being transparent. Surface rendering reconstruction needs only organic contour data, so it can save much disc space and can run faster than volume reconstruction. Using voxel as the basic modeling unit, volume rendering can show the rich internal details of object, which has become the preferred method of 3D medical visualization.

Volume rendering reconstruction can preserve the information of the original images and overcome the defects of the surface rendering (lacking internal anatomical information). The image of the volume rendering is of high quality, but the quantity of operation is too much and the computation cost of visualization is very high.

Combining surface rendering and volume rendering reconstruction, thoracic structures can be displayed clearly and truly. Comparing with surface rendering reconstruction or volume rendering reconstruction solely, this method can overcome above defects.

4.3. Significance of Establishment of Human Thorax Models.

Many scientists 3D reconstructed tracheal tree, pulmonary artery, and pulmonary tree using CTA\MRA images [14–18], while there is still no study reporting reconstruct of mediastinal parenchyma such as thymus, thoracic duct, lymph nodes, zygus vein, phrenic nerve, vagus nerve, and sympathetic nerve. Our 3D thorax model can provide detailed 3D reconstructed model of lung and mediastinal structures.

To familiarize and master the anatomy of lung and mediastinum and their relationship is critical to improve thoracic and cardiovascular surgical techniques and to increase the success rate of thoracic surgery. Mediastinum contains so many important structures such as heart, aorta and its ramus, azygos vein, superior vena cava, inferior vena cava, thymus, esophagus, diaphragm, phrenic nerve, vagus nerve, and sympathetic trunk, and the relationship of the thoracic structures is difficult and it is hard to touch. Prior to a thoracic surgery, combing with pathological information, surgeon can know the size and location of the thoracic lesion and its spatial relations to its surrounding structures, so as to design an individualized surgical plan. Otherwise, the accuracy of the plan of a thoracic surgery will be decreased greatly and it may lead to pneumothorax, hemothorax, nerve, or thoracic duct injury. This three-dimensional reconstructed model of thoracic structures combining surface rendering with volume rendering can provide detailed and average information of Asian thorax. It can cut from any angle or any direction and display any sectional image including orthoslice and oblique slice.

Traditional anatomical study of thorax includes cadaver dissection and reading two-dimensional sectional images such as X-ray, CT, MRI, and anatomical atlas. In cadaver dissection, the anatomical structures and situation of some slim vessels and nerves in thorax are liable to be destroyed; moreover donated cadavers used in anatomical practice are scarce and limited. Two-dimensional images such as X-ray, CT, MRI, and anatomical atlas cannot 3D display the anatomical structures in the thorax, so medical students need more time to understand the anatomy of thorax. This 3D reconstructed anatomical model of thorax can provide detailed and integrated 3D anatomy in thorax for medical students learning gross anatomy and sectional anatomy [1, 2]. Detailed 3D anatomy may be observed from any direction or any angle. Medical students can dissect virtual thorax freely at any cut plane and can make any 3D reconstructed structures transparent, so it is helpful to observe its internal structure in a personal computer.

4.4. *VR of Thorax.* Virtual reality (VR) surgical simulation increasingly appears to be a promising aspect of the clinical anatomical education. The 3D reconstructed model of thoracic structures is a framework for simulating thoracic operation, thoracic radiotherapy, thoracoscopy and

mediastinoscopy operation, and thoracic surgery rehearsal [19]. Junior surgeon can manipulate VR program of thorax to deeply master the detailed anatomy of thorax and thoracic surgical basic skills. For example, thoracoscopy and mediastinoscopy can be facilitated greatly by preclinical operation training by using a model-based simulation. In radical lobectomy or mediastinal tumour dissection, tumors should be identified and dissected, and adjacent normal structures are important and needed and should be carefully protected to some extent. Thoracic surgery rehearsal model based on this 3D reconstructed model will help thoracic and cardiovascular rehearse operation in virtual thorax, which is helpful to maximal tumor tissue dissection and to minimize operational trauma [20].

4.5. *Some Problems.* The 3D reconstructed models based on CVH data set can provide detailed thoracic anatomy and have a broad range of potential applications for modern medical diagnosis and therapy for thoracic diseases [21]. Nevertheless, lung and heart have their own movements, and the 3D geometric anatomic shapes are only initialized basement of constructing dynamic model of thorax and virtual reality. A huge amount of work still has to be done. The ultimate goal of our study is to produce a virtual dynamic photorealistic human model which has physical and even physiological function.

Authors' Contribution

Yi Wu and Na Luo contributed equally to this work.

Conflict of Interests

The authors have no conflict of interests to declare in regard to this research work.

Acknowledgment

The authors greatly thank the National Science Foundation of China (nos. 81100480 and 61190122) (<http://www.nsf.gov.cn/>) for its financial support to this research work.

References

- [1] S. X. Zhang, P. A. Heng, Z. J. Liu et al., "Creation of the Chinese visible human data set," *The Anatomical Record B*, vol. 275, no. 1, pp. 190–195, 2003.
- [2] S. X. Zhang, P. A. Heng, Z. J. Liu et al., "The Chinese Visible Human (CVH) datasets incorporate technical and imaging advances on earlier digital humans," *Journal of Anatomy*, vol. 204, part 3, pp. 165–173, 2004.
- [3] Y. Wu, L. W. Tan, Y. Li et al., "Creation of a female and male segmentation dataset based on Chinese Visible Human (CVH)," *Computerized Medical Imaging and Graphics*, vol. 36, no. 4, pp. 336–342, 2012.
- [4] Y. Wu, S. X. Zhang, N. Luo et al., "Creation of the digital three-dimensional model of the prostate and its adjacent structures based on Chinese visible human," *Surgical and Radiologic Anatomy*, vol. 32, no. 7, pp. 629–635, 2010.

- [5] V. M. Spitzer, "The visible human: a new language for communication in health care education," *Caduceus*, vol. 13, no. 2, pp. 42–48, 1997.
- [6] K. V. Slavin, "The Visible Human Project," *Surgical Neurology*, vol. 48, no. 6, pp. 638–639, 1997.
- [7] M. J. Ackerman, "The Visible Human Project: a resource for education," *Academic Medicine*, vol. 74, no. 6, pp. 667–670, 1999.
- [8] M. J. Ackerman, "The Visible Human Project: a resource for anatomical visualization," *Studies in Health Technology and Informatics*, vol. 52, part 2, pp. 1030–1032, 1998.
- [9] T. Markestad, "Bruk av datasettet "The Visible Human Project" i forskning," *Tidsskrift for den Norske Laegeforening*, vol. 129, no. 6, pp. 529–530, 2009.
- [10] J. C. Deutsch, "Applications of the Colorado Visible Human Project in gastroenterology," *Clinical Anatomy*, vol. 19, no. 3, pp. 254–257, 2006.
- [11] M. M. Aldur, "Creating computer aided 3D model of spleen and kidney based on Visible Human Project," *Saudi Medical Journal*, vol. 26, no. 1, pp. 51–56, 2005.
- [12] S. Lei, L. Hu-jian, and J. Xun, "Comparison of constitution indexes of Han male youth recruited from different areas," *Chinese Journal of Public Health*, vol. 25, 017, no. 2, pp. 157–160, 2009.
- [13] X. G. Yang, Y. P. Li, G. S. Ma et al., "Study on weight and height of the Chinese people and the differences between 1992 and 2002," *Zhonghua Liuxingbingxue Zazhi*, vol. 26, no. 7, pp. 489–493, 2005.
- [14] P. M. Boiselle, K. F. Reynolds, and A. Ernst, "Multiplanar and three-dimensional imaging of the central airways with multi-detector CT," *American Journal of Roentgenology*, vol. 179, no. 2, pp. 301–308, 2002.
- [15] N. C. Dalrymple, S. R. Prasad, M. W. Freckleton, and K. N. Chintapalli, "Informatics in radiology (infoRAD): introduction to the language of three-dimensional imaging with multidetector CT," *Radiographics*, vol. 25, no. 5, pp. 1409–1428, 2005.
- [16] K. M. Horton, M. R. Horton, and E. K. Fishman, "Advanced visualization of airways with 64-MDCT: 3D mapping and virtual bronchoscopy," *American Journal of Roentgenology*, vol. 189, no. 6, pp. 1387–1396, 2007.
- [17] J. G. Ravenel, H. P. McAdams, M. Remy-Jardin, and J. Remy, "Multidimensional imaging of the thorax: practical applications," *Journal of Thoracic Imaging*, vol. 16, no. 4, pp. 269–281, 2001.
- [18] X. Zhao, Y. Ju, C. Liu et al., "Bronchial anatomy of left lung: a study of multi-detector row CT," *Surgical and Radiologic Anatomy*, vol. 31, no. 2, pp. 85–91, 2009.
- [19] Y. Morita, K. Takase, T. Yamada et al., "Virtual CT thoracoscopy: preoperative simulation for thoracoscopic surgery of esophageal cancer," *Abdominal Imaging*, vol. 32, no. 6, pp. 679–687, 2007.
- [20] R. C. Ward, M. W. Yambert, R. J. Toedte et al., "Creating a human phantom for the virtual human program," *Studies in Health Technology and Informatics*, vol. 70, pp. 368–374, 2000.
- [21] R. A. Robb, "Virtual endoscopy: development and evaluation using the Visible Human Datasets," *Computerized Medical Imaging and Graphics*, vol. 24, no. 3, pp. 133–151, 2000.

Research Article

L_p -Norm Regularization in Volumetric Imaging of Cardiac Current Sources

Azar Rahimi, Jingjia Xu, and Linwei Wang

Rochester Institute of Technology, Rochester, NY 14623, USA

Correspondence should be addressed to Azar Rahimi; azar.rahimi@mail.rit.edu

Received 13 September 2013; Revised 23 October 2013; Accepted 23 October 2013

Academic Editor: Heye Zhang

Copyright © 2013 Azar Rahimi et al. This is an open access article distributed under the Creative Commons Attribution License, which permits unrestricted use, distribution, and reproduction in any medium, provided the original work is properly cited.

Advances in computer vision have substantially improved our ability to analyze the structure and mechanics of the heart. In comparison, our ability to observe and analyze cardiac electrical activities is much limited. The progress to computationally reconstruct cardiac current sources from noninvasive voltage data sensed on the body surface has been hindered by the ill-posedness and the lack of a unique solution of the reconstruction problem. Common L_2 - and L_1 -norm regularizations tend to produce a solution that is either too diffused or too scattered to reflect the complex spatial structure of current source distribution in the heart. In this work, we propose a general regularization with L_p -norm ($1 < p < 2$) constraint to bridge the gap and balance between an overly smeared and overly focal solution in cardiac source reconstruction. In a set of phantom experiments, we demonstrate the superiority of the proposed L_p -norm method over its L_1 and L_2 counterparts in imaging cardiac current sources with increasing extents. Through computer-simulated and real-data experiments, we further demonstrate the feasibility of the proposed method in imaging the complex structure of excitation wavefront, as well as current sources distributed along the postinfarction scar border. This ability to preserve the spatial structure of source distribution is important for revealing the potential disruption to the normal heart excitation.

1. Introduction

Advances in medical imaging modalities have led to an explosion in the quantity and quality of cardiac data available for analysis. Together with the progress in computer vision, there has been a substantial improvement in our ability to assess the structure [1], the kinematics (such as the deformation) [2], and the mechanics (such as the strain distribution) [3] of the heart. Nevertheless, the heart is an electromechanically coupled organ. An efficient contraction of the heart must be preceded by a coordinated electrical current flow throughout the heart muscle. Otherwise a disrupted current flow will directly compromise the ability of the heart to contract and pump effectively. Unfortunately, there is a considerable inadequacy in our ability to observe and analyze the electrical activity and property of the heart.

Electrical currents in the heart, similar to those in the brain, work as bioelectric sources to produce bioelectromagnetic fields that can be sensed as small voltages in the volume conductor of the torso. This voltage change over time is measured on the body surface as electrocardiogram (ECG),

similar to the electroencephalogram (EEG) measured for the brain. Biophysical models of this bioelectrical field can be derived from the *quasistatic electromagnetism* [4] where, at any time instant, the m -dimensional ECG measurements \mathbf{b} are described as linear combination of the n -dimensional spatial distribution of current source \mathbf{v} : $\mathbf{b} = \mathbf{H}\mathbf{v}$. Note that the biophysical model between the current sources in the brain and the EEG signals can be derived from the same physical principle but on a different anatomical region (heart-torso versus brain-skull).

Because there is a lack of experimental techniques to physically measure cardiac electrical signals \mathbf{v} deep into the thickness of the myocardium, many computational strategies are developed which, analogous to *computed tomography*, aim to computationally *reconstruct* the three-dimensionally distributed, time-varying bioelectrical currents by solving the inverse problem on $\mathbf{b} = \mathbf{H}\mathbf{v}$, using noninvasive signals \mathbf{b} collected at different body-surface locations. However, solving this computational inverse problem is afflicted with two sources of challenges. First, this problem is ill-posed and underdetermined because of the limited number of field

measurements compared to the large degree of freedom in the unknowns (the possible location of current sources). Errors in the measurement data or the anatomical modeling (reflected in \mathbf{H}) could highly affect the stability of the solution. Second, even with *virtually* continuous measurements on the surface, this problem still suffers from the lack of a unique solution as determined by the underlying biophysics: different configurations of 3D source distributions may produce the same field measurements on the external surface [4]. Therefore, if the solution is sought transmurally, this inverse problem is intrinsically ill-posed without a unique solution in its most unconstrained form. Proper assumptions of the solutions must be made in order to guarantee a unique solution.

Even though the inverse problem of source reconstruction in the heart (using ECG) and in the brain (using EEG) essentially deals with the same physics problem, developments in the two fields have seen substantial difference in progress. In the latter, numerous approaches have been developed to estimate three-dimensionally distributed current sources [5–7]. In the former, on the contrary, the most commonly used approach is to restrain the solution on the epicardium [8] and/or endocardium [9], sacrificing the information into the depth of the myocardium in exchange for a unique solution. There are few successes in *imaging* the cardiac electrical sources deep into the myocardium, which often involve complex, physiological prior knowledge from computational electrical propagation models of the heart [11, 27]. The question is: *if the two inverse problems are essentially founded on the same physics, what is the obstacle that hinders the progress of cardiac source reconstruction towards a volumetric solution?* We hypothesize that this is, at least in part, caused by the unique spatial property of cardiac current sources. Neural current sources are often focal and compact, and the research focus is to find out which regions in the brain are activated at any given condition. For this purpose, the widely used minimum norm solution (minimum L_2 -norm) [5] was proved to be feasible to provide a solution with minimum overall energy that fits the measured EEG data. Though the solutions are often overly diffused/smoothed, the maximum magnitude in the solution still suffices to approximate the source location. Later, sparse methods such as minimum L_1 -norm [7] and p -norm ($p \leq 1$, realized through recursive weighting scheme) [6] were proposed to obtain sparse solutions that can more accurately pinpoint the location of focal sources.

In comparison, cardiac current source starts from a few focal sites but then propagates throughout the atrial and ventricular myocardium during the cardiac cycle. As a result, the structure of cardiac current sources undergoes a much more complex spatiotemporal change during the cardiac excitation, as illustrated by the two examples given in Figure 1. In a normal depolarization phase of the cardiac excitation, the current sources form an *excitation wavefront* between depolarized and resting cells (Figure 1(a)). After all the cells are depolarized, the heart goes through a stage without current flow (ST-segment in an ECG cycle). Afterwards, the repolarization phase starts and a similar *repolarization wavefront* can be observed to flow throughout the myocardium. In a

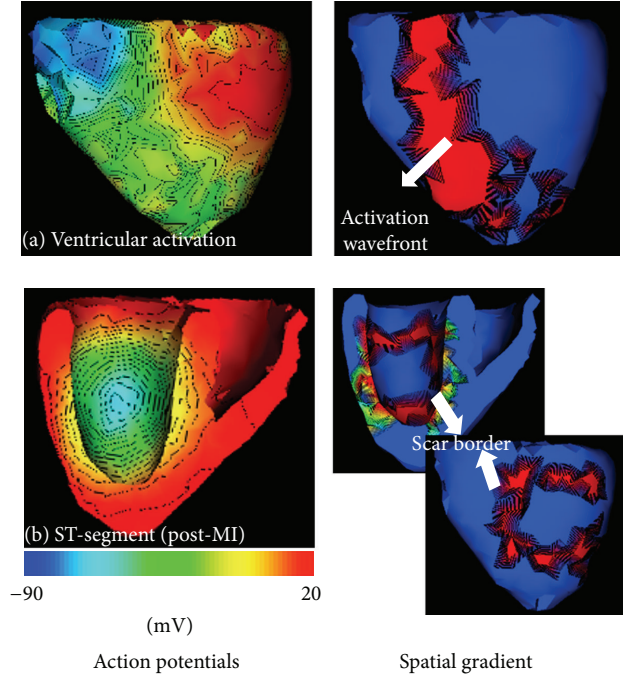


FIGURE 1: Illustration of the spatial structure of ventricular current sources during a healthy (a) or pathological (b) cardiac cycle.

diseased heart with an infarct, this normal excitation process will be disrupted. For example, during the ST-segment, there will be a voltage difference between healthy myocardium and the center of the infarct, and active current sources will be concentrated along the scar border (Figure 1(b)). This time-varying spatial structure of the current source is important because it reveals the potential disruption to a normal excitation of the heart.

This unique spatial property of cardiac current sources decides that L_2 or L_1 regularization will produce a solution that is either too smeared or too focal to reveal the underlying source distribution, even though they have been successful with a similar inverse problem in the brain. Based on this observation, we propose a general regularization with L_p -norm ($1 < p < 2$) constraint to cardiac source reconstruction. Balancing between a smeared and a focal solution, L_p -norm constraint bridges the gap between L_1 - and L_2 -norm regularizations. The nonlinear L_p -norm regularization is solved after being cast to second-order cone programming (SOCP) problem. In a set of phantom experiments, the proposed method is shown to outperform its L_1 and L_2 counterparts in imaging cardiac current sources with increasing extents. We further demonstrate the feasibility of the proposed method in imaging the complex structure of excitation wavefront during a normal propagation (Figure 1(a)), as well as that of the scar border during a ST-segment in an infarcted heart (Figure 1(b)). An initial real-data experiment also attests to its feasibility in detecting scar border in a postinfarction human subject.

2. Related Works

As mentioned earlier, the quasi-static electromagnetism governs the relation between cardiac current sources and body-surface voltage measurements. Employing proper numerical methods such as mesh-free and boundary element methods, this relationship can be rendered to $\mathbf{b} = \mathbf{H}\mathbf{v}$, where \mathbf{H} is built on a subject-specific heart-torso model in ECG source localization problem. To overcome the ill-posedness of the inverse problems on these bioelectric fields, proper regularization needs to be employed:

$$\min_{\mathbf{v}} \|\mathbf{b} - \mathbf{H}\mathbf{v}\|_2^2 + \lambda C(\mathbf{v}), \quad (1)$$

where the first term in the objective function describes the least square minimization of data-fitting error (data fidelity term) and the second term defines the regularization constraint. λ is the regularization parameter that controls the trade-off between fitting to the data and comforting to the constraint.

2.1. L2 Regularization: Smooth Constraints. The most common constraint used in (1) is $L2$ or weighted- $L2$ norm to enforce the smoothness of the source distribution: $C(\mathbf{v}) = \|\mathbf{F}\mathbf{v}\|_2^2$, where \mathbf{F} is usually defined as identity matrix, gradient operator, and Laplace operator for 0-order, 1-order, and 2-order regularization, respectively. In $L2$ -norm regularization, regularization parameter λ is typically determined using the generalized cross-validation, the discrepancy principle, and the L -curve method [12].

The mainstream approaches, addressing the inverse problem of ECG source localization on the heart surfaces, are mainly based on $L2$ -norm regularization using different spatial and/or temporal constraints. These methods include Tikhonov regularization method [8], least squares QR (LSQR) [13], truncated total least square (TTLS) [14], Kalman filter [15], generalized minimal residual [16], and level-set [17] and statistical approaches [18]. Although incorporating the $L2$ -norm-based constraint handles the ill-posedness of this inverse problem and provides stability in the presence of noise, it ultimately diffuses the source reconstruction solution. The smoothing nature of $L2$ regularization makes it infeasible to trace the complex spatial distribution of the cardiac current sources using the region with maximum energy (as shown in Section 4.2).

$L2$ -norm-based regularization was later extended to a 3D setting in order to *image* volumetric current sources in the heart [19, 20]. Employing a weighted $L2$ -norm regularization on the intramural solution, these methods successfully estimate the active sources during the initiation sites and activation sequence [19] and the ST segment of an ECG cycle [20]. Because of the simplicity of the constraint, these methods can only be utilized to recover the source activity during one stable period of cardiac excitation cycle where the source distribution does not go through notable temporal changes. To consider the complete temporal changes of the cardiac sources in a complete excitation cycle, more complex prior knowledge in terms of 3D intramural electrical excitation model of the heart was included in [11, 27]. $L2$ penalty is

then used to enforce the solution to be close to that predicted by the computer model. While being able to reconstruct the complete spatiotemporal changes of the current sources, this type of approaches is influenced by the prior knowledge produced by the excitation model; furthermore, due to the $L2$ -norm penalty, the solution only renders patternwise qualitative accuracy but loses quantitative accuracy in the distribution of 3D current sources [21].

2.2. L1 Regularization: Sparse Methods. The most popular approach to circumvent the smoothing effect of $L2$ -norm constraint is to employ $L1$ -norm penalty during regularization [22] $C(\mathbf{v}) = \|\mathbf{F}\mathbf{v}\|_1$, where \mathbf{F} is defined similar to that in the $L2$ -norm constraint. For this type of approaches, there is no established methods to objectively set the value of the regularization parameter λ , and common practice resorts to empirical methods depending on the dataset.

As explained earlier (Figure 1), cardiac current sources are often localized, but not focal, during the course of a cardiac cycle. Therefore, sparse methods are rarely considered in the ECG inverse problem. Recently, $L1$ regularization was introduced for the first time to improve the sharp features of the source reconstruction on the epicardium [23, 24]. While it has been shown to numerically improve the resolution of the solution, it is unknown if the sparsity assumption is tied to the physiological property of the epicardial equivalent source models. In another work, $L1$ -norm was extended to the data term in order to improve the solution in terms of outliers [25]. Most recently, we developed and demonstrated the efficacy of a Lp regularization ($p \leq 1$) based on recursive weighting scheme to successfully pinpoint the focal sources in the beginning of an electrical propagation cycle [26]. However, as explained earlier, such focal sparsity of cardiac current sources is quickly lost as the current flows throughout the heart muscle, and the same sparse method is no longer applied. The regularization method that imposes sparsity at the early stage of electrical excitation, therefore, must be able to adapt to this change of spatial property of the current sources for the rest of the cardiac cycle.

3. Methodology

Based on the quasi-static electromagnetism [4], the potential distribution within torso volume conductor is produced by the cardiac current sources according to

$$\sigma_{\text{blk}} \nabla^2 \phi_e(\mathbf{r}) = \nabla \cdot (-\mathbf{D}_{\text{int}} \mathbf{v}(\mathbf{r})), \quad \forall \mathbf{r} \in \Omega_h, \quad (2)$$

$$\sigma \nabla^2 \phi(\mathbf{r}) = 0, \quad \forall \mathbf{r} \in \Omega_{t/h}, \quad (3)$$

where the Poisson equation (2) describes, on a bidomain heart model, how the extracellular potential ϕ_e within the heart volume Ω_h originates from the current sources \mathbf{v} modulated by the anisotropic intracellular conductivity tensor \mathbf{D}_{int} . σ_{blk} is the bulk conductivity assumed to be isotropic. The Laplace equation (3) describes, on the monodomain torso model, how the potential ϕ distributes within the torso volume $\Omega_{t/h}$ external to the heart with conductivity σ .

We have previously shown that, using mesh-free and boundary element methods, we can numerically solve (2) and

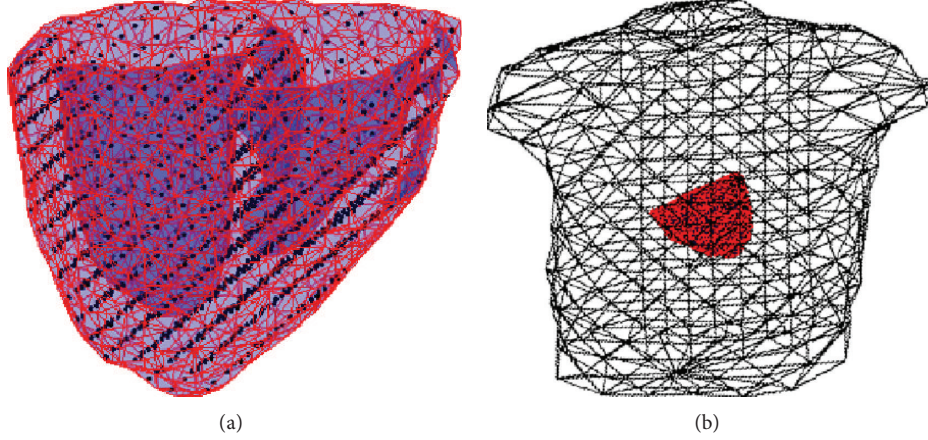


FIGURE 2: (a) Mesh-free nodes (black points) that represent the 3D myocardium. (b) Coupled heart-torso model.

(3) on a given heart-torso model of a subject (Figure 2) and obtain a linear relationship between ECG measurements (**b**) and the current sources (**v**): $\mathbf{b} = \mathbf{H}\mathbf{v}$ [10].

3.1. L_p -Norm Regularization. As mentioned earlier, reconstructing 3D current sources from ECG data is a highly ill-posed inverse problem with nonunique solutions in its most unconstrained form. However, complex spatial distribution of cardiac current sources conflicts with a focal $L1$ or smooth $L2$ constraint. To estimate the special structure of current sources, we apply L_p -norm regularization:

$$\min_{\mathbf{v}} \|\mathbf{b} - \mathbf{H}\mathbf{v}\|_2^2 + \lambda \|\mathbf{v}\|_p, \quad 1 < p < 2, \quad (4)$$

$$\|\mathbf{v}\|_p = \left(\sum_{i=1}^n [v_i]^p \right)^{1/p},$$

where n is the dimension of \mathbf{v} , that is, the number of mesh-free nodes used to represent the ventricular myocardium.

L_p -norm penalty term promotes different forms of structural sparsity as often observed in the heart. It offers the potential to outperform sparse $L1$ -norm and diffused $L2$ -norm for localizing sources with different extents/sizes.

3.2. p -Order Cones and Second-Order Cones Programming. Solving this L_p -norm regularization is not possible using linear or quadratic programming. Here we adopt SOCP that allows minimization of linear objective functions with quadratic cone constraints based on interior point methods. Furthermore, it provides flexibility to incorporate an arbitrary number of constraints while providing an efficient solution. To do so, we need to first reformulate our inverse problem (4) into a p -order cone programming (p -OCP) problem, which can be obtained by introducing two intermediate variables ξ, η into the objective function:

$$\min_{\xi, \eta} \xi + \lambda \eta \quad (5)$$

$$\text{s.t. } \|\mathbf{b} - \mathbf{H}\mathbf{v}\|_2^2 \leq \xi$$

$$\|\mathbf{v}\|_p \leq \eta.$$

Assuming p as a positive rational number ($p = r/s$), this p -OCP problem can then be transformed into a set of linear inequalities and 3D SOC constraints and be handled by SOCP methods [28]. In this way, the conic constraint $(v_1^p + \dots + v_n^p)^{1/p} \leq \eta$ is equivalent to

$$v_j^r \leq u_j^s t^{r-s}, \quad u_j \geq 0, \quad j = 1, \dots, n \quad (6)$$

$$t \geq \sum_{j=1}^n u_j.$$

Each constraint is then represented by a sequence of 3D rotated SOC constraints that can be expressed with inequalities of the form $z^2 \leq xy$.

4. Results

4.1. Imaging Current Sources with Various Extents. First, we consider synthetic experiments on a heart-torso model derived from a human subject as shown in Figure 2. The torso surface is represented by triangulated elements with 370 vertices. The ventricular myocardium is represented by total 1019 nodes distributed in a cubic grid with 7 mm intergrid distance and confined by the ventricular surface.

In the first set of experiments, we investigate the performance of L_p -norm regularization in localizing current sources with different sizes. In total, 44 settings are studied, considering a region of active current sources sized from 1% to 45% of the left ventricle. These sources form a region with structural sparsity located randomly inside the ventricular myocardium. The nodes lying within the region of active sources are assigned with values 1, while the rest of the ventricular nodes are set to be 0. For each setting, the corresponding ECG measurements are simulated on the 370 vertices on the body surface and are corrupted with white Gaussian noise before being input to the L_p -norm method to reconstruct the region of active current sources. The accuracy of 3D source estimation is evaluated using the *source overlap*

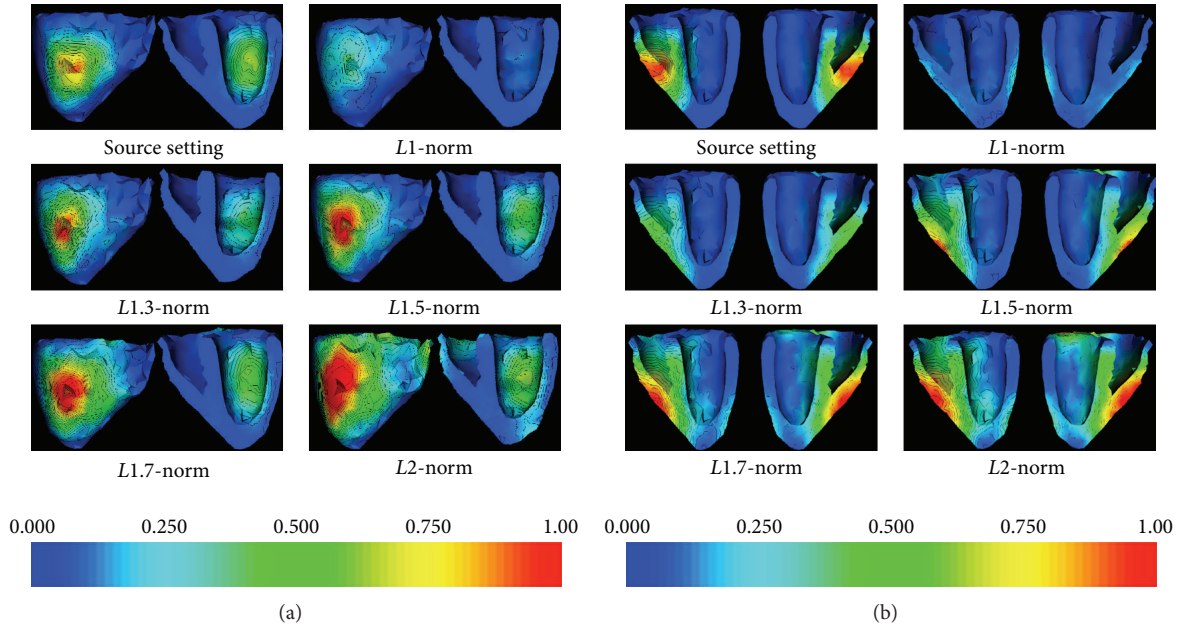


FIGURE 3: Source estimation using L_p -norm regularization for $1 \leq p \leq 2$. (a) 58 active sources are located at left ventricle mid-anterior. (b) 127 active sources are located close to the right ventricle apex. Increasing the p value increases the source extent such that $L1$ -norm obtains too scattered source distribution while $L2$ -norm provides overly diffused solution. Current magnitudes are normalized to 1.

(SO) defined as the intersection divided by the union between the estimated and the *true* region of current sources:

$$SO = \frac{\text{simulated sources} \cap \text{estimated sources}}{\text{simulated sources} \cup \text{estimated sources}}. \quad (7)$$

Setting p value to 1 and 2, we also perform $L1$ - and $L2$ -norm estimation of the 3D current source distribution and compare the results with the proposed L_p -norm method.

4.1.1. Values of p versus Source Extents. For every source setting, L_p -norm estimation is obtained using $p \in \{1.1, 1.3, 1.5, 1.7, 1.9\}$ and is compared to that obtained by $L1$ and $L2$ solutions. 30 dB noise is considered.

Figure 3(a) shows an example of source estimation using L_p -norm regularization for $1 \leq p \leq 2$, where the active region is located at mid-inferior of the left ventricle. The $L1$ -norm estimation of active sources results in a very sparse source reconstruction ($SO = 0.05$) scattered in the *true* region of active sources, and nearly no active sources were detected close to the endocardium. Increasing the p value for the L_p -norm regularization, the detected source extent increases. At $p = 1.3$, we obtain an accurate estimation of source extent ($SO = 0.38$), which is located very close to the *true* region of active sources. As p continues to increase, the estimated source region becomes more extended but still has a relatively compact center. There is a sudden change of pattern in the solution when p equals 2, where the estimated source region ($L2$ solution) becomes very diffused ($SO = 0.22$). Another example is presented in Figure 3(b), where the active current sources are located close to the right ventricle apex. Similar pattern can be observed in the source estimation by increasing the p value from 1 to 2.

Figure 4(a) summarizes the mean SO (vertical axis) between the *true* and estimated source regions obtained using

L_p -norm regularization, as p increases from 1 to 2 (horizontal axis 1) and as the size of active region increases (horizontal axis 2). As shown, for source regions of all sizes, similar trend of SO change can be observed as p increases from 1 to 2 in the L_p -norm regularization: the sparse solution produced by $L1$ -norm regularization, though produces low false-positives, also has a high underestimation (low numerator in the calculation of the OS) and therefore a low value of OS. On the other extreme, the smeared solution of $L2$ -norm regularization, though is able to detect the majority of the *true* active sources, tends to have a high overestimation (high denominator in the calculation of the OS) and thus leads to again a low OS value. Therefore, for source region of all sizes (as the 3 examples shown in Figures 4(b)–4(d)), we can observe an increase followed by a decrease of the OS value when p increases from 1 to 2, with the maximum OS obtained when $1.5 \leq p \leq 1.6$. Such benefits of the L_p -norm regularization with $1 < p < 2$ are particularly evident when the source region is of medium size ($\leq 30\%$ of the left ventricle).

4.1.2. Noise Effect on L_p -Norm Source Estimation. Next, we investigate the performance of our proposed L_p -norm regularization in presence of noise with different SNR levels (50–20 dB), using $p = 1.5$ as an example. Here we consider a region of size 1–52% of the left ventricle. As shown in Figure 5, increasing the noise level leads to minor decreasing of the OS value, and the trend of change is similar for sources of all sizes. The mean SO calculated for different source extents in presence of 50 dB noise is 0.35 and starts to decrease to 0.28, 0.25, and 0.2 as the SNR decreases to 40, 30, and 20, respectively. Again, the advantage of L_p regularization is more evident when the source is of medium size ($\sim 30\%$ of LV).

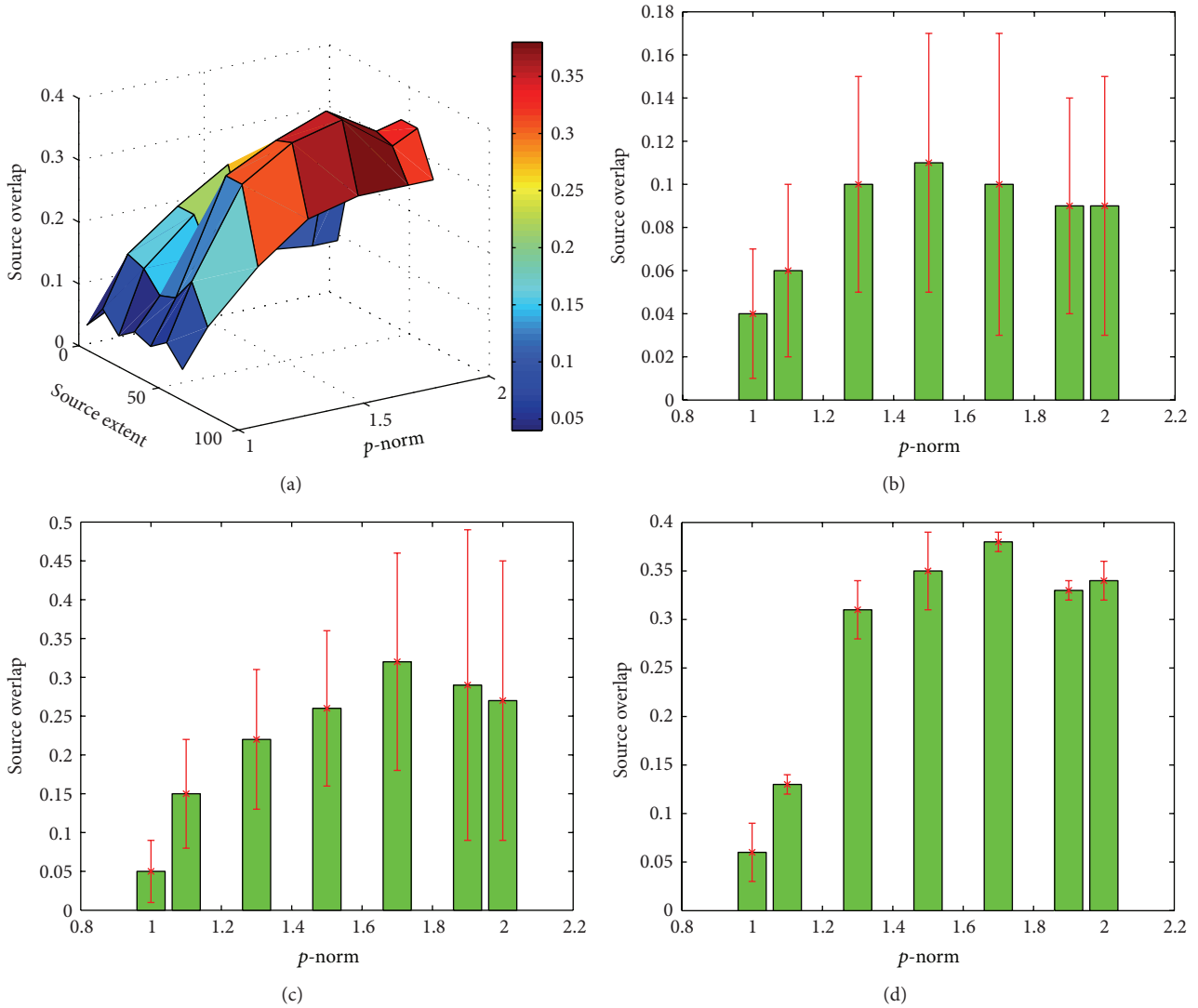


FIGURE 4: (a) Source overlap (SO, vertical axis) obtained by L_p -norm reconstruction ($1 \leq p \leq 2$, horizontal axis 1) for active sources with different extents (ranging from 1 to more than 80 active sources in the region, horizontal axis 2). (b)–(d) Examples of SO mean and standard deviation obtained by L_p -norm reconstruction ($1 \leq p \leq 2$) for a region of (b) 1–10, (c) 20–30, and (d) 40–50 active sources.

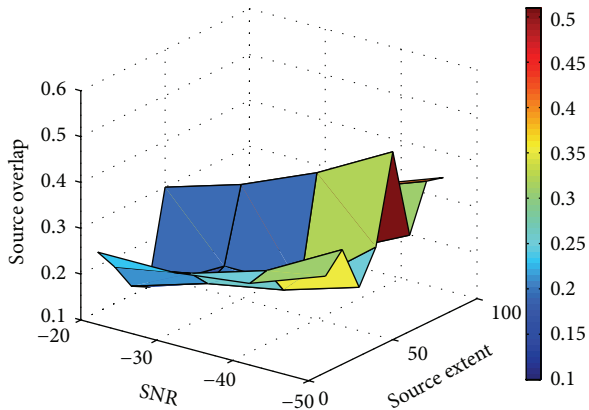


FIGURE 5: Source overlap (SO, vertical axis) obtained by L_p -norm reconstruction ($p = 1.5$) for active sources with different extents (horizontal axis 1) in presence of white Gaussian noise with different SNR levels (horizontal axis 2).

4.2. Computer-Simulated Electrical Activity. As explained earlier, one critical feature of cardiac current sources that differs from neural current sources is the complex spatial structure they exhibit during the cardiac cycle of electrical propagation, which is likely to be the cause of the difficulty of using L_1 or L_2 regularization for faithful reconstruction. In this set of experiments, we increase the complexity of the experimental settings and consider *realistic* structures of current sources, which are generated by computer simulations of the spatiotemporal propagation of electrical waves in the ventricles.

4.2.1. Imaging Excitation Wavefront. First, we consider the ability of the proposed L_p -norm regularization in reconstructing the complex structure of excitation wavefront. Figure 6(a) shows an example of an excitation wavefront during a normal propagation in a healthy ventricle at 33 ms

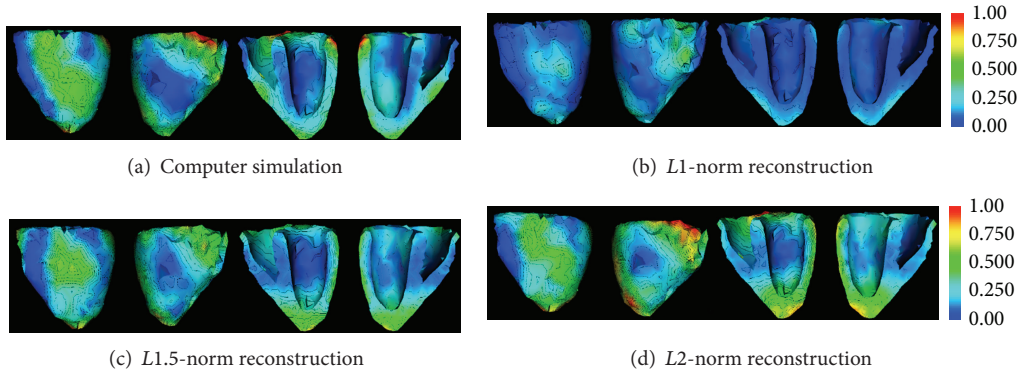


FIGURE 6: Excitation wavefront estimation using L_p -norm regularization versus L_1 - and L_2 -norm counterparts.

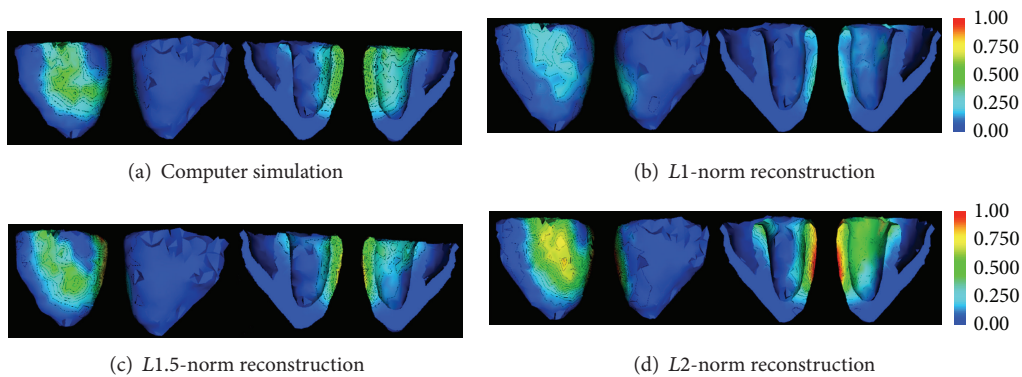


FIGURE 7: Estimation of current sources localized along the scar border using L_p -norm regularization versus L_1 - and L_2 -norm counterparts.

after the onset of ventricular excitation. Similar to our earlier observations, the L_1 reconstruction produces scattered solution where the spatial structure of the excitation wavefront is lost (Figure 6(b)). The L_2 reconstruction, on the other extreme, produces a blurred region of activation where the structure of excitation wavefront is smeared (Figure 6(d)). In comparison, the L_p reconstruction ($p = 1.5$) better preserves the excitation wavefront (Figure 6(c)). Quantitatively, the L_p regularization obtains $OS = 0.26$, while the L_1 solution provides $OS = 0.07$, and the L_2 solution produces $OS = 0.23$.

The ability to properly capture the spatial structure of the excitation wavefront, with a solution neither too scattered nor too diffused, is important because tracing the excitation wavefront can reveal the existence and location of obstacles that disrupt the normal propagation of electrical waves.

4.2.2. Imaging Source Localization along the Scar Border. Second, we examine the feasibility of the proposed method in estimating the current source activity along the scar border in an infarcted heart. As explained earlier, during the ST-segment of an ECG cycle, there is no current flow in a healthy heart. In an infarcted heart, in comparison, only the viable myocardium would exhibit coherent high voltage, while the necrotic tissue in the scar core will exhibit low voltage. These two regions will be separated by the scar border where the active current sources are localized.

Figure 7 shows an example of current source distributed along the border of an infarct that extends from basal to

mid-anterior and anterolateral LV. L_p regularization ($p = 1.5$) detects an active sources region consistent with the *true* scar border, reporting an $SO = 0.35$. In comparison, the L_1 regularization produces a scattered solution ($SO = 0.08$) and the L_2 regularization produces a diffused solution ($SO = 0.26$), neither of which is able to capture the structure topology of the current sources along the scar border. This ability of the proposed L_p reconstruction to faithfully reconstruct the current sources distributed along the scar border is of great importance because the scar border is known as the common site for triggered electrical activity and reentrant circuits that can initiate and maintain life-threatening ventricular arrhythmias.

4.3. Real-Data Experiments: Imaging Scar Border for a Postinfarction Patient. Because of the important therapeutic value of scar border, and the promising results obtained from our initial synthetic experiments, we continue to conduct an initial real-data experiment on a real post-infarction human subject to assess the feasibility of the proposed L_p -norm method in detecting current sources along the scar border.

Experimental data were collected from a patient with prior myocardial infarction and made available to this study by 2007 *PhysioNet/Computers in Cardiology Challenges* [29]. MRI scan of the patient has 8 mm interslice spacing and 1.33 mm/pixel in-plane resolution. Body surface ECG maps were recorded by *Dalhousie University* standards [30] at 123 known anatomical sites and interpolated to 370 nodes of the

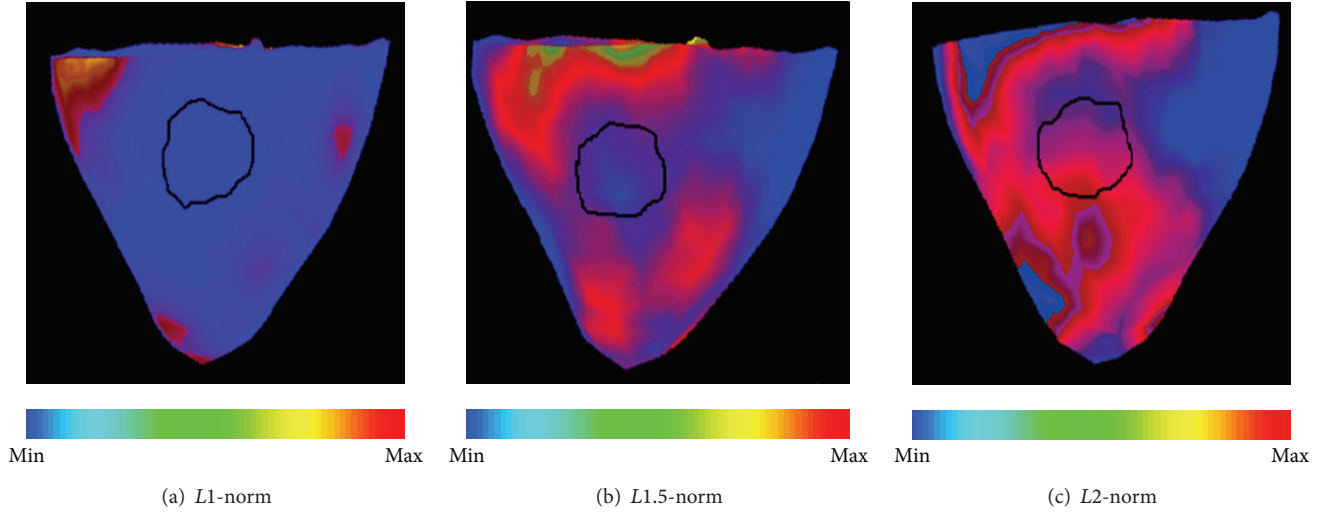


FIGURE 8: Estimation of current sources localized along the scar border using L_p , L_1 - and L_2 -norm regularizations for a post-infarction human subject.

Dalhousie torso model; each BSP recording consists of a single averaged PQRST complex sampled at 2 kHz. Gold standards of the scar were provided by cardiologists who examined the late Gadolinium enhanced (LGE) MR scans of the patient, and were provided in terms of the location and size of the scar with regard to the 17-segment division of the LV according to AHA standards [31]. Specifically, according to the gold standard, the scar center is located at segments 10 and 11, between mid-inferior and mid-inferolateral of the subject's left ventricle (highlighted with black contour in Figure 8).

ECG data collected at the 192 ms during the ST-segment are selected as the input data. As shown in Figure 8(a), the L_1 regularization results in a very sparse solution scattered far from the infarct center. Regions of current sources provided by L_2 regularization (Figure 8(c)) are diffused and cover the scar center; that is, the structure of the scar border cannot be discerned by the reconstruction. The proposed L_p solution ($p = 1.5$) (Figure 8(b)) provides a more accurate estimation of the current sources, which can be seen to distribute around the center of the scar.

5. Discussions and Conclusions

The inverse problem of cardiac source reconstruction is notoriously ill-posed without a unique solution. Progress towards volumetric cardiac source reconstruction is further hindered by the complex structure of current source distribution in the heart because of which the common L_1 - and L_2 -norm constraints are no longer proper because they make an assumption that is either too focal or too smooth regarding the source distribution.

Our experiments' results on localization of current source activity (Section 4.1.1) show that L_1 -norm constraint only works well in recovering focal sources. As a result, it can be employed in the applications where the target source is sparse and focal such as detecting the pacing sites as described in [23–25]. Increasing the size of active source region decreases the performance of L_1 -norm such that the detected sources

are too sparse to provide any information about the structure of source region. These extended source regions occur, for example, as activation and repolarization wavefronts during depolarization and repolarization stages of a cardiac cycle, as shown in Figure 1. In comparison, L_2 -norm regularization provides better approximation of extended source regions while it provides an overly smeared estimation of focal and compact source regions. Because of L_2 -norm smoothing effect, it fails to distinguish multiple proximal active current sources.

We proposed a general L_p -norm regularization to bridge the gap between the scattered and smeared solutions of L_1 and L_2 regularizations and show its potential in imaging cardiac current source distributions that are of important therapeutic information, such as the excitation wavefront, and the source distribution along the myocardial scar border in an infarcted heart. L_p -norm provides a solution that better reflects different spatial properties of cardiac current sources. Our results show its better performance in detecting current sources with different extents compared to L_1 - and L_2 -norms.

It should be noted that our work focuses on estimation of volumetric current sources whose spatial and temporal properties are different from those of an equivalent source model such as the potential distribution on the epicardium [23–25]; while the spatiotemporal dynamics and properties of volumetric current sources (true cardiac sources) are well known and can be well deduced from our knowledge of the physiology of cardiac excitation [32], the spatiotemporal physiological property of epicardial potential as an equivalent source model is not clear. Therefore, the conclusion drawn for one source model regarding which types of regularization would achieve the best performance cannot be directly extended to the other. In addition, in this work the accuracy of source localization is presented in terms of source overlap compared to other surface-based approaches that use relative error and correlation coefficient as accuracy measures [23–25].

At the current stage, the L_p -norm reconstruction is separately performed at each time instant of the measured ECG data. Therefore, temporal information of the electrical current flow in the heart is not taken into account. Because the current flow follows a diffusion process, temporal relation between consecutive time instants has the potential to improve the stability and accuracy of the reconstruction and will be studied in the next step of this research.

It is also observed that, when p increases from 1 to 2, the accuracy of source reconstruction increases then decreases. Our experimental results show that the optimal solutions are obtained at $p = 1.5$ – 1.6 for sources with different sizes, though a larger p is often needed as the size of the source increases (Figure 4). In this feasibility study, $p = 1.5$ is considered for the computer-simulated and real-data experiments. Because it is not possible to foresee the size of the source before the reconstruction, in the future we will investigate the possibility to simultaneously estimate the value of p during the L_p -norm regularization, where the optimal value of p can be decided by the datasets under study.

References

- [1] A. F. Frangi, W. J. Niessen, and M. A. Viergever, "Three-dimensional modeling for functional analysis of cardiac images: a review," *IEEE Transactions on Medical Imaging*, vol. 20, no. 1, pp. 2–25, 2001.
- [2] K. C. L. Wong, H. Zhang, H. Liu, and P. Shi, "Physiome-model-based state-space framework for cardiac deformation recovery," *Academic Radiology*, vol. 14, no. 11, pp. 1341–1349, 2007.
- [3] M. Sermesant, P. Moireau, O. Camara et al., "Cardiac function estimation from MRI using a heart model and data assimilation: advances and difficulties," *Medical Image Analysis*, vol. 10, no. 4, pp. 642–656, 2006.
- [4] R. Plonsey, *Bioelectric Phenomena*, McGraw Hill, New York, NY, USA, 1969.
- [5] J. Z. Wang, S. J. Williamson, and L. Kaufman, "Magnetic source imaging based on the Minimum-Norm Least-Squares inverse," *Brain Topography*, vol. 5, no. 4, pp. 365–371, 1993.
- [6] I. F. Gorodnitsky and B. D. Rao, "Sparse signal reconstruction from limited data using FOCUSS: a re-weighted minimum norm algorithm," *IEEE Transactions on Signal Processing*, vol. 45, no. 3, pp. 600–616, 1997.
- [7] K. Uutela, M. Hämäläinen, and E. Somersalo, "Visualization of magnetoencephalographic data using minimum current estimates," *NeuroImage*, vol. 10, no. 2, pp. 173–180, 1999.
- [8] Y. Rudy and B. J. Messinger-Rapport, "The inverse problem in electrocardiography: solutions in terms of epicardial potentials," *Critical Reviews in Biomedical Engineering*, vol. 16, no. 3, pp. 215–268, 1988.
- [9] G. Huiskamp and F. Greensite, "A new method for myocardial activation imaging," *IEEE Transactions on Biomedical Engineering*, vol. 44, no. 6, pp. 433–446, 1997.
- [10] L. Wang, H. Zhang, K. Wong, H. Liu, and P. Shi, "Electrocardiographic simulation on personalised heart-torso structures using coupled meshfree-BEM platform," *International Journal of Functional Informatics and Personalized Medicine*, vol. 2, no. 2, pp. 175–200, 2009.
- [11] B. He, G. Li, and X. Zhang, "Noninvasive imaging of cardiac transmembrane potentials within three-dimensional myocardium by means of a realistic geometry anisotropic heart model," *IEEE Transactions on Biomedical Engineering*, vol. 50, no. 10, pp. 1190–1202, 2003.
- [12] P. R. Johnston and R. M. Gulrajani, "Selecting the corner in the L-curve approach to Tikhonov regularization," *IEEE Transactions on Biomedical Engineering*, vol. 47, no. 9, pp. 1293–1296, 2000.
- [13] M. Jiang, L. Xia, G. Shou, and M. Tang, "Combination of the LSQR method and a genetic algorithm for solving the electrocardiography inverse problem," *Physics in Medicine and Biology*, vol. 52, no. 5, article 005, pp. 1277–1294, 2007.
- [14] G. Shou, L. Xia, M. Jiang, Q. Wei, F. Liu, and S. Crozier, "Truncated total least squares: a new regularization method for the solution of ECG inverse problems," *IEEE Transactions on Biomedical Engineering*, vol. 55, no. 4, pp. 1327–1335, 2008.
- [15] U. Aydin and Y. S. Dogrusoz, "A Kalman filter-based approach to reduce the effects of geometric errors and the measurement noise in the inverse ECG problem," *Medical & Biological Engineering & Computing*, vol. 49, no. 9, pp. 1003–1013, 2011.
- [16] C. Ramanathan, P. Jia, R. Ghanem, D. Calvetti, and Y. Rudy, "Noninvasive electrocardiographic imaging (ECGI): application of the generalized minimal residual (GMRes) method," *Annals of Biomedical Engineering*, vol. 31, no. 8, pp. 981–994, 2003.
- [17] T. S. Ruud, B. F. Nielsen, M. Lysaker, and J. Sundnes, "A computationally efficient method for determining the size and location of myocardial ischemia," *IEEE Transactions on Biomedical Engineering*, vol. 56, no. 2, pp. 263–272, 2009.
- [18] Y. Serinagaoglu, D. H. Brooks, and R. S. MacLeod, "Improved performance of Bayesian solutions for inverse electrocardiography using multiple information sources," *IEEE Transactions on Biomedical Engineering*, vol. 53, no. 10, pp. 2024–2034, 2006.
- [19] Z. Liu, C. Liu, and B. He, "Noninvasive reconstruction of three-dimensional ventricular activation sequence from the inverse solution of distributed equivalent current density," *IEEE Transactions on Medical Imaging*, vol. 25, no. 10, pp. 1307–1318, 2006.
- [20] D. Wang, R. M. Kirby, R. S. MacLeod, and C. R. Johnson, "An optimization framework for inversely estimating myocardial transmembrane potentials and localizing ischemia," in *Proceedings of the 33rd Annual International Conference of the IEEE Engineering in Medicine and Biology Society (EMBS '11)*, pp. 1680–1683, September 2011.
- [21] L. Wang, K. C. L. Wong, H. Zhang, H. Liu, and P. Shi, "Noninvasive computational imaging of cardiac electrophysiology for 3-D infarct," *IEEE Transactions on Biomedical Engineering*, vol. 58, no. 4, pp. 1033–1043, 2011.
- [22] D. L. Donoho, "Compressed sensing," *IEEE Transactions on Information Theory*, vol. 52, no. 4, pp. 1289–1306, 2006.
- [23] S. Ghosh and Y. Rudy, "Application of L1-norm regularization to epicardial potential solutions of the inverse electrocardiography problem," *Annals of Biomedical Engineering*, vol. 37, no. 5, pp. 692–699, 2011.
- [24] L. Wang, J. Qin, T. T. Wong, and P. A. Heng, "Application of L1-norm regularization to epicardial potential reconstruction based on gradient projection," *Physics in Medicine and Biology*, vol. 56, no. 19, article 009, pp. 6291–6310, 2011.
- [25] G. Shou, L. Xia, F. Liu, M. Jiang, and S. Crozier, "On epicardial potential reconstruction using regularization schemes with the L1-norm data term," *Physics in Medicine and Biology*, vol. 56, no. 1, pp. 57–72, 2011.

- [26] J. Xu, A. Rahimi, F. Gao, and L. Wang, "Localization of sparse transmural excitation stimuli from surface mapping," in *Proceedings of the 15th International Conference on Medical Image Computing and Computer Assisted Intervention (MICCAI '12)*, pp. 657–682, 2012.
- [27] L. Wang, H. Zhang, K. C. L. Wong, H. Liu, and P. Shi, "Physiological-model-constrained noninvasive reconstruction of volumetric myocardial transmembrane potentials," *IEEE Transactions on Bio-Medical Engineering*, vol. 57, no. 2, pp. 296–315, 2010.
- [28] P. A. Krokhmal and P. Soberanis, "Risk optimization with p-order conic constraints: a linear programming approach," *European Journal of Operational Research*, vol. 201, no. 3, pp. 653–671, 2010.
- [29] "Physionet/computers in cardiology challenge 2007: electrocardiographic imaging of myocardial infarction," 2007, <http://physionet.org/challenge/2007/>.
- [30] L. M. Title, S. E. Iles, M. J. Gardner, C. J. Penney, J. C. Clements, and B. M. Horáček, "Quantitative assessment of myocardial ischemia by electrocardiographic and scintigraphic imaging," *Journal of Electrocardiology*, vol. 36, pp. 17–26, 2003.
- [31] M. D. Cerqueira, N. J. Weissman, V. Dilsizian et al., "Standardized myocardial segmentation and nomenclature for tomographic imaging of the heart: a Statement for Healthcare Professionals from the Cardiac Imaging Committee of the Council on Clinical Cardiology of the American Heart Association," *Circulation*, vol. 105, no. 4, pp. 539–542, 2002.
- [32] R. H. Clayton, O. Bernus, E. M. Cherry et al., "Models of cardiac tissue electrophysiology: progress, challenges and open questions," *Progress in Biophysics and Molecular Biology*, vol. 104, no. 1–3, pp. 22–48, 2011.

Research Article

Three-Dimensional Reconstruction of Coronary Arteries and Its Application in Localization of Coronary Artery Segments Corresponding to Myocardial Segments Identified by Transthoracic Echocardiography

Chunyan Zhong,¹ Yanli Guo,¹ Haiyun Huang,¹ Liwen Tan,² Yi Wu,² and Wenting Wang¹

¹ Department of Ultrasound, Southwest Hospital, Third Military Medical University, Chongqing, China

² School of Basic Medicine, Third Military Medical University, Chongqing, China

Correspondence should be addressed to Yanli Guo; guoyanli71@aliyun.com

Received 17 August 2013; Revised 7 October 2013; Accepted 11 October 2013

Academic Editor: Heye Zhang

Copyright © 2013 Chunyan Zhong et al. This is an open access article distributed under the Creative Commons Attribution License, which permits unrestricted use, distribution, and reproduction in any medium, provided the original work is properly cited.

Objectives. To establish 3D models of coronary arteries (CA) and study their application in localization of CA segments identified by Transthoracic Echocardiography (TTE). **Methods.** Sectional images of the heart collected from the first CVH dataset and contrast CT data were used to establish 3D models of the CA. Virtual dissection was performed on the 3D models to simulate the conventional sections of TTE. Then, we used 2D ultrasound, speckle tracking imaging (STI), and 2D ultrasound plus 3D CA models to diagnose 170 patients and compare the results to coronary angiography (CAG). **Results.** 3D models of CA distinctly displayed both 3D structure and 2D sections of CA. This simulated TTE imaging in any plane and showed the CA segments that corresponded to 17 myocardial segments identified by TTE. The localization accuracy showed a significant difference between 2D ultrasound and 2D ultrasound plus 3D CA model in the severe stenosis group ($P < 0.05$) and in the mild-to-moderate stenosis group ($P < 0.05$). **Conclusions.** These innovative modeling techniques help clinicians identify the CA segments that correspond to myocardial segments typically shown in TTE sectional images, thereby increasing the accuracy of the TTE-based diagnosis of CHD.

1. Introduction

The incidence of coronary heart disease (CHD) has increased in China. Due to technical advances, transthoracic echocardiography (TTE) and new TTE-based techniques (such as myocardial contrast echocardiography and myocardial quantitative analysis) have become important diagnostic and prognostic modalities in CHD [1]. In contrast to CAG, TTE indicates myocardial ischemia by identifying abnormal segmental movements of the ventricular wall in CHD patients and cannot directly display the occluded coronary arteries. Therefore, the use of TTE is limited in the diagnosis and assessment of CHD [2, 3]. In addition, TTE has difficulty in displaying the blood flow in the coronary arteries due to the complicated paths, narrow lumina, and frequent anatomic variations of the coronary arteries. In the present study, 3D

visible models of human coronary arteries were established based on the Chinese visible human (CVH) datasets and coronary CT images. These models provide 2D and 3D anatomical bases for the localization of coronary artery segments that correspond to the 17 myocardial segments identified by conventional TTE. This work may help directly identify occluded coronary arteries by using TTE to display myocardial segmental abnormalities in CHD patients.

2. Materials and Methods

2.1. Acquisition of Heart Slice Images. The CVH datasets comprised 286 successive sections of the heart from the first female CVH. The slice thickness was 0.5 mm, and the image resolution was 3072×2048 pixels. The CT datasets

comprised 266 CT images of the heart obtained during CAG. The subjects included 3 men and 2 women without any heart disease, who were aged 25–48 years and had a medium body height. The slice thickness was 0.5 mm, and the image resolution was 512×512 pixels.

2.2. 3D Reconstructions of the Coronary Arteries

2.2.1. Data Partitioning. The “magnetic lasso” and the “polygonal lasso” in Photoshop CS2 9.0 were used to permit data partitioning of the coronary artery imaging data in the CVH datasets. Then, different gray values were assigned to different branches of the coronary arteries. These images were saved in PNG format.

Partitioning tools such as “threshold segmentation,” “magnetic lasso,” and “semiautomatic identification” in the Amira 5.2.1 software were used to segment the coronary arteries in dual source computed tomography angiography (DSCTA). Then, different branches of the coronary arteries were labeled. The labels were colored with different RGB values and saved in AM format.

2.2.2. Reconstruction. The hardware used in our research included the following equipment: a dual-core CPU with AMD Hyper Transport TM technology, a 64-bit Windows XP operating system, a Dual Graphic Quadro FX 4500 graphics card, 64 MB of video memory, support for OpenGL 4.4, 16.0 GB of physical memory, and 4.0 GB of virtual memory. We also used Amira 5.2.1 software.

A total of 286 layers of CVH partitioning data were imported into the Amira 5.2.1 software, and the “Channel 1” mode was selected as the gray value channel. The selected voxel parameter values were 0.167/0.167/1.0 in the $X/Y/Z$ directions, respectively, and surface rendering was started by the software. Color layers were imported into the “color field,” and volume rendering was completed. Surface rendering and volume rendering were obtained from the same data and used the same coordinates, allowing the software to match them together without errors. The “am” DSCTA datasets were imported into Amira 5.2.1. We then clicked the “File” button to choose the correct “am” file, which was renamed, and completed the surface rendering. All the “am” files were selected and opened in Amira 5.2.1, and volume rendering was then completed.

The software could reconstruct 3D models automatically by right clicking on the surface rendering mode, choosing “Labeling—Label field,” and clicking the “SurfaceGen” button. Then, “SurfaceView” was clicked to display the models. Clicking the “OrthoSlice” button displayed three planes in the $xy/xz/yz$ directions. “Display—ObliqueSlice” was chosen to control the virtual spin ball and to choose any desired angle and slice.

2.3. Establishment of 3D Visible Models of the Coronary Arteries. Coronary artery images from the surface and volume renderings were displayed in combination to establish the 3D models of the coronary arteries. According to the myocardial segmentation method stipulated by the American Heart

Association, virtual dissection was performed using Amira 5.2.1 on the 3D visible models to simulate conventional TTE sections, including a long-axis view of the left ventricle, a 4-chamber apical view, a 2-chamber apical view, and a short-axis view of the left ventricle (including a short-axis view of the basal segment, a short-axis view of the left ventricular papillary muscle, a short-axis view of the apex, and a top view of the apex).

2.4. Acquisition of Normal Ultrasound Images. Fifteen healthy medical students underwent TEE using a Philips IE33 color Doppler scanner with an S5-1 heart probe to obtain conventional sectional images including a long-axis view of the left ventricle, a four-chamber apical view, a two-chamber apical view, and a short-axis view of the left ventricle (including a short-axis view of the basal segment, a short-axis view of the left ventricular papillary muscle, a short-axis view of the apex, and a top view of the apex). All images were stored in AVI or DICOM format on compact discs (CDs).

2.5. Clinical Application

2.5.1. Studying Objects. A total of 170 patients (95 males and 75 females), aged between 40 and 82 years (61.2 ± 8.9), with a positive history or clinical suspicion of CHD, were treated at the Southwest Hospital between January 2011 and October 2011.

2.5.2. 2D Ultrasound Images. Ultrasound images were acquired according to the methods described in Section 2.4. Coronary lesions were diagnosed by the sonographic identification of abnormal segmental ventricular wall motion. The examiners were unaware that ultrasonography was being performed for the purposes of this study.

2.5.3. Location of Coronary Artery Lesions Using STI. After image acquisition, CMQ in the QLab software was used to open a 4-chamber apical view in diastole. In these images, 3 points (the anterior mitral valve annulus, the posterior mitral valve annulus, and the apex cordis) were selected and then divided into 7 segments (segments 3, 6, 9, 12, 14, 16, and 17) automatically using the AP4 mode. The shape and direction of these areas of interest were adjusted to conform to the myocardial thickness. The same methods were used with AP2 mode in a 2-chamber apical view to identify 7 segments (segments 1, 4, 7, 10, 13, 15, and 17). The same methods were then used with the AP3/LAX mode in the long-axis view of the left ventricle to view segments 2, 5, 8, 11, 14, 16, and 17.

2.5.4. Locating Coronary Artery Lesions Using 3D Models of the Coronary Arteries. For slices with echocardiographic evidence of abnormal segmental ventricular wall motion, “ObliqueSlice” was clicked in the volume rendering of the coronary arteries to simulate different ultrasound image angles by rotating the spin ball in the software. For each patient, an average of 25 minutes was needed to analyze the lesioned coronary artery and its branches.

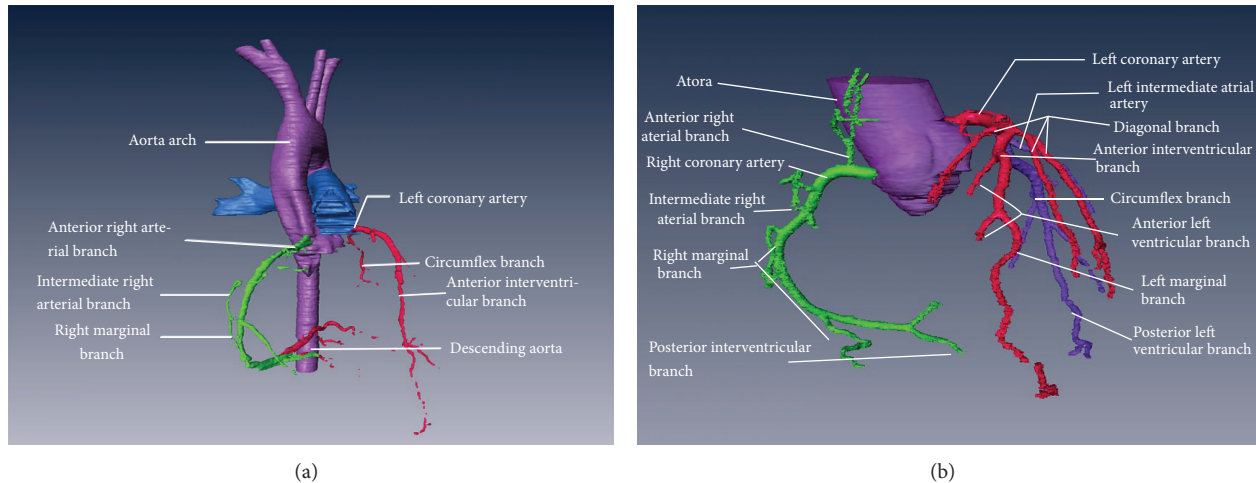


FIGURE 1: 3D visible models of the coronary arteries based on the CVH and cardiac CT datasets. (a) Coronary artery model based on the CVH dataset. (b) Coronary artery model based on the cardiac CT dataset.

2.5.5. CAG Examination. The CAG examination was performed to confirm the results of the ultrasound and 3D coronary artery models. The Judkin method was used for the CAG examination. When $>50\%$ stenosis was present, the CAG examination was considered positive; otherwise, it was considered negative.

2.5.6. Statistical Analysis. The diagnostic accuracy rates were compared between the following: 2D ultrasound and 2D ultrasound plus 3D coronary artery models and STI and 2D ultrasound plus 3D coronary artery models. The data were analyzed using SPSS 13.0 software. Numerical data were compared using the χ^2 test. A P value of <0.05 was deemed statistically significant.

3. Results

In the present study, 3D visible models of the human coronary arteries were established on the basis of the CVH and clinical CT image datasets (Figures 1(a) and 1(b)). These models were right dominant, which is representative of the coronary artery anatomy in approximately 2/3 of Chinese people. These models can distinctly display the trunk and main branches of the normal human coronary arteries. The CT-based coronary artery model can display most of the tertiary branches of the coronary arteries. Moreover, these models combined the 3D structure of the coronary arteries and their branches with gross anatomic and 2D sections of the heart to simulate conventional TTE sections. In these models, the coronary artery segments corresponding to the 17 myocardial segments identified by conventional TTE can be displayed distinctly and recognized accurately (Figure 2).

3.1. Dissection of the Parasternal Short-Axis View of the Left Ventricle on 3D Visible Models of the Coronary Arteries and Comparison with TTE. The parasternal short-axis view of the left ventricle usually displayed blood supply to the left

ventricular wall, helping to identify the site of myocardial ischemia and infarction. Various parts of the left ventricular wall could be displayed along the short axis. At the mitral leaflet level, the left ventricular wall near the cardiac base was displayed, and the middle and apical parts of the left ventricular wall were displayed at the papillary muscle and apical levels, respectively.

3.1.1. Parasternal Short-Axis View of the Left Ventricle at the Level of the Mitral Leaflet Segments 1–6 of the Left Ventricular Myocardium Was Displayed. On the CVH-based coronary artery model, the upper and middle segments of the anterior descending branch of the left coronary artery supplied blood to segments 1 and 2 (i.e., the anterior septal base and the anterior wall base, resp.), the middle and inferior segments of the left circumflex branch supplied blood to segments 3 and 4 (i.e., the base of the lateral wall and the base of the posterolateral wall, resp.), and the right coronary artery supplied blood to segments 5 and 6 (i.e., the base of the posteroinferior/inferior wall). The CT-based coronary artery model showed that the anterior left ventricular branch supplied blood to segment 1, the diagonal branch supplied blood to segment 2, the posterior interventricular branch supplied blood to segments 3 and 4, the left intermediate artery supplied blood to segment 5, and the left marginal branch supplied blood to segments 5 and 6 (Figures 3(a) and 3(b)).

3.1.2. Parasternal Short-Axis View of the Left Ventricle at the Level of the Papillary Muscle. Myocardial segments 7–12 of the left ventricle were displayed, including the posterior septal base, the septal base, the anterior septum, the anterior wall, the lateral wall, and the posterolateral wall. On the CVH-based coronary artery model, the middle and inferior segments of the anterior descending branch of the left coronary artery supplied blood to segments 7 and 8, respectively, the left circumflex branch supplied blood to

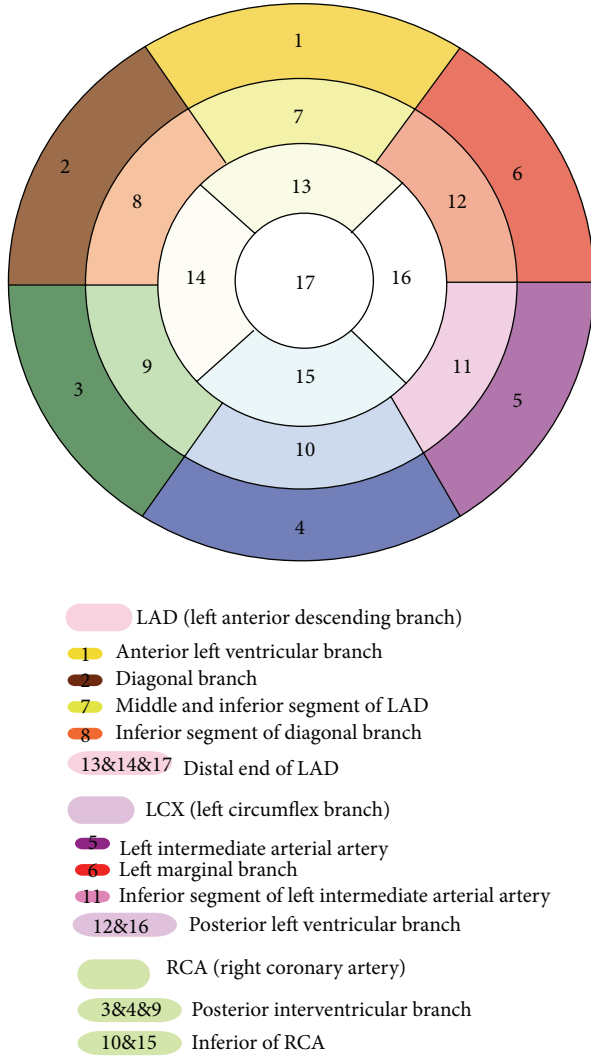


FIGURE 2: Our identification of the coronary artery segments corresponding to the 17 myocardial segments.

segments 9 and 10, and no vessels penetrated segments 11 and 12. On the CT-based coronary artery model, the middle and inferior segments of the anterior descending branch trunk supplied blood to segment 7, the interior segment of the diagonal branch supplied blood to segment 8, the posterior interventricular branch supplied blood to segment 9, the inferior right coronary artery supplied blood to segment 10, the inferior segment of the left intermediate atrial artery supplied blood to segment 11, and the posterior left ventricular branch supplied blood to segment 12 (Figures 4(a) and 4(b)).

3.1.3. Parasternal Short-Axis View of the Left Ventricle at the Level of the Apex. Myocardial segments 13–17 of the left ventricle were displayed, including the posteroinferior wall, the inferior wall, the posterior septum, the septum, and the apex of the anterior wall. Coronary artery models based on the CVH and CT datasets showed that the distal end of the left anterior descending branch supplied blood to segments 13,

14, and 17, the inferior right coronary artery supplied blood to segment 15, and the posterior left ventricular branch supplied blood to segment 16 (Figures 5(a) and 5(b)).

3.2. Visualization of the Heart in a 4-Chamber Apical View Using the Coronary Artery Model and Comparison with TTE Studies. Myocardial segments 3, 9, 13, 16, and 17 of the left ventricle were displayed in the 4-chamber apical view. This view usually displays the posterior septum and clearly displays the morphology and motion of the anterolateral wall of the left ventricle. On the coronary artery models based on the CVH and CT datasets, the posterior interventricular branch supplied blood to segments 3 and 9, the distal end of left anterior descending branch supplied blood to segments 13 and 17, and the posterior left ventricular branch supplied blood to segment 16 (Figures 6(a) and 6(b)).

3.3. Localization Accuracy of the 3 Methods for Lesions in the Coronary Arteries. The CAG showed that there were 141 patients with coronary stenosis and 29 patients without stenosis. In these 141 patients, 43 patients were classified as having severe stenosis, with at least 75% blockage of 1 coronary artery. This group contained 65 males and 14 females. The other 97 patients were classified as having mild-to-moderate stenosis. This group contained 65 males and 33 females, who ranged in age from 40 to 82 years. The results of all 4 diagnostic methods in each group are shown in Tables 1 and 2. The localization accuracy of the 2D ultrasound, STI and, the 2D ultrasound plus 3D coronary artery model was 69.8% (30/43), 88.4% (38/43), and 88.4% (38/43), respectively, in the severe stenosis group (Table 3). The localization accuracy in the mild-to-moderate stenosis group was 66.3% (65/98) for 2D ultrasound, 90.8% (89/98) for STI, and 89.8% (88/98) for the 2D ultrasound plus 3D coronary artery model (Table 4). The results showed a significant difference between the 2D ultrasound and 2D ultrasound plus 3D coronary artery model in the severe stenosis group ($P < 0.05$) and in the mild-to-moderate stenosis group ($P < 0.05$). Additionally, there was no significant difference between the STI and 2D ultrasound plus 3D coronary artery model.

4. Discussion

CHD is a common cardiovascular disease and the leading cause of death in western countries. The incidence of CHD has tended to increase in China. Therefore, the early diagnosis and posttreatment assessment of CHD are clinically significant. TTE provides important diagnostic and prognostic information for CHD because of its lack of invasiveness, simple examination technique, and ability to provide ample anatomical and hemodynamic information. Abnormal segmental ventricular wall motion is a sensitive and specific indicator for myocardial ischemia. To facilitate data exchange among various imaging modalities, including ultrasonography, radionuclide imaging, MRI, and CT, the American Heart Association (AHA) has suggested a myocardial segmentation method that divides the myocardium into 17 segments [4]. In contrast to other imaging modalities, TTE suggests the

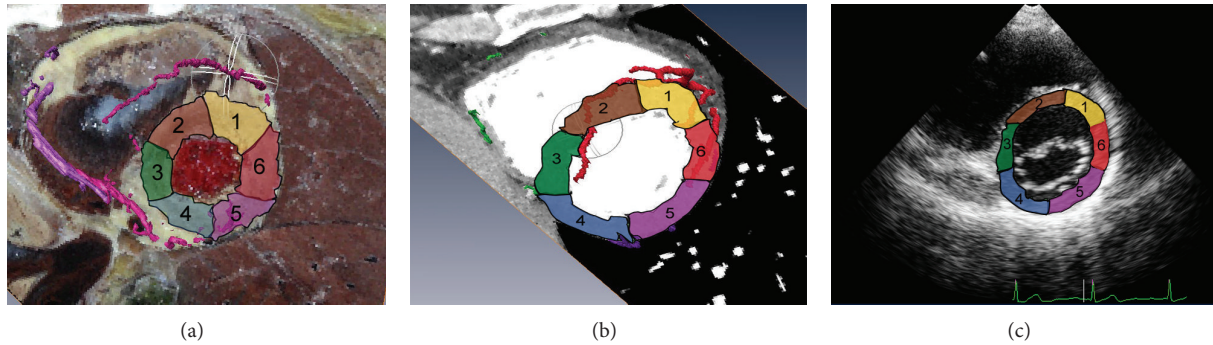


FIGURE 3: Short-axis sections of left ventricle at the level of the mitral leaflet. (a) Fusion display of the CVH dataset and the coronary artery model. (b) Fusion display of the cardiac CT dataset and the coronary artery model. (c) Short-axis section of the left ventricle at the level of the mitral leaflet revealed by echocardiography.

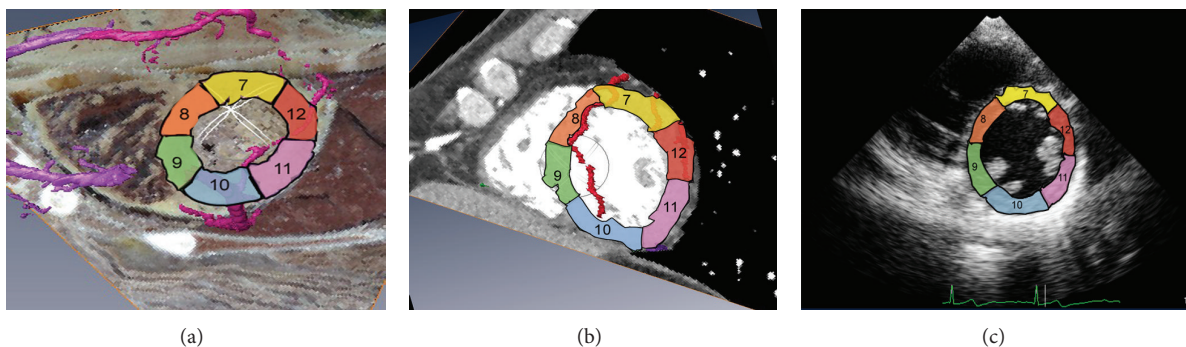


FIGURE 4: Short-axis sections of the left ventricle at the level of the papillary muscle. (a) Fusion display of the CVH dataset and the coronary artery model. (b) Fusion display of the cardiac CT dataset and the coronary artery model. (c) Short-axis section of the left ventricle at the level of the papillary muscle revealed by echocardiography.

presence of an occluded coronary artery by detecting the abnormal motion of the ventricular wall. The identification of the coronary artery segments that correspond to the myocardial segments directly on TTE 2D sections is difficult. Therefore, 3D visible models of the human coronary arteries were established in the present study on the basis of the CVH dataset and a normal cardiac CT dataset, thereby providing both 2D and 3D anatomic bases for localizing the coronary artery segments corresponding to the 17 myocardial segments identified by conventional TTE.

4.1. Establishment of 3D Visible Models of the Coronary Arteries. The coronary arteries are the first pair of branches originating from the ascending aorta and provide the primary supply of blood to the heart. The trunk of the left coronary artery originates from the left coronary sinus. The left coronary artery passes between the pulmonary artery and left auricle and bifurcates into the anterior descending branch and the left circumflex branch. The anterior descending branch divides into the left arterial cone, the right ventricular anterior branch, the left ventricular anterior branch, the anterior septal artery, and the diagonal branch. The left circumflex branch divides into the left ventricular anterior branch, the marginal branch, the left atrial branch, and the

left ventricular posterior branch. The right coronary artery originates from the anterior aortic sinus; its branches include the right arterial cone, the right ventricular anterior branch, the right marginal branch, the right ventricular posterior branch, the right atrial branch, the atrioventricular nodal artery, the posterior descending branch, and the left atrial posterior branch. Three-dimensional visualizations of the coronary arteries are challenging because of the large number of thin branches from these vessels, which have a highly variable anatomy. The CVH has been demonstrated to help individuals master medical imaging technologies. Based on the CVH, virtual human organs and tissues with real anatomical information can be modeled, thereby facilitating 3D visualizations of human anatomy [5–7]. In the present study, we used the cardiac dataset from the first CVH reported by the Computerized Medicine Laboratory of the Third Military Medical University in February 2003 [8, 9]. The 3D visible model of the coronary arteries that was based on the CVH dataset clearly displayed the 3D structure of the left and right coronary arteries and their major branches, such as the anterior interventricular branch, left circumflex branch, arterial cone, and posterior interventricular branch. Because the CVH dataset contains delicate anatomical information in 2D sections, the courses and locations of the coronary arteries can be displayed distinctly on the 3D visible model using

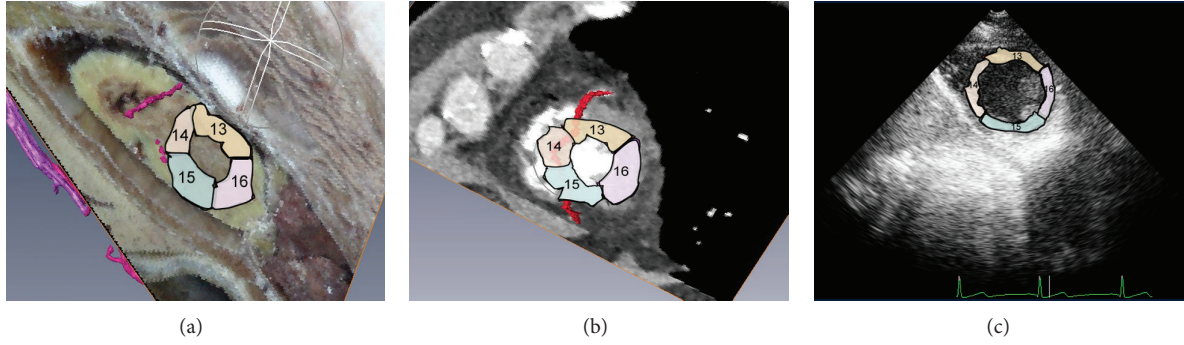


FIGURE 5: Short-axis sections of the left ventricular apex. (a) Fusion display of the CVH dataset and the coronary artery model. (b) Fusion display of the cardiac CT dataset and the coronary artery model. (c) Short-axis section of the left ventricular apex revealed by echocardiography.

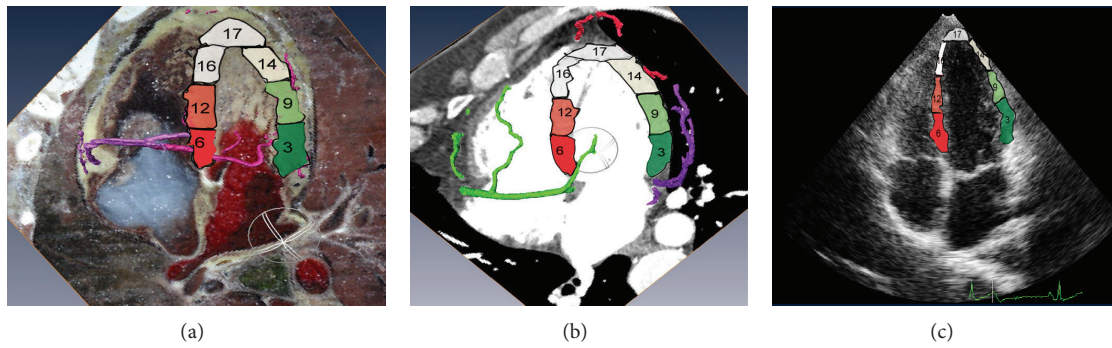


FIGURE 6: Four-chamber heart sections. (a) Fusion display of the CVH dataset and the coronary artery model. (b) Fusion display of the cardiac CT dataset and the coronary artery model. (c) Two-chamber heart section revealed by echocardiography.

TABLE 1: Number of lesioned coronary artery branches detected by the 4 imaging methods (severe stenosis group).

Method	LAD	LCX	RCA	Multivessel lesion	Total
2D ultrasound	6	2	3	32	43
STI	7	3	5	28	43
2D ultrasound plus 3D model	9	4	5	25	43
CAG	9	4	6	24	43

LAD: left anterior descending branch; LCX: left circumflex branch; RCA: right coronary artery; CAG: coronary angiography; STI: speckle tracking imaging.

TABLE 2: Number of lesioned coronary artery branches detected by the 4 imaging methods (light-moderate stenosis group).

Method	LAD	LCX	RCA	Multivessel lesion	Total
2D ultrasound	20	5	11	62	98
STI	21	7	11	61	98
2D ultrasound plus 3D model	23	6	11	58	98
CAG	24	6	11	57	98

LAD: left anterior descending branch; LCX: left circumflex branch; RCA: right coronary artery; CAG: coronary angiography; STI: speckle tracking imaging.

TABLE 3: Accuracy of localization for lesioned coronary arteries using 3 different imaging methods (severe stenosis group).

Methods	CAG results		Accuracy of localization (%)
	True	False	
2D ultrasound	30	13	69.8*
STI	38	5	88.4
2D ultrasound plus 3D model	38	5	88.4

* $P < 0.05$ for 2D ultrasound versus 2D ultrasound plus 3D model.

TABLE 4: Accuracy of localization for lesioned coronary arteries using 3 different imaging methods (severe stenosis group).

Methods	CAG results		Accuracy of localization (%)
	True	False	
2D ultrasound	65	33	66.3*
STI	89	9	90.8
2D ultrasound plus 3D model	88	10	89.8

* $P < 0.05$ 2D ultrasound versus 2D ultrasound plus 3D model.

software-based dissection, suggesting that the CVH dataset can provide high-quality, well-aligned 2D data for establishing 3D visible models of the human coronary arteries.

Due to the highly variable anatomy of the coronary arteries, a single CVH dataset is not adequate for a 3D visualization study of the coronary arteries. Computed tomography angiography (CTA) of the coronary arteries has been shown to clearly display the trunk and branches of the coronary arteries, particularly the trunk of the main coronary artery, the proximal segment of the right coronary artery, the proximal segment of the anterior descending branch, and the proximal segment of the left circumflex branch [10, 11]. CTA is less effective than CAG in displaying the distal segment of the right coronary artery, the distal segment of the left anterior descending branch, and the distal segment of the circumflex branch. The CTA dataset complements the CVH dataset to display the 3D structure of the coronary arteries. Based on CTA datasets from 5 subjects without heart disease, 5 3D visible models of the coronary arteries were established. Compared with the 3D visible model based on the CVH dataset, the models based on the CTA datasets displayed the coronary arteries and their branches clearly, including the trunk and branches of the left and right coronary arteries. The CTA-based models combined with the CT-based 2D sectional images complement the 3D model that was based on the CVH dataset, showing the delicate course of the coronary artery branches and providing a basis for fusing and converting cardiac CT and echocardiographic images to 3D models.

4.2. 3D Visible Models of the Coronary Arteries Provide 2D and 3D Anatomical Bases for the TTE-Based Diagnosis of CHD. Recently, virtual reality medicine (VRM) has been widely used in medicine [12]. Using VRM, anatomical structures can be viewed with 3D reconstructions in any direction, and virtual dissections can be performed as needed to visualize intracardiac structures and vessels. Therefore, VRM can provide 2D and 3D anatomical bases for various imaging modalities, such as ultrasonography, CT, and MRI [13, 14]. In the present study, 3D visual models of the coronary arterial anatomy were established on the basis of the CVH and cardiac CT imaging datasets. These models can clearly display the 3D courses and spatial relationships of the coronary arteries and can be dissected and rotated in any direction with the use of 3D reconstruction software. We further simulated conventional TTE imaging of the left ventricle in various views to display the coronary arteries with their branches

corresponding to the 17 segments of the left ventricle and compared these results with conventional TTE sectional images. To the best of our knowledge, this report is the first 3D visualization study of the coronary arteries that was based on CVH and CT imaging datasets and a comparison with TTE. In our research, combining 2D ultrasound and 3D coronary artery models can significantly improve the accuracy with which lesioned coronary arteries are located. The accuracy of 2D ultrasound plus the 3D coronary artery model was similar to that of STI. Thus, we can include these models in a diasonograph to display the coronary arteries in 2D ultrasound images without image postprocessing. This technique could permit the diagnosis of coronary artery disease using 2D ultrasound imaging.

In summary, 3D visible models of the coronary arteries can simulate conventional TTE imaging. These models can clearly display the coronary artery branches corresponding to the 17 segments of the left ventricle, thereby providing anatomical landmarks for 2D echocardiography and helping clinicians identify coronary artery segments through myocardial segments displayed by TTE.

Acknowledgments

This work was supported by the Commercialization of Research Findings in Third Military Medical University (2009XZH07) and the National Science Foundation of China (no. 61190122).

References

- [1] B. D. Hoit, "Strain and strain rate echocardiography and coronary artery disease," *Circulation: Cardiovascular Imaging*, vol. 4, no. 2, pp. 179–190, 2011.
- [2] N. Gaibazzi, F. Rigo, and C. Reverberi, "Detection of coronary artery disease by combined assessment of wall motion, myocardial perfusion and coronary flow reserve: a multiparametric contrast stress-echocardiography study," *Journal of the American Society of Echocardiography*, vol. 23, no. 12, pp. 1242–1250, 2010.
- [3] X. Zhang, Y. Yang, Z. Li, H. Ren, J. Lin, and L. Wang, "Noninvasive evaluation of coronary flow velocity reserve in homozygous familial hypercholesterolemia by transthoracic doppler echocardiography," *Echocardiography*, vol. 27, no. 8, pp. 985–989, 2010.
- [4] I. Farid, D. Litaker, and J. E. Tetzlaff, "Implementing ACC/AHA guidelines for the preoperative management of patients with coronary artery disease scheduled for noncardiac surgery: effect

- on perioperative outcome,” *Journal of Clinical Anesthesia*, vol. 14, no. 2, pp. 126–128, 2002.
- [5] T. Wu, L. Tan, Q. Shao et al., “Chinese adult anatomical models and the application in evaluation of RF exposures,” *Physics in Medicine and Biology*, vol. 56, no. 7, pp. 2075–2089, 2011.
- [6] Y. L. Guo, P. A. Heng, S. X. Zhang et al., “Thin sectional anatomy, three-dimensional reconstruction and visualization of the heart from the Chinese visible human,” *Surgical and Radiologic Anatomy*, vol. 27, no. 2, pp. 113–118, 2005.
- [7] Y. L. Guo, S. X. Zhang, Z. J. Liu et al., “Three dimensional virtual heart and multiple transesophageal echocardiography,” *Chinese Journal of Ultrasound in Medicine*, vol. 19, no. 12, pp. 917–920, 2003.
- [8] S. X. Zhang, Z. J. Liu, L. W. Tan et al., “Number one of Chinese digitized visible human completed,” *Acta Academiae Medicinae Militaris Tertiae*, vol. 24, no. 10, pp. 1231–1232, 2002.
- [9] S. X. Zhang, P. A. Wang, L. W. Tan et al., “Visualization of the first Chinese visible human male and female,” *Acta Academiae Medicinae Militaris Tertiae*, vol. 25, no. 7, pp. 563–565, 2003.
- [10] R. Mitsutake, S. Miura, Y. Shiga, Y. Uehara, and K. Saku, “Association between hypertension and coronary artery disease as assessed by coronary computed tomography,” *Journal of Clinical Hypertension*, vol. 13, no. 3, pp. 198–204, 2011.
- [11] E. T. D. Hoey, “Coronary CT angiography: a paradigm shift in the evaluation of coronary artery disease?” *Postgraduate Medical Journal*, vol. 87, no. 1025, pp. 163–164, 2011.
- [12] N. Saied, “Virtual reality and medicine—from the cockpit to the operating room: are we there yet?” *Missouri medicine*, vol. 102, no. 5, pp. 450–455, 2005.
- [13] B. S. Lange, P. Requejo, S. M. Flynn et al., “The potential of virtual reality and gaming to assist successful aging with disability,” *Physical Medicine and Rehabilitation Clinics of North America*, vol. 21, no. 2, pp. 339–356, 2010.
- [14] M. J. Ackerman, “The visible human project: a resource for education,” *Academic Medicine*, vol. 74, no. 6, pp. 667–670, 1999.

Research Article

A Voxel-Map Quantitative Analysis Approach for Atherosclerotic Noncalcified Plaques of the Coronary Artery Tree

Ying Li,¹ Wei Chen,² Kaijun Liu,¹ Yi Wu,¹ Yonglin Chen,² Chun Chu,¹
Bingji Fang,¹ Liwen Tan,¹ and Shaoxiang Zhang¹

¹ Institute of Computing Medicine, Third Military Medical University, Chongqing 400038, China

² Department of Radiology, Southwest Hospital, Third Military Medical University, Chongqing 400038, China

Correspondence should be addressed to Liwen Tan; tlwtan@163.com and Shaoxiang Zhang; zhangsx1021@yahoo.com

Received 5 September 2013; Accepted 22 October 2013

Academic Editor: Heye Zhang

Copyright © 2013 Ying Li et al. This is an open access article distributed under the Creative Commons Attribution License, which permits unrestricted use, distribution, and reproduction in any medium, provided the original work is properly cited.

Noncalcified plaques (NCPs) are associated with the presence of lipid-core plaques that are prone to rupture. Thus, it is important to detect and monitor the development of NCPs. Contrast-enhanced coronary Computed Tomography Angiography (CTA) is a potential imaging technique to identify atherosclerotic plaques in the whole coronary tree, but it fails to provide information about vessel walls. In order to overcome the limitations of coronary CTA and provide more meaningful quantitative information for percutaneous coronary intervention (PCI), we proposed a Voxel-Map based on mathematical morphology to quantitatively analyze the noncalcified plaques on a three-dimensional coronary artery wall model (3D-CAWM). This approach is a combination of Voxel-Map analysis techniques, plaque locating, and anatomical location related labeling, which show more detailed and comprehensive coronary tree wall visualization.

1. Introduction

Noncalcified plaque (NCP, referred to as “soft plaque”) [1] usually shows lower attenuation values than calcified plaque in a CT image, which has been associated with the presence of lipid-core plaques [2]. Retrospective studies have shown an association between plaques containing non-calcified components and acute coronary syndrome (ACS) [3, 4]. Therefore, it is important to detect and monitor the progress of NCPs.

According to whether or not the body has to be injured during detection of a lesion, the imaging techniques for detection and quantitative analysis of NCPs are classified into two categories: invasive methods and noninvasive methods [5]. Imaging techniques, such as intravascular ultrasound (IVUS) and optical coherence tomography (OCT), provide detailed visualization of luminal and plaque morphology and reliable quantification of the atheroma burden and its composition [5]. Although intravascular techniques have good discriminability for NCPs, they are invasive and expensive and can only be performed in proximal vessel segments [6]. Therefore, they are not appropriate to monitor the progress of

NCPs of the whole coronary tree over a short time interval. Compared with intravascular ultrasound (IVUS), contrast-enhanced coronary Computed Tomography Angiography (CTA) has the advantages of being noninvasive, convenient, and economical and offers excellent diagnostic accuracy for coronary plaques [6–10]. The potential of these imaging techniques to identify atherosclerotic plaques in the whole coronary tree has raised the interest of radiologists [11]. The range of attenuation relevance to different types of plaque in CTA has been a concern over recent years. For example, there are three typical plaques that include non-calcified plaque (NCP, referred to as “soft plaque”), partially calcified plaque (PCP, also called “mixed plaque”), and calcified plaque (CP). Further details about CT attenuation value can be found in review [1].

The main limitation of traditional methods in a CTA image for the visualization of coronary artery disease is the inability to provide information about vessel walls [1]. In order to recognize NCPs, a radiologist needs to detect stenosis through various reconstruction methods and then quantitatively analyze plaques by manually drawing the boundaries of the wall and plaques [8, 10]. The current standard for

coronary CT angiography plaque quantification is automatic but requires manual tracing of contours, separating epicardial fat from the vessel wall and enclosing non-calcified and calcified plaque components; this contribution promotes the plaque quantitative accuracy by accurately describing the wall border but is time consuming and may be prone to intraobserver variability [12–14]. In order to automatically trace the wall border, a previous study proposed an interactive approach that radiologists have to mark the initial and end points of the plaque in a curved multiplanar reformatted (CMPR). Further, an automated algorithm for unsupervised computer detection of coronary artery lesions has been proposed [15], but plaques are prone to be missed if they do not belong to “stenosis” by their definition. Therefore, the identification of the wall and plaques is still a challenging area.

In addition, with the development of PCI, more meaningful quantitative information is necessary to plan the path of the percutaneous coronary intervention and to assess the outcome. It is important to predict the potential location related danger in the process of PCI and also whether the catheter is able to pass through the vessel where plaque is located in the coronary tree. Higher requirements are put forward on further information of quantitative plaques such as size, type, and location quantification in a 3D space.

Above all, in order to overcome the limitations of coronary CTA and provide more meaningful quantitative information for PCI, we propose a quantitative analysis approach based on a mathematical morphology named Voxel-Map for non-calcified plaque based on a three-dimensional coronary-tree model. This method is a combination of Voxel-Map analysis techniques, plaque locating, and anatomical location related labeling that show more detailed and comprehensive coronary tree wall visualization.

2. Materials and Methods

2.1. Imaging Acquisition. All patients were scanned with a DSCT scanner (Somatom Definition, Siemens Medical Solutions, Germany). No beta-blockers were administered for the scan irrespective of the individual heart rate. The ECG was continuously recorded and stored throughout the scan. A nonenhanced DSCT was carried out from 1 to 1.5 cm below the level of the tracheal bifurcation to the diaphragm in the craniocaudal direction. For contrast-enhanced scans, intravenous bolus (60–80 mL) of a contrast agent with 370 mg of iodine per milliliter (iopromide, 370 mg of iodine/mL; Ultravist 370, Bayer-Schering, Berlin, Germany) was injected at a flow rate of 6 mL/sec, and a 50 mL chaser saline bolus was achieved with an automated injection through a power injector (Ulrich, USA). Estimation of individual circulation times was based on the test bolus technique with 20 mL bolus tracking. Data acquisition parameters for CT angiography were 0.6 mm collimation, 330 ms rotation time, 120 kV tube voltage, and 400 m as tube current. A contrast-enhanced volume data set was acquired with retrospective electrocardiogram (ECG) gating to allow reconstructions during all phases of the cardiac cycle. Transaxial images were reconstructed with 0.75 mm section thickness, 0.4 mm increment, and

a medium-soft convolution kernel (B26f). The position of the reconstruction window in the cardiac cycle was individually selected to minimize artifacts.

Through Voxel-Map analysis and quantification algorithms implemented by Matlab software version 8.0 (R2012b), we treated each image as a vector. All images of one patient are treated as a set of vectors. The processing is in parallel in Matlab without complex conditions and loop operations. Segmentation, 3D reconstruction, and centerline were extracted and labeled by Amira software (V. 5.4).

2.2. Segmentation and 3D Coronary Tree Model. According to recent pieces of literature on the attenuation cutoffs between the arterial wall and lumen [6, 10, 15–17], a voxel with an attenuation value greater than 160 Hounsfield units (HU) was defined as being the first voxel within the lumen. Based on this assumption and according to our experiment results (see Figure 1), which showed that the CT attenuation value gradient decreased from the inside to the outside the arterial wall, we can conclude that most of the voxel of the inner lumen will be greater than 160 HU. On the other hand, the attenuation values outside of lumen will be less than 160 HU. As such, we set 160 HU values as the threshold to segment highlight voxels in lumen. Then we refined the coronary tree by a region growing method to fill small holes and obtained lumen boundaries, which are well satisfied to connective relationships. After that, we obtained the segmentation of the three-dimensional coronary tree, which set 1 as foreground and 0 as background. We then used this data for centerline extraction. After an array multiply was performed on segmentation images and original CTA images, a three-dimensional coronary tree model (3D-CTM) was generated, which maintained the original attenuation values and excluded approximate attenuation values belonging to other regions. We used this model for Voxel-Map analysis.

2.3. Centerline Extraction. We imported the segmentation of the 3D coronary tree data into Amira software and selected “skeleton” and “centerline,” and then the 3D centerline of the coronary tree was generated automatically. After setting the segment with a minimum value of z -coordinate as root, we identified the tree as hierarchical relations and manually labeled all segments by anatomical names referring to the 17-segment model defined by the American Heart Association (AHA) [18]. We then exported the information for the centerline as a data structure which includes the start point, length, label, and the connect relationship of each segment, along with the x -, y -, and z -coordinates of each point and its radius.

2.4. Morphological Voxel-Map. We developed a Voxel-Map based on mathematical morphology [19], which is a broad set of image processing operations that process objects based on shape. The Voxel-Map includes two parts: one is dilation that reflected the voxel changes from lumen to wall, and the other is erosion that reflects the voxel changes inside the lumen.

The dilated vessel lumen by original pixel values at the morphological edge by formula is as follows:

$$A \oplus B = \{z \mid (\widehat{B})_z \cap A \neq \emptyset\}, \quad B = \{B_1, B_2, B_3\}, \quad (1)$$

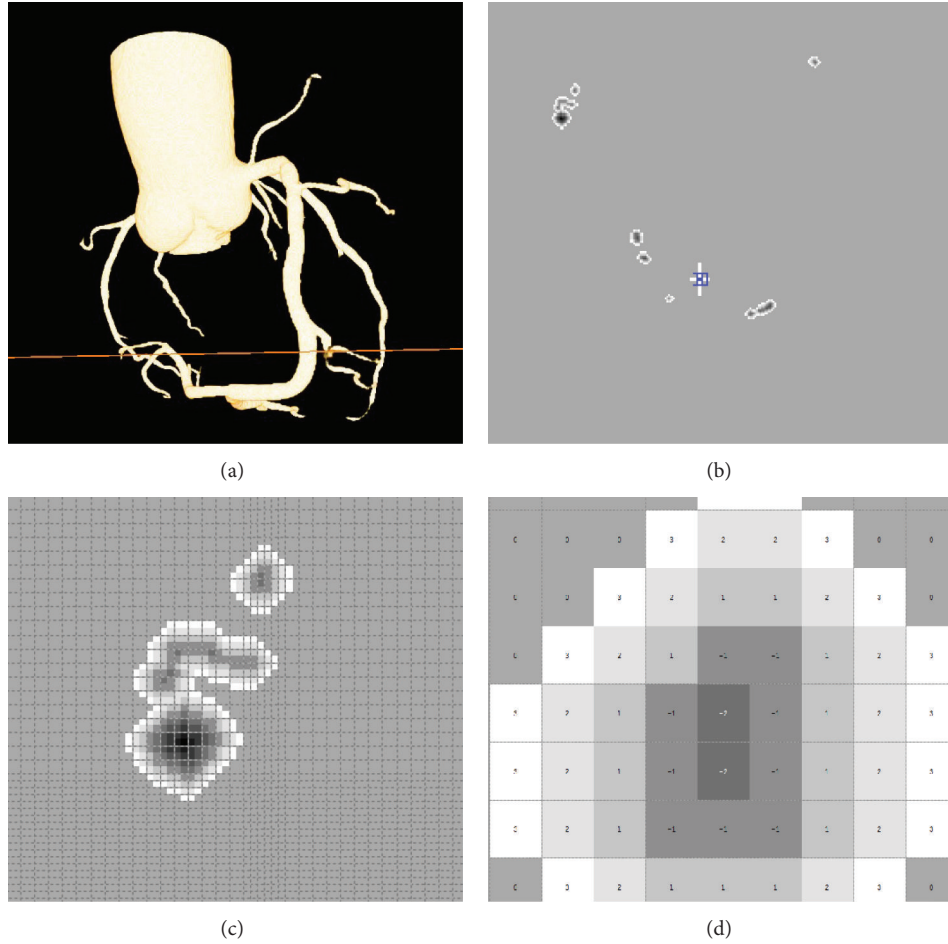


FIGURE 1: 3D-CTM reconstruction and creating Voxel-Map. The reconstruction of 3D-CTM (a); the horizontal plane in the position of 3D-CTM where lined in panel a (b) and a local region of the horizontal plane (c); more detailed values of pixels are shown in Figure 1(d). Positive and negative signs represent dilation and erosion, respectively, and the values represent the distance off lumen.

where \hat{B} is the reflection of the pixel locations B . In other words, it is the set of pixel locations z , where the reflected pixel locations of B overlap with foreground pixels in A when translated to z . A and B , respectively, represent original lumen pixel locations, and its surrounding pixels. The boundaries forming lumen to outside are represented as B_1 , B_2 , and B_3 , with each point in boundary only having one pixel.

The morphological erosion of the edge returned nearest pixels of inside boundary. The operations are defined as follows with the formula

$$A \ominus B = \{z \mid (B)_z \subseteq A\}, \quad B = \{B_{-1}, B_{-2}, \dots, B_{-n}\}. \quad (2)$$

$B_{-1}, B_{-2}, \dots, B_{-n}$ represent the $1, 2, \dots, n$ boundaries from the border of lumen to the center, and n is the thickness of the lumen. The voxel with an orientation to the outer lumen has an inner wall that is defined as positive and on the contrary wall, is defined negative. After performing morphological erosion on the current lumen region each time, the region is smaller by one pixel in every direction.

2.5. Quantification

2.5.1. Classified Attenuation Values. We divided attenuation values on the wall into six levels from one to six to describe the various severities of plaques: 0–49, 50–99, 100–199, 200–299, 300–399, and ≥ 400 , which was extracted from the 3D-CTM and assigned a different color for each range (illustrated in Figure 6). The first three and the last three ranges describe the severity of NCP and CP, respectively. As the contrast-enhanced CTA does not offer the best images for detection of CP, which can easily be identified and quantified, we do not consider discussing CP in this paper.

2.5.2. Plaques Location and Anatomical Location Related Labeling. Traditional quantification parameters can refer to pieces of literature [6, 10, 14, 15, 17, 20]. We want to emphasize on a new type of quantitative information: the plaques location and anatomical location related label, which is useful in planning pathway, guiding procession, and assessing results for PCI. The steps are as follows.

Step 1. A 3D surface reconstruction method was used to reconstruct non-calcified plaques (see Figure 7). Then plaque

model was generated, which not only can be used in visualization in 3D space but also can be saved as “obj” format, which is a standard 3D object file format consisting of vertex’s geometric position in space by x -, y -, and z -coordinates.

Step 2. Anatomical labeling: the segmentation of CTM was used as a bridge associating the 3D location of plaque with their anatomical labels, by finding the intersection set of 3D coordinates of plaque, in the segmentation of CTM, and the intersection set of 3D coordinates of the segmentation of CTM and labeled centerline tree, respectively, and intersecting the two sets.

3. Results

3.1. Voxel-Map Approach. After processing by Voxel-Map on 3D-CTM, from the outer border of lumen to the outer border of wall, four layers are labeled as -1 , 1 , 2 , and 3 , respectively, as shown in Figure 1. Any voxels whose attenuation values are less than 0 HU are considered as epicardial fat [6] and will be set as 0 Hu. If a voxel’s position not in the Voxel-Map was excluded from the 3D-CTM, a 3D-CAWM was generated.

3.2. CT Attenuation Values

3.2.1. The Difference of Attenuation Values between Vessel Lumen and the Boundary Layer of Vessel Wall. The attenuation values between vessel lumen and the boundary layer of vessel wall have different characteristics, as shown in Figure 2; in a whole coronary tree, the mean attenuation values for inner lumen are sharply increasing while closing to the aorta, but for the boundary layer adjacent lumens are relatively stable. This means that different individuals might have different CT attenuation values with different doses of contrast media for the inner lumen in various positions of the coronary tree but hold relatively stable values with nearby artery walls.

3.2.2. The Gradient Changes of Attenuation Values on Various Layers of Vessel Wall. As shown in Figure 3, the mean CT attenuation values of various layers on a wall are at a gradient decreasing from inside to outside. Our experimental results show that after being dilated three times, most voxel values are equal or less than 0, which means that those voxels cross the outer borders of the wall [6], so we set the maximum as B3 and set the negative values included in the wall as 0. Artery walls were divided into three layers: inside, middle, and outside. The reason we divided attenuation values on the wall into six levels to describe the various severities of plaques is also based on the gradient distribution of attenuation values. As shown in Figure 3, the first three levels, 0–49, 50–99, and 100–199, included most of voxels in each layer, respectively. The attenuation values of vessel walls on the range of the last three levels, 200–299, 300–399, and ≥ 400 , should be considered as calcified plaques with the various severities. The results of attenuation values belonging to various levels are shown in the right column of Figure 6.

3.3. Quantitative Analysis

3.3.1. Anatomical Labeling. The result is that centerline extraction of 3D-CTM, as shown in Figure 4(a), was organized

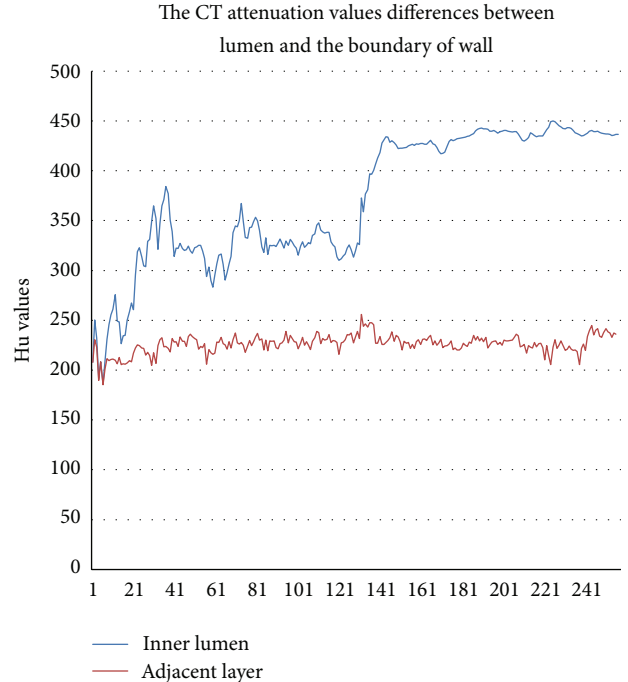


FIGURE 2: The blue and red lines represent the mean CT attenuation values of inner lumen and the border of lumen nearby wall, respectively. The y -axis is the range of CT attenuation values; the x -axis is slice number of CTA images.

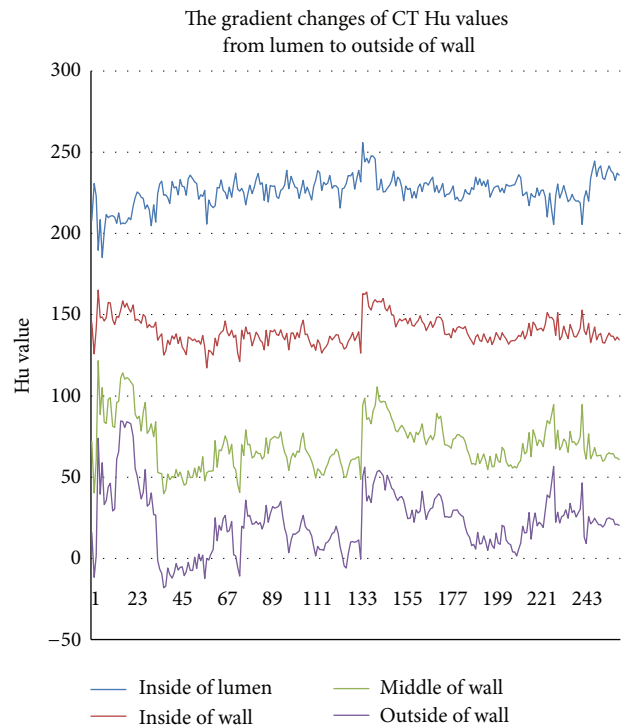


FIGURE 3: The mean CT attenuation values of various layer on wall are gradient decreased from inside to outside. The y -axis is the range of CT attenuation values; the x -axis is slice number of CTA images.

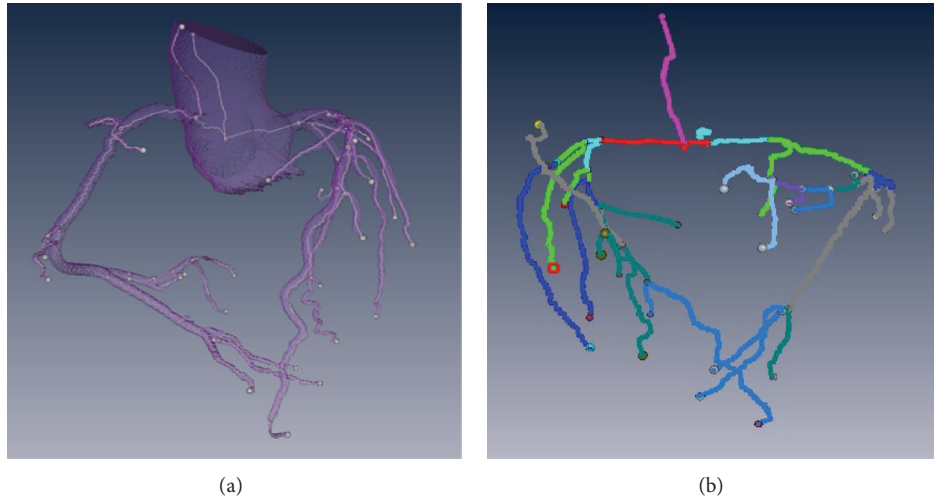


FIGURE 4: Centerline extraction (a) and anatomical labeling (b).

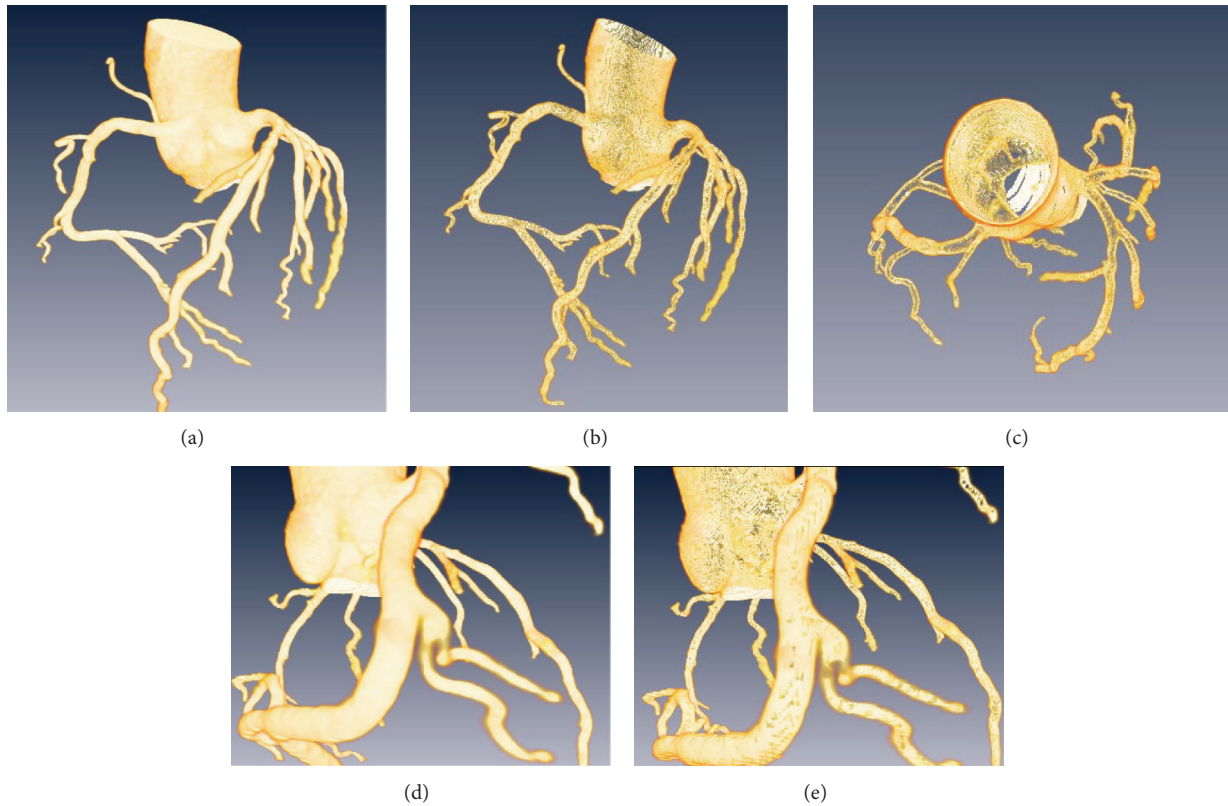


FIGURE 5: The three-dimensional coronary tree model (3D-CTM) and coronary artery wall model (3D-CAWM). The original 3D-CTM (a); the 3D-CAWM (b); the top view of 3D-CAWM (c); the stenosis of coronary tree in 3D-CTM (d) and 3D-CAWM (e).

by tree graph, and Figure 4(b) shows the resulting anatomical labeling based on the tree graph. The different colors represent different segments. Once we obtain the x -, y -, and z -coordinates of plaque, the computer will obtain which label the segment belongs to.

3.3.2. *The 3D-CAWM Analysis.* The result of 3D-CAWM, as shown in Figure 5, provided the shape and details of the

whole coronary artery wall including the proximal, middle, and distal segments. Compared with the original 3D-CTM, the output of the 3D-CAWM processed by a Voxel-Map focusing on the morphology and details of the wall and the stenosis is more remarkable. On contrast-enhanced CTA images (the left column in Figure 6), the lumen can be easily identified as areas of high attenuation, while it is difficult to identify the wall and plaque. Compared with original images,

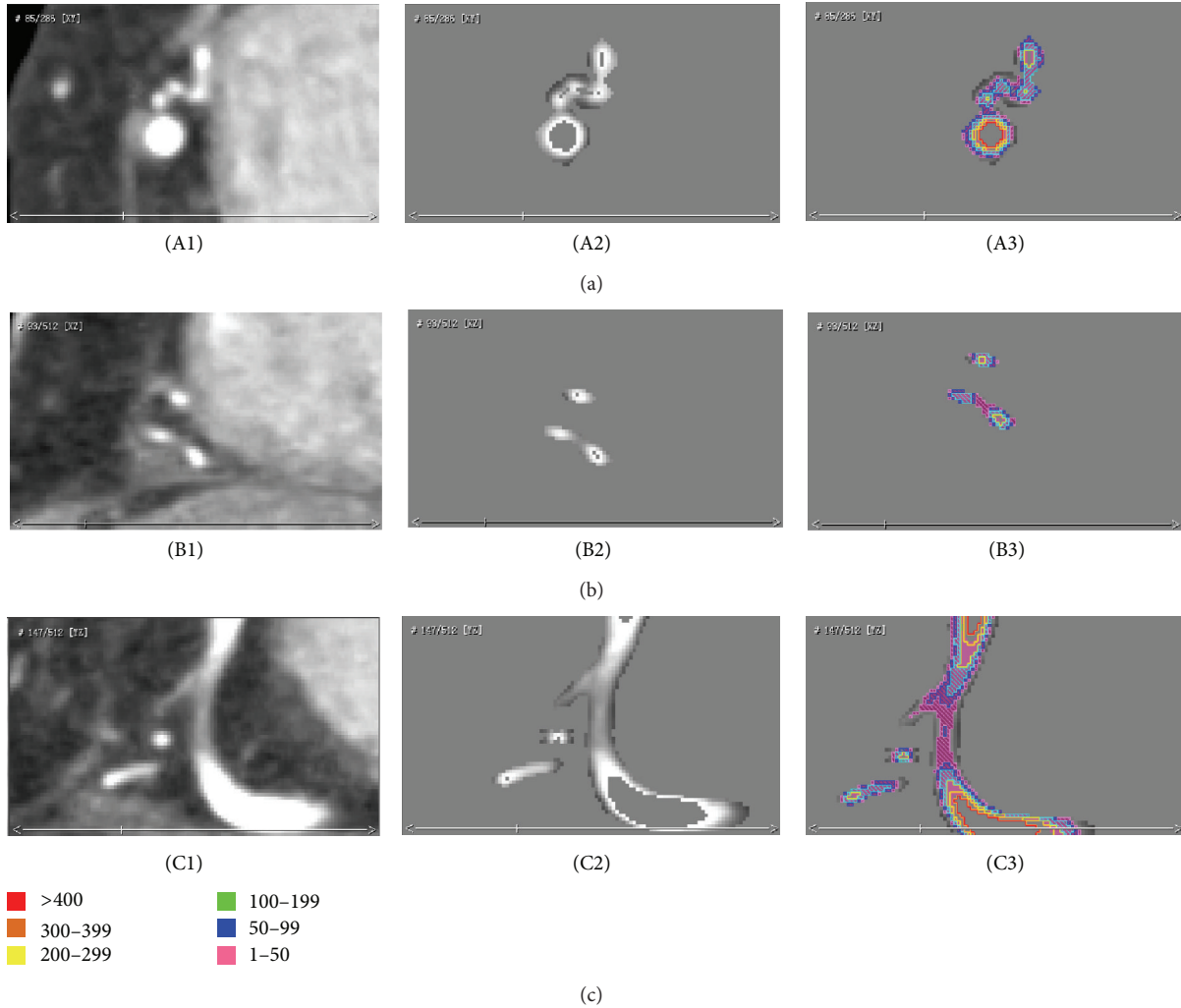


FIGURE 6: Quantitative analysis of 3D-CAWM. The left column shows that the original CTA images, A1, B1, C1, are horizontal plane, sagittal plane, and coronal plane, respectively. The middle column figures of A2, B2, and C2 show the corresponding planes in 3D-CAWM, and A3, B3, and C3 show the corresponding quantitative results based on Voxel-Map.

the 3D-CAWM (the right column in Figure 6), after having the Voxel-Map applied, is able to provide details of the nearby wall, and the different colors represent different severities.

3.4. Plaques Visualization and Location. The visualization of plaques in 3D-CAWM is shown in Figure 7. The locations of various NCPs on the coronary tree are recorded by computer automatically in the form of x -, y -, and z -coordinates. At the same time, anatomical labeling of plaque is generated by comparing these coordinates to the coordinates of the centerline in the 3D-CTM that were assigned an anatomical label.

The computer analysis results showed that the plaque consisted of level 1 and level 2, and the volume and percent of each level of plaque were 0.9834 mm^3 and 33.29%, 1.9703 mm^3 and 66.71%, respectively, and the location label belongs to RMA (right marginal artery). The location results of stenosis are consistent with the CMPR review results by an experimental radiologist. Compared with the stenosis views

in CMPR (shown in Figure 8), the characteristic of NCPs is more directly related to the results of quantitative analysis.

4. Discussion

4.1. Voxel-Map's Function. The key feature in quantitative analysis of NCP is recognition of artery walls. Manually describing the wall and plaque by a radiologist is time-consuming and may be prone to intraobserver variability [12–14] that influences the accuracy of quantitative analysis. In traditional automatic quantitative methods, the reader marks starting and ending positions of the plaque in the CMPR and then displays and adjusts attenuation thresholds for NCP and CP [13, 21], which is based on the hypothesis that before you quantitatively analyze plaques, you must first find their wall border. The positions of the start and end marked by reader also influence the computation of the mean attenuation values in various types. In order to solve this problem, we developed a Voxel-Map based on mathematical morphology

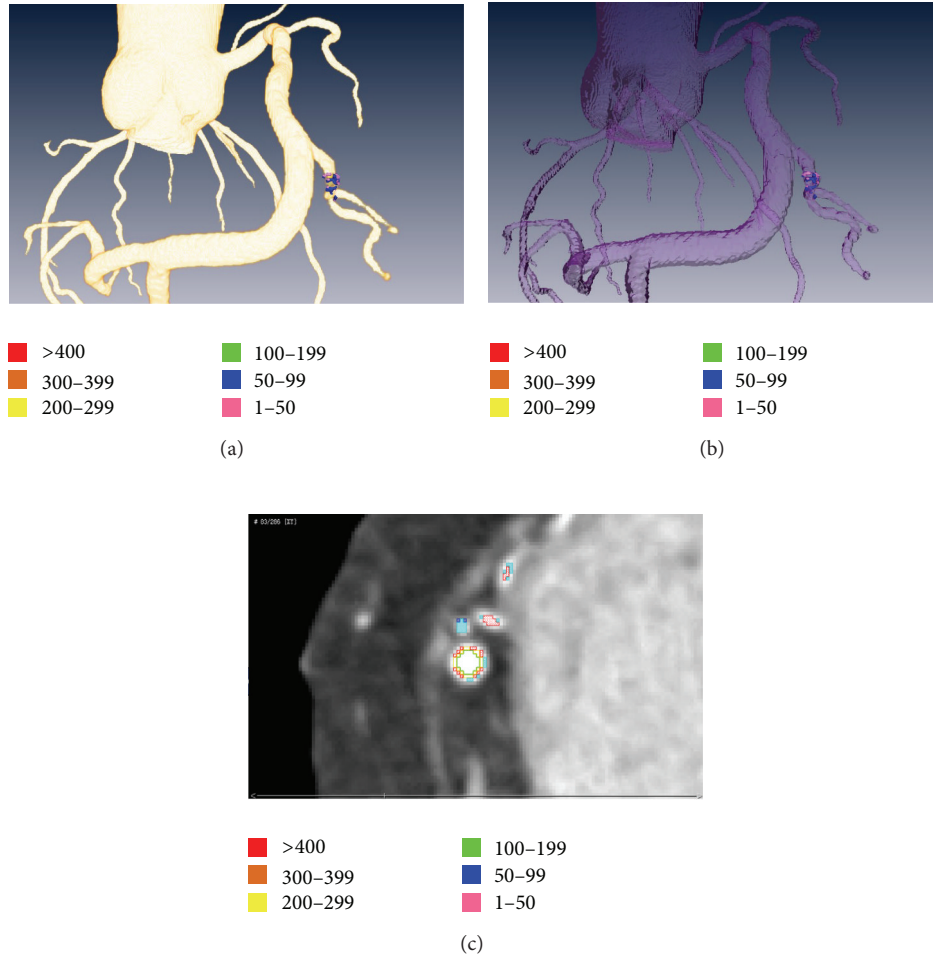


FIGURE 7: Plaques visualization. The reconstruction of coronary tree and NCPs (a); the transparent coronary tree to observe plaques (b); the analysis results in horizontal plane (c). The different colors represent different severities.

[19] to structurally and quantitatively analyze coronary artery walls on a 3D-CTM, which detects walls in a similar approach as IVUS but overcomes its limitation of only being able to be performed in proximal segments [6].

4.2. The 3D-CAWM Analysis. A 3D-CTM only includes the HU values of lumen and thus does not satisfy the need to analyze NCPs, as the attenuation values of NCPs are lower than the lumen, which were often excluded in the process of segmenting for 3D-CTM. Compared with original 3D-CTM, the stenosis is more remarkable on the 3D-CAWM that was processed by the Voxel-Map. The analysis method focuses on the morphology and details of wall, which can directly show the composition of plaque attenuations that are associated with its severity. The advantage of 3D-CAWM is that it can analyze the details of distal vessels and provide meaningful information for a radiologist’s diagnostic decision, which is impossible in previous methods. The obtained 3D-CAWM allows comprehensive visualization of vessel geometry and plaque distribution and can be further used in research to study the association between local plaque types and the progression of atherosclerosis.

4.3. Attenuation Values of Plaque. Recently, many studies had shown different ranges of the attenuation values in various compositions of plaque [6, 10, 14, 15, 17, 20]. However, according to previous studies, even IVUS has some limitations in the assessment of the true composition and vulnerability of plaque, due to substantial overlap of the corresponding attenuation values [17, 21]. As such, we further subdivided attenuation values on the wall into six levels to describe the various severities of the plaques. The outliers that located within one layer but not belonging to its level might be paid more attention by radiologist. Our group proposed the Voxel-Map as a new approach for analyzing and deep understanding attenuation changes in different degrees on the vessel wall in 3D space. Using our approach, early diagnosis and process monitor of the slight NCPs in vessel walls for patients become possible.

4.4. Plaques Location and Anatomical Location Related Label. Through the 3D surface reconstruction of non-calcified plaques, we can directly observe the location of plaque in the coronary tree and also can recognize its composition

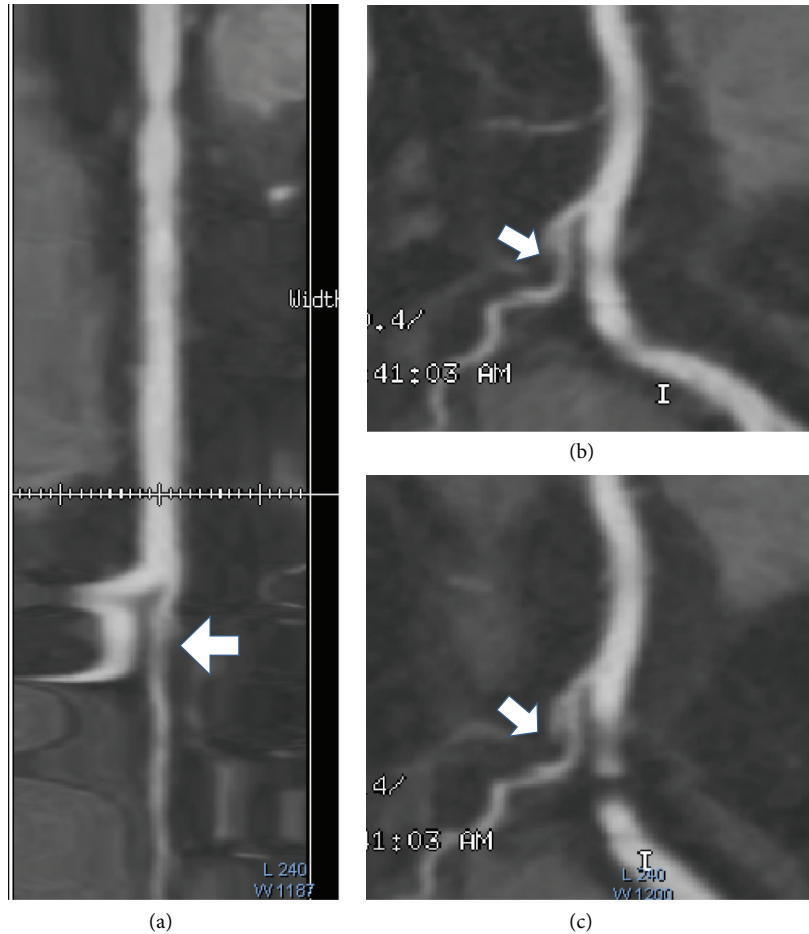


FIGURE 8: CMPR vessel representation (by AW Volume Share 4 software, GE, America). Longitudinal straightened views (a); the left rotated 284 degree views (b) and the left rotated 295 degree views (c).

(see Figure 7). Information about the locations that have plaques and to which branch they belong benefits doctors and will improve the success rate of percutaneous coronary intervention by evaluating the degree of danger and allowing for planning the pathway before operation and for assessing the outcome after operation. An anatomical location-related label is linked to plaque location, and its properties, such as per artery or per segment, can be used for reporting pathological findings according to CCTA image guidelines by radiologists and cardiologists [22, 23].

5. Conclusions

We proposed a Voxel-Map quantitative analysis approach, overcame the drawbacks of a CTA image regarding analysis of non-calcified plaque, and provided information regarding vessel walls based on a 3D coronary tree model. In this paper, we presented the Voxel-Map design and related quantitative analysis. The approach we proposed can provide details about the morphology from lumen to outer wall border, the types of plaques, and its location. This noninvasive, convenient, and economical approach can also be used for advantage of asymptomatic patients and to identify predictors of future

cardiovascular events. Furthermore, it can be used in planning and assessing the outcome of percutaneous coronary intervention.

Acknowledgment

This work was supported by the National Science Foundation of China (no. 61190122) (<http://www.nsf.gov.cn/>) and the Natural Science Foundation Project of CQ CSTC(cstc2011jjA10032).

References

- [1] S. Voros, S. Rinehart, Z. Qian et al., "Coronary atherosclerosis imaging by coronary CT angiography: current status, correlation with intravascular interrogation and meta-analysis," *Journal of the American College of Cardiology*, vol. 4, no. 5, pp. 537–548, 2011.
- [2] C. L. Schlett, M. Ferencik, C. Celeng et al., "How to assess non-calcified plaque in CT angiography: delineation methods affect diagnostic accuracy of low-attenuation plaque by CT for lipid-core plaque in histology," *European Heart Journal*, vol. 14, no. 11, pp. 1099–1105, 2013.

- [3] S. Motoyama, T. Kondo, M. Sarai et al., "Multislice computed tomographic characteristics of coronary lesions in acute coronary syndromes," *Journal of the American College of Cardiology*, vol. 50, no. 4, pp. 319–326, 2007.
- [4] J. D. Schuijf, T. Beck, C. Burgstahler et al., "Differences in plaque composition and distribution in stable coronary artery disease versus acute coronary syndromes; non-invasive evaluation with multi-slice computed tomography," *Acute Cardiac Care*, vol. 9, no. 1, pp. 48–53, 2007.
- [5] C. Bourantas, H. Garcia-Garcia, K. Naka et al., "Hybrid intravascular imaging: current applications and prospective potential in the study of coronary atherosclerosis," *Journal of the American College of Cardiology*, vol. 61, no. 13, pp. 1369–1378, 2013.
- [6] H. Brodoefel, C. Burgstahler, A. Sabir et al., "Coronary plaque quantification by voxel analysis: dual-source MDCT angiography versus intravascular sonography," *The American Journal of Roentgenology*, vol. 192, no. 3, pp. W84–W89, 2009.
- [7] H. Brodoefel, C. Burgstahler, M. Heuschmid et al., "Accuracy of dual-source CT in the characterisation of non-calcified plaque: use of a colour-coded analysis compared with virtual histology intravascular ultrasound," *British Journal of Radiology*, vol. 82, no. 982, pp. 805–812, 2009.
- [8] A. W. Leber, A. Becker, A. Knez et al., "Accuracy of 64-slice computed tomography to classify and quantify plaque volumes in the proximal coronary system: a comparative study using intravascular ultrasound," *Journal of the American College of Cardiology*, vol. 47, no. 3, pp. 672–677, 2006.
- [9] H. C. Stary, A. B. Chandler, R. E. Dinsmore et al., "A definition of advanced types of atherosclerotic lesions and a histological classification of atherosclerosis: a report from the Committee on Vascular Lesions of the Council on Arteriosclerosis, American Heart Association," *Arteriosclerosis, Thrombosis, and Vascular Biology*, vol. 15, no. 9, pp. 1512–1531, 1995.
- [10] J. Sun, Z. Zhang, B. Lu et al., "Identification and quantification of coronary atherosclerotic plaques: a comparison of 64-MDCT and intravascular ultrasound," *The American Journal of Roentgenology*, vol. 190, no. 3, pp. 748–754, 2008.
- [11] T. C. Villines, F. S. Rinehart, Z. Qian et al., "Coronary atherosclerosis imaging by coronary CT angiography," in *Atherosclerosis: Clinical Perspectives Through Imaging*, pp. 127–161, Springer, 2013.
- [12] M. Schmid, S. Achenbach, D. Ropers et al., "Assessment of changes in non-calcified atherosclerotic plaque volume in the left main and left anterior descending coronary arteries over time by 64-slice computed tomography," *The American Journal of Cardiology*, vol. 101, no. 5, pp. 579–584, 2008.
- [13] D. Dey, T. Schepis, M. Marwan, P. J. Slomka, D. S. Berman, and S. Achenbach, "Automated three-dimensional quantification of noncalcified coronary plaque from coronary CT angiography: comparison with intravascular US," *Radiology*, vol. 257, no. 2, pp. 516–522, 2010.
- [14] C. Burgstahler, A. Reimann, T. Beck et al., "Influence of a lipid-lowering therapy on calcified and noncalcified coronary plaques monitored by multislice detector computed tomography: results of The New Age II Pilot study," *Investigative Radiology*, vol. 42, no. 3, pp. 189–195, 2007.
- [15] M. E. Clouse, A. Sabir, C.-S. Yam et al., "Measuring noncalcified coronary atherosclerotic plaque using voxel analysis with MDCT angiography: a pilot clinical study," *The American Journal of Roentgenology*, vol. 190, no. 6, pp. 1553–1560, 2008.
- [16] P. M. Carrascosa, C. M. Capuñay, P. Garcia-Merletti, J. Carrascosa, and M. J. Garcia, "Characterization of coronary atherosclerotic plaques by multidetector computed tomography," *The American Journal of Cardiology*, vol. 97, no. 5, pp. 598–602, 2006.
- [17] K. Pohle, S. Achenbach, B. MacNeill et al., "Characterization of non-calcified coronary atherosclerotic plaque by multi-detector row CT: comparison to IVUS," *Atherosclerosis*, vol. 190, no. 1, pp. 174–180, 2007.
- [18] W. G. Austen, J. E. Edwards, R. L. Frye et al., "A reporting system on patients evaluated for coronary artery disease. Report of the Ad Hoc Committee for Grading of Coronary Artery Disease, Council on Cardiovascular Surgery, American Heart Association," *Circulation*, vol. 51, no. 4, pp. 5–40, 1975.
- [19] L. Najman and H. Talbot, *Mathematical Morphology*, John Wiley & Sons, 2013.
- [20] D. Kang, P. J. Slomka, R. Nakazato et al., "Automated knowledge-based detection of nonobstructive and obstructive arterial lesions from coronary CT angiography," *Medical Physics*, vol. 40, no. 4, Article ID 041912, 2013.
- [21] D. Dey, V. Y. Cheng, P. J. Slomka et al., "Automated 3-dimensional quantification of noncalcified and calcified coronary plaque from coronary CT angiography," *Journal of Cardiovascular Computed Tomography*, vol. 3, no. 6, pp. 372–382, 2009.
- [22] S. Abbara, A. Arbab-Zadeh, T. Q. Callister et al., "SCCT guidelines for performance of coronary computed tomographic angiography: a report of the Society of Cardiovascular Computed Tomography Guidelines Committee," *Journal of Cardiovascular Computed Tomography*, vol. 3, no. 3, pp. 190–204, 2009.
- [23] G. Yang, A. Broersen, R. Petr et al., "Automatic coronary artery tree labeling in coronary computed tomographic angiography datasets," in *Proceedings of the Computing in Cardiology (CinC '11)*, pp. 109–112, Hangzhou, China, September 2011.